J Mater Sci (2015) 50:7495–7536
DOI 10.1007/s10853-015-9303-7

REVIEW

Recent developments in TiO_2 as n- and p-type transparent semiconductors: synthesis, modification, properties, and energy-related applications

V. C. Anitha[1] · Arghya Narayan Banerjee[1] · Sang Woo Joo[1]

Received: 6 May 2015 / Accepted: 25 July 2015 / Published online: 7 August 2015

Abstract TiO_2-based thin films and nanomaterials have been fabricated via physical and solution-based techniques by various research groups around the globe. Generally, most applications of TiO_2 involve photocatalytic activity for water and air purification, self-cleaning surfaces, antibacterial activity, and superhydrophilicity. As a wide-bandgap semiconductor, modified TiO_2 belongs to a class of materials called transparent semiconducting oxides (TSOs), which are simultaneously optically transparent and electrically conductive. TSOs continue to be in high demand for a variety of applications ranging from transparent electronics and sensor devices to light detecting and emitting devices in telecommunications. However, reports on TiO_2 applications as an effective TSO for transparent electronics applications have been limited. In general, TiO_2 is intrinsically an n-type semiconductor but can be doped to have p-type semiconductivity. This provides a very important opportunity to fabricate all-transparent homojunction devices for light harvesting and energy storage. P-type TSOs have recently attracted tremendous interest in the field of active devices for emerging transparent electronics for potential use in ultra-violet light-based solar cells. Therefore, a detailed overview of the synthesis, band structure modification via doping, properties, and applications of modified TiO_2 as n- and p-type TSOs is warranted. This article comprehensively reviews the latest developments. The discussion includes solution-based wet chemical techniques and vacuum-based dry physical techniques fabricating TiO_2–TSOs. The synthesis of p-TiO_2 in particular is discussed in detail as it may provide interesting breakthroughs in emerging transparent electronics applications. Also, the structural, optical, and electrical properties of TiO_2 are discussed in the context of TSO applications, specifically the defect chemistry of TiO_2 to obtain n- and p-type semiconductivity, which could provide interesting insights into the band structure engineering of TiO_2 for conductivity reversal. Applications of both n- and p-type TiO_2 have been reviewed in detail in relation to thin film transparent homo/heterojunction devices, dye-sensitized solar cells, electrochromic displays, and other energy-related applications.

✉ Arghya Narayan Banerjee
banerjee_arghya@hotmail.com; arghya@ynu.ac.kr

✉ Sang Woo Joo
swjoo@yu.ac.kr

[1] School of Mechanical Engineering, Yeungnam University, Gyeongsan 712-749, South Korea

Introduction

Transparent semiconducting oxides (TSOs) have high optical transmittance and electrical conductivity at the same time. As a wide-bandgap material, TSOs are expected to have poor electronic conduction because carrier doping for large-gap materials is difficult. Hence, the general notion is that high optical transparency and high electrical conduction cannot go hand in hand in the same material [1–5]. TSOs constitute a unique group of oxide materials with these two mutually incompatible properties together. The conductivity of the TSOs generally varies from 10^{-8} S-cm^{-1} to more than 10^3 S-cm^{-1} [4–10]. These oxides are divided into two groups based on their electrical conductivity: transparent conducting oxides (TCOs) with conductivity higher than 10^3 S-cm^{-1} and transparent oxide semiconductors (TOSs) with conductivity between 10^{-8} and 10^3 S-cm^{-1}. Although TCOs have nearly metallic conductivity (hence the nomenclature), their band

structures are not metallic type but rather semiconducting type with a large bandgap. We have combined these groups into one category of TSOs. TSOs are well known and have been used industrially for more than 50 years [1, 2]. The first report of a TSO was published in 1907, when Badeker reported that thin films of Cd metal deposited in a glow discharge chamber could be oxidized to make them transparent while maintaining electrical conductivity [3]. TSOs are greatly important for their increasing use in applications such as touch panels and flat-panel displays (FPDs). Other electronic/optoelectronic device applications include Si-based solar cells, light-emitting diodes (LEDs), waveguides, low-emissivity ("low-e") windows, electrochromic or "smart" windows, oven windows, defrosting windows, invisible security circuits, antistatic coatings, flexible displays, holographic recording media, waveguides for sensors and telecommunication applications, write-once-read-many-times memory chips (WORM), electronic ink, and field-emission displays [4–25].

Since the 1960s, the most widely used TSO for optoelectronic device applications has been tin-doped indium oxide ($In_{2-x}Sn_xO_3$; ITO) and fluorine-doped tin-oxide ($SnO_{2-x}F_x$). These materials offered the best performance in terms of conductivity, transmissivity, excellent environmental stability, reproducibility, and surface morphology [12, 13, 21, 22]. Nowadays, TSOs are a major component in organic light-emitting diodes (OLEDs), copper indium gallium diselenide (CIGS) solar cells, dye-sensitized solar cells (DSSC), and blue GaN-based LEDs [4–8, 10, 16, 17], in which other well-known TSOs are also widely used, including SnO_2:Sb, ZnO:In/Al/F/B/Ga, In_2O_3:/F/Sb/Pb, and Cd_2SnO_4. [26–32]. But due to the scarcity and rapidly expanding consumption in many fields, it is necessary to find alternative TSOs.

Recently, several multicomponent TSOs and their doped versions have been reported, such as Zn_2SnO_4, $ZnSnO_3$, $GaInO_3$:Ge/Sn, $AgInO_2$:Sn, $MgIn_2O_4$, $CdSb_2O_6$:Y, $Zn_2In_2O_5$, $ZnGa_2O_4$, $In_4Sn_3O_{12}$, and $CdIn_2O_4$:Sn. [15, 33–40]. These have interesting electronic/optoelectronic applications but have yet to break into the TSO industry for high volume production because of their costly and complex fabrication processes. Therefore, it is still necessary to explore new TSO materials produced by cost-effective and simple processes for diverse and wide-scale device applications. The fabrication process should also have flexibility in tuning the TSO properties for improved device performance. ZnO, TiO_2 (Nb-doped TiO_2–TNO), and doped SnO_2 are widely used as indium-free TSOs for low-e windows and other applications [17–23, 41–46]. These materials are compared in Table 1. Even though TiO_2-based TSOs have optoelectronic performance characteristics close to ITO, they also have significant shortcomings in terms of deposition parameters and chemical stability [44].

The control of oxygen stoichiometry in TNO films is the most important parameter for obtaining high conductivity. The oxygen partial pressure during deposition should be maintained at $\sim 1 \times 10^{-3}$ Pa to control the oxygen content of the films. The annealing conditions also control the electrical properties of the TNO. Annealing in air at 600 °C yields insulating films [46]. As a result, there is a growing body of research on TSO to look for new indium-free materials outside the group of typical TSOs. The discovery of transparent conducting properties in Nb- and Ta-doped anatase TiO_2 thin films has extended the range of materials that can be used for transparent electrodes [44, 45].

TiO_2 is a versatile material that has been used in many applications, such as gas sensors, solar cells, photocatalytic layers for self-cleaning glass, photocatalytic degradation of organic wastes, hydrogen production, storage media, optical coatings for filters and waveguides, and various biological- and health-related applications [47–66]. Since the early twentieth century, titanium dioxide (TiO_2) has been widely used as a pigment in sunscreens, paints, ointments, toothpaste, etc. [48–50]. A phenomenon of photocatalytic water splitting on a TiO_2 electrode under ultra-violet (UV) light was discovered [59–62], which gave new hope in helping ease energy crises through effective utilization of solar energy in photovoltaic and water-splitting devices [63–65]. Transparent thin films based on TiO_2 are widely applied in the coating industry for preparation of hydrophobic or hydrophilic films, self-cleaning coatings, optical filters, and protective films [48, 51, 54, 55, 66–68].

TiO_2 is a technologically important material with a wide range of applications, easy availability, and cost-effective syntheses processes. In this review article, we focus on recent progress in the synthesis, properties, modifications, and applications of n- and p-type transparent semiconducting TiO_2 thin films, their doped versions, and corresponding nanomaterials. The manuscript is arranged as follows. After preliminary introduction of the basic

Table 1 Comparison of material parameters between conventional TSOs (ITO, ZnO, SnO_2, etc.) and the TiO_2-based TSO

	ITO, ZnO	TNO
Carrier density	Small $n_e < 10^{21}$ cm^{-3}	Large $n_e > 10^{21}$ cm^{-3}
Electron mobility	Large	Small
Dielectric constant (ε_0)	4	5.9
Effective mass (m^*)	0.3	1

Reproduced from [41] with permission from © 2010 WILEY–VCH Verlag GmbH & Co. KGaA, Weinheim

properties of TSO and the importance of TiO_2 as a TSO in "Introduction" and "Basic electronic band structure of TSO" section, the synthesis methods for transparent conducting TiO_2 nanomaterials is given in "Synthesis of TiO_2-based TSO" section, including nanoparticles, nanorods, nanowires, and nanotubes. These methods are primarily categorized into vacuum-based and solution-based techniques. A sub-section introduces the fabrication processes of p-type semiconducting TiO_2. p-type TSOs (*p*-TSO) have recently attracted tremendous interest in the optoelectronics industry for potential applications in transparent electronics and UV-based solar cells [69–73].

It is well known that most of the TSOs mentioned are n-type semiconductors. *p*-TSOs were developed in the late 1990s, and applications in active devices have been highly limited [74]. Sato et al. [75], and Kawazoe et al. [76] reported p-type conductivity in transparent thin films of binary NiO and ternary $CuAlO_2$ and opened up a new field in transparent electronics. All-transparent *p*–n junctions of TSO materials could be used as a "functional window" to transmit the visible portion of solar radiation and generate electricity using the UV part, thus potentially extending solar cell applications into the UV region. Undoped TiO_2 is a well-known n-type semiconducting material, and it can be made to conduct holes by doping [77]. Therefore, a *p*–n transparent homojunction fabricated with *p*- and n-type transparent TiO_2 can be used very efficiently if the junction properties can be improved. Hence, a detailed review on the fabrication of *p*-TiO_2 is necessary.

"Properties" section includes a detailed review of the structural, thermal, electronic, and optical properties of TiO_2 nanomaterials. The size, shape, and crystal structure of TiO_2 nanomaterials influence the surface stability and can make the transitions between different phases of TiO_2 under pressure or heat become size dependent. The influence of the size of TiO_2 nanomaterials on the X-ray diffraction patterns and Raman vibrational spectra is also summarized. These data could help to determine the size of the materials to some extent, although the correlation between the spectra and size of TiO_2 nanomaterials is not straightforward. The review of modifications to TiO_2 nanomaterials is mainly limited to research related to the optical properties of TiO_2 nanomaterials, which are important in many applications. TiO_2 nanomaterials are normally transparent in the visible light region. By doping, sensitization, or size tuning, it is possible to improve the optical sensitivity and activity of TiO_2 nanomaterials in the visible light region. Therefore, a detailed review on the tuning of the optical properties of TiO_2 nanomaterials is given in terms of bandgap engineering by the quantum size effect for potential TSO applications.

In "Applications" section, transparent electronics (heterojunctions, functional windows), environmental applications (photocatalysis, sensing), and energy applications (photovoltaics, water splitting, photo-/electrochromics, hydrogen storage) are reviewed with emphasis on clean and sustainable energy, since increasing energy demands and environmental pollution are creating a pressing need for clean and sustainable energy solutions. The fundamentals and working principles of TSO-based devices are discussed. TiO_2 nanomaterials are used either as a TSO or as a component to facilitate understanding and improvement of current and practical TiO_2 nanotechnology. Although TiO_2 has been used for many years, there is a complete lack of reports on the application of *p*-TiO_2 as an active channel in electronic and transistor circuit devices. Therefore, the properties and application perspectives of *p*-TiO_2 are discussed in detail in this section.

Finally, "Future developments" section discusses the future prospects of TiO_2-based TSO materials and gives concluding remarks. Several previous review articles reported detailed accounts of the synthesis, doping, material properties, and photocatalytic, photoelectrochemical, energy-related, and bio-related applications of TiO_2 films and nanostructures [48–50, 59–65, 78–83]. But there is negligible literature reviewing TiO_2 as a TSO material. Recently, only Hitosugi et al. [41, 45] presented a brief review of the synthesis and transparent conductive properties of Nb-doped TiO_2 (TNO). They discussed the mechanistic differences between TNO and conventional TSOs. But to the best of our knowledge, there has been no other review accounting for the entire TiO_2–TSO family, including both n- and p-type TiO_2 and energy/TSO-related applications. This review covers a wide spectrum of the recent developments of TiO_2 as transparent conductors in terms of syntheses, modification, opto-electrical properties, and TSO-based energy applications (including p-type TiO_2 and *p*–n active junctions for transparent electronics). The content could thus be very useful for the field of TCOs for practical applications.

Basic electronic band structure of TSO

The general band picture of TSO is shown in Fig. 1. Assuming flat band potential, the approximate bandgap of TSO is generally higher than the energy of a 400-nm blue photon (which is roughly 3.1 eV). Therefore, visible photons, which have energy between 2.1 and 3.1 eV, are transmitted through the material without exciting the electrons from the valence band (VB) to the conduction band (CB). The material thus becomes transparent in the visible region of solar radiation. As a wide-bandgap semiconductor, the material can acquire acceptor levels (for p-type) or donor levels (for n-type) under appropriate conditions (doping or induction of non-stoichiometric

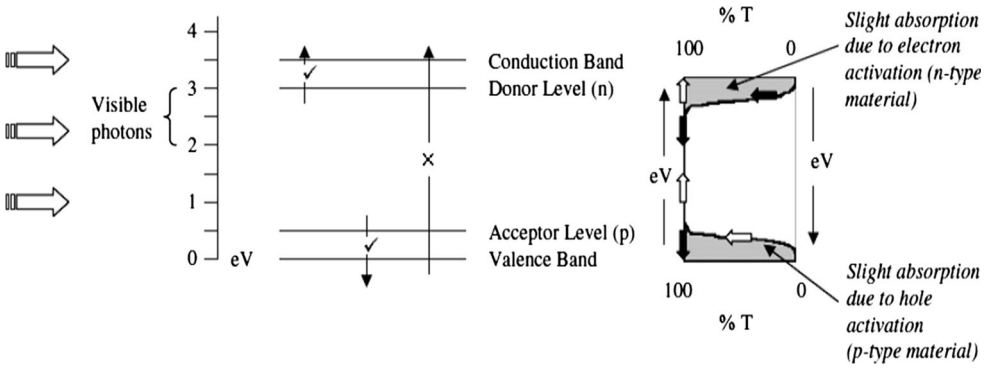

Fig. 1 Bandgap design of TSO. Reproduced from [71] with permission from © 2005 Elsevier Ltd.

defects). Visible radiation would have enough energy to excite electrons from the donor level to the CB (for n-type TSOs) or holes from the acceptor level to the VB (for p-type TSOs). Therefore, the optical transmission (*%T*) should theoretically be 100 % within the visible region (400–800 nm). Slight absorption in the low energy region may occur due to activation of electrons from the donor level to the CB (for n-type TSOs) or holes from the acceptor level to the VB (for p-type TSOs), as shown in Fig. 1.

According to the band theory of solids, the mobility of carriers (electrons or holes) in TSOs is defined by the position and curvature of the CB minimum (CBM) and VB maximum (VBM), which determine the effective masses of the corresponding carriers and hence the carrier mobility [74]. In general, a majority of TSOs are binary metal oxides where metals have electronic configuration in the form of $[n-1]\ d^{10}ns^2$. During oxide formation, the unoccupied *ns* orbital of the metal cation (M*s*) interacts strongly with the occupied 2*p* orbital of oxygen (O2*p*) to produce the electronic band structure of the TSOs. Figure 2 schematically depicts the electronic band structure of the TSOs. Figure 2a shows the *E*–*k* diagram of a stoichiometric TSO material, where the VB comprises the bonding and non-bonding occupied O2*p* states and the CB arises from the anti-bonding M*s*–O*p* interaction. Because of this

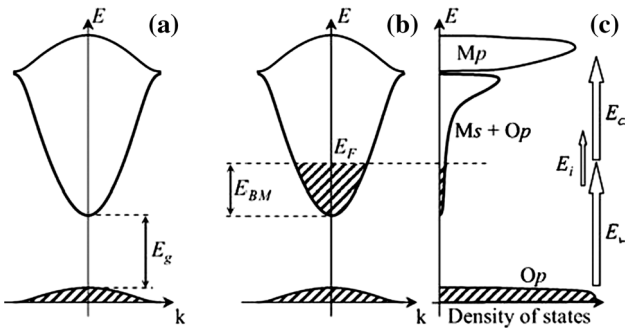

Fig. 2 Band structure of **a** stoichiometric, **b** non-stoichiometric TSO, and **c** corresponding density of states. Reproduced from [74] with permission from © 2010, John Wiley and Sons Ltd.

parabolic band formation due to the M*s* + O*p* interaction, a forbidden energy gap (E_g) is created between the CBM and VBM to form the wide bandgap in TSOs.

Higher energy states are created by the empty *p* states of the metal ions (M*p*) [70, 74]. For a non-stoichiometric or doped TSO, the creation of degenerate levels pushes the Fermi level (E_F) upward, as shown in Fig. 2b, and the corresponding density of states is shown in Fig. 2c. A majority of TSOs show n-type semiconductivity for several reasons. Firstly, the CB of TSO is mostly formed due to the spherically shaped extended metal *s* orbital, making the carrier transportation within the CB region more favorable than the VB region and leading to better electron conductivity than hole conductivity. Therefore, it is easier to obtain promising n-type TSOs with relatively good conductivity and transparency [70, 74].

Secondly, as the VB comprises occupied O2*p* levels, the strong electronegativity of oxygen ions makes the VB edge strongly localized, leading to very large hole effective mass and much lower hole mobility than electron mobility. Also, because of the ionicity of metallic oxides, the O2*p* level becomes far lower than the valence orbit cationic levels (Fig. 3a). Hence, holes (either intrinsically created or externally induced by non-stoichiometry or doping) become strongly localized around the oxygen ions to create deep acceptor levels that are unable to migrate readily within the crystal lattice. These holes require enough energy to overcome a large barrier height to be delocalized and migrate within the crystal lattice, resulting in poor p-type conductivity and hole mobility [70, 71, 76].

It is clear that typical TSOs are n-type semiconductors (*n*-TSO), and the induction of p-type semiconductivity (*p*-TSO) is difficult unless the holes are delocalized from the highly electronegative oxygen ions. This can be achieved by chemical modulation of the VB (CMVB) [72], where a closed d^{10} orbital of metal cations (such as Cu-d^{10}, Ag-d^{10} etc.) with energy level comparable to the O_2 p^6 level is combined with an oxygen ion to create degenerate hybridized O2*p* states (Fig. 3b, inset). This leads to the formation of an extended VB structure, which results in the

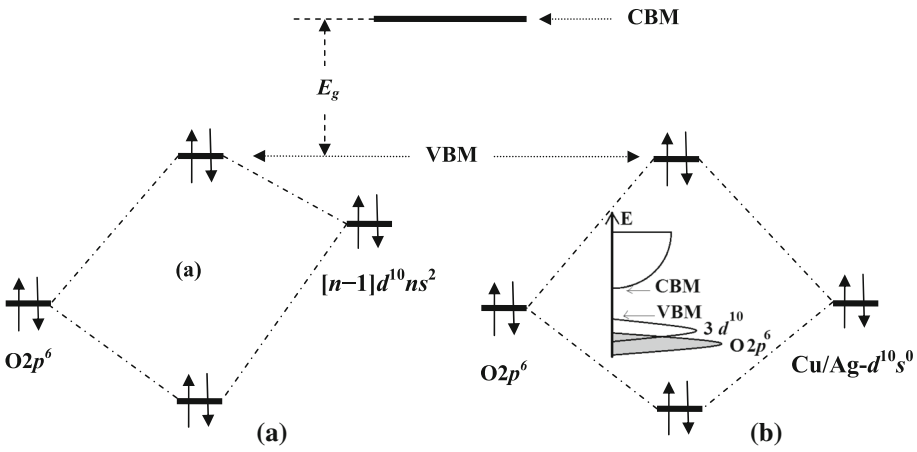

Fig. 3 **a** Schematic diagram of the chemical bonding between cation and anion in (**a**) a typical n-type TSO, **b** p-type binary metal oxide. Both the atomic orbitals are occupied by electron pairs, which results in the formation of the highest occupied level as the valence band maxima. *Inset* Density of states of *p*-TSO. Reproduced from [72] with permission from 2 © 2000, Materials Research Society/© 2011

delocalization of holes, easy migration into the crystal lattice, increased hole mobility, and improved p-type semiconductivity. This is why Cu_2O and Ag_2O are intrinsically p-type materials, although their bandgaps are less than 3.1 eV, making them unsuitable for *p*-TSO applications [70]. To obtain intrinsic *p*-TSO, additional structural requirements need to be satisfied to create superlattice or layered structures to suppress the three-dimensional interactions between d^{10} cations, which would increase the bandgap to the transparent regime [70, 71]. The details of the criteria to create intrinsic *p*-TSOs are not in the scope of this report but are available elsewhere [71].

Electronic structure of TiO_2 as TSO

Generally, density functional theory (DFT) calculations for the electronic band structure of semiconductors and insulators are highly underestimated when used with local density approximation (LDA) or generalized gradient approximation (GGA) for the exchange correlation functional [84–89]. One accurate way to predict the band structure is ab initio many-body perturbation theory (MBPT) with dynamically screened interaction or GW approximation (GWA), where the self-energy is considered to be the product of the single-particle Green function *G* and the screened interaction *W* [85–92]. Several groups theoretically calculated the bandgaps (E_g^{GWA}) of different polymorphs of TiO_2 (mainly anatase, rutile, and brookite) by the GWA method combined with some hybrid/correlation/exchange functional. These methods are given in Table 2 [87], and recently reported representative band structure calculations of TiO_2 polymorphs are shown in Fig. 4 [91]. The calculated bandgaps are well within the transparent regime, indicating potential for use in TSO applications. The experimentally obtained bandgap values of different TiO_2 polymorphs are discussed in "Electro-optical properties" section.

Hitosugi et al. [93] reported the theoretical band structure of Nb-doped TiO_2 by DFT calculations using a standard GGA (Perdew–Wang: PW91) functional. As shown in Fig. 5, the bandgap is much lower (2.24 eV) than the experimental value (3.2 eV) from using the DFT + GGA method and producing an underestimated value. No MBPT calculation with GWA has been reported for Nb-doped TiO_2 to predict bandgap values more accurately.

The band calculations revealed strong hybridization of Nb-4*d* orbitals with Ti-3*d* orbitals to form a *d*-nature CB, without any impurity states within the bandgap. This results in high carrier density and superior visible transparency. Also, it has been observed that the band structure of Nb-doped TiO_2 is essentially identical to that of undoped anatase TiO_2, although Nb doping changes the band filling without affecting the band dispersions [94]. When the Nb concentration within the TiO_2 matrix is increased beyond an optimal level, the carrier concentration is decreased considerably, apparently because of interstitial oxygen atoms, which strongly interact and combine with surrounding Nb atoms to produce in-gap states and compensate for carrier electrons in the heavily doped region [95].

Synthesis of TiO_2-based TSO

Transparent conducting TiO_2 films have been fabricated by various techniques [41–46]. These include both vacuum-based techniques (like sputtering, pulsed laser deposition—PLD, and chemical vapor deposition—CVD) and solution-based techniques (like sol–gel, dip/spin-coating, and spray pyrolysis). Although the solution-based techniques are simpler and more cost effective than vacuum-based techniques, they are not compatible with modern solid-state device fabrication techniques, especially complementary-

Table 2 Theoretically calculated electronic bandgaps of TiO_2 polymorphs via GWA method

TiO_2 polymorphs	E_g (eV)				References
	GWA + LDA	GWA + PBE	GWA + DFT + U	GWA + HSE06	
Rutile	3.38	3.59	3.40	–	[88, 89]
		3.46			[90, 91]
Anatase	3.56	3.83	3.70	–	[92]
		3.73			
		3.79			
Brookite	–	4.45	–	3.68	[91]

Reproduced from [87] with permission from © 2014 American Chemical Society

PBE Perdew–Burke–Ernzerhof, *U* Coulomb repulsion, *HSE06* Heyd–Scuseria–Ernzerhof

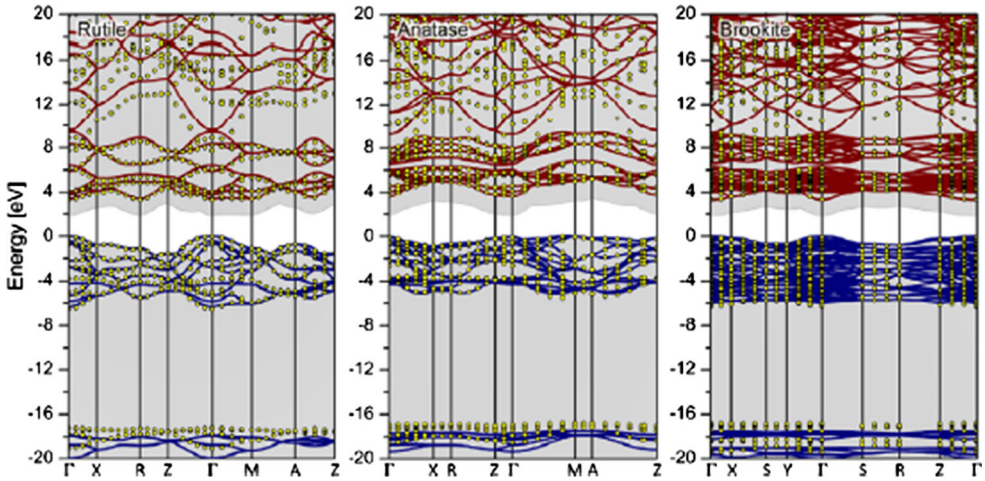

Fig. 4 TiO_2 band structures for the rutile (*left*), anatase (*middle*), and brookite (*right*) polymorphs. Pictured are the DFT–HSE06 band structure as well as quasiparticle (QP) energies (dots) obtained from PBE–G_0W_0 calculations. The *gray shaded areas* correspond to energies below the highest valence band and above the lowest conduction band from DFT–PBE calculations. For PBE and HSE06 eigenvalues, the valence band maximum has been chosen as the zero point of the energy scale. G_0W_0 QP energies are given with respect to DFT–PBE energy scale. The HSE06 calculations have been carried out with regular 7 × 7 × 11, 9 × 9 × 3 and 3 × 5 × 5 Γ-centered *k*-point meshes for rutile anatase and brookite. The various high symmetry lines were additionally sampled by 40 *k*-points to obtain the HSE06 band structure. For rutile, anatase, and brookite, the GW calculations were carried out on top of DFT–PBE calculations with 192, 384, and 768 electronic bands, regular 8 × 8 × 12, 10 × 10 × 4, and 4 × 6 × 6 Γ-centered *k*-point meshes, and 192 frequency points for sampling the dielectric function, respectively. These numerical parameters provide bandgaps converged within about 0.02 eV accuracy, as tested for the case of rutile. Reproduced from [91] with permission from © 2012 IOP Publishing Ltd., Printed in UK & USA

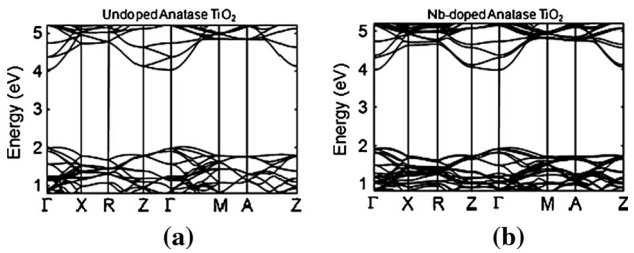

Fig. 5 Calculated electron energy band structure of **a** undoped and **b** Nb-doped TiO_2. Reproduced from [93] with permission from © 2008 The Japan Society of Applied Physics

metal–oxide–semiconductor integrated-circuit (CMOS-IC) fabrication. Hence, the methods are not commercially viable.

Vacuum-based techniques

Sputtering

Sputtering is suitable for low cost and uniform coating on large-area substrates and has been established as a standard technique for preparing TSO films [96–101]. Niu et al. [102] prepared transparent TiO_2 films on PDMS substrate by DC reactive sputtering. The target was titanium, and the distance between the target and substrate was fixed at 100 mm. The chamber was evacuated to a vacuum level lower than 1.2×10^{-3} Pa, and then argon was introduced. The input power and substrate temperature were fixed at 350 W at ambient temperature, and the discharge voltage was maintained at 220 V. When the Ar discharge was

stabilized, oxygen was introduced into the sputtering chamber, and the color of the sputtering plasma changed from pink to blue. The gas pressure during the reactive sputtering was increased from 1.0 to 1.6 Pa as the oxygen flow rate was increased from 0 to 3.0 mL/min by adjusting the exhaust through the main gas valve.

Five samples (A_1–A_5) were prepared by changing the ratio of argon and oxygen flow mixtures (1:0.5, 1:1, 1:1.5, 1:2, and 1:4). The sputtering time for sample A_1 was varied from 30 min to 1 h with an average deposition rate of 100 nm/h and constant discharge power of 350 W. All the films were transparent, and their colors changed from slight blue to slight green. The preparation of highly transparent films is very important because it is necessary to have minimal light absorption within the coated films to retain the original transparency of the substrate. Figure 6a shows the optical transmittance spectra of PDMS and five modified samples over a wavelength range of 250–700 nm. After coating TiO_2 films, all the five samples have optical absorption over a wavelength range of 250–300 nm, which is typical for the fundamental absorption of TiO_2.

Sample A_1 showed a transmittance of about 0.57 at a wavelength of 280 nm, indicating relatively low optical loss. A_3–A_5 were prepared at ambient temperature. The samples had large amounts of O_2 and showed lower transmittance. The film thickness is a main factor in the film transmittance and it was lowest for sample A_1, which had the highest UV transmittance. The surface morphology is another factor in the film transmittance. A film with larger crystallite size could cause stronger reflection and interference of light, which results in lower transmittance and lower optical absorption. UV spectrum analysis indicates that all the samples have optical absorption over a wavelength range of 250–300 nm. The structure was amorphous, the surface morphology was smooth, and the size of grains was about 30–50 nm. Mixed titanium oxidation states of the film surfaces were found in XPS analysis (Fig. 6b).

Sicha et al. [103] reported low-temperature high-rate sputtering of hydrophilic transparent TiO_2 thin films using DC dual magnetron (DM) sputtering in an Ar + O_2 mixture on unheated glass substrates. The DM was operated in a bipolar asymmetric mode and equipped with Ti (99.5) targets with 50-mm diameter. A spectrally selective reflector can be fabricated by depositing a TCO on a reflective substrate. The films were deposited on unheated microscope glass slides ($26 \times 26 \times 1$ mm^3) and unheated polycarbonate (PC) substrates ($26 \times 26 \times 3$ mm^3). TiO_2 films with a constant thickness $t \approx 1000$ nm were prepared to avoid a strong influence of the film thickness on the properties [104, 105]. Figure 7 presents the time evolution of the pulse waveforms of the current (I_d) and voltage (U_d) in the dual magnetron discharge generated in the oxide mode of sputtering ($P_{O_2} = 0.15$ Pa) at different values of the repetition frequency f_r, an average discharge current $I_{da\ 1,\ 2}$ of 3 A, and P_T of 0.9 Pa. It is clear from Fig. 7 that the utilization of the period $T = 10$ μs ($f_r = 100$ kHz) can be improved if f_r of the pulses is increased. Due to shortening of the pulses and cutting of the stationary regime, only the first time interval with strong sputtering is present, and plasma build-up regime starts to dominate.

The conclusion is that transparent hydrophilic TiO_2 film composed of a mixture of the anatase and rutile phases can be obtained with transition-mode sputtering at high deposition rate ($a_D = 80$ nm/min) on glass substrate with

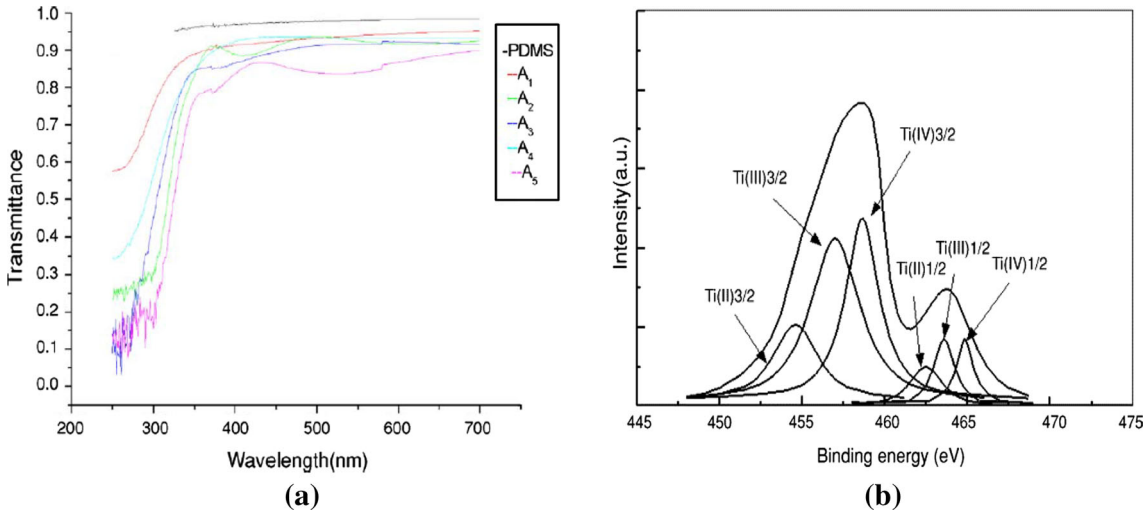

Fig. 6 **a** Optical transmittance spectra of PDMS and samples coated with TiO films, **b** XPS spectra of the TiO_2 films with mixed titanium oxidation states. Reproduced from [102] with permission from © 2005 Elsevier B.V.

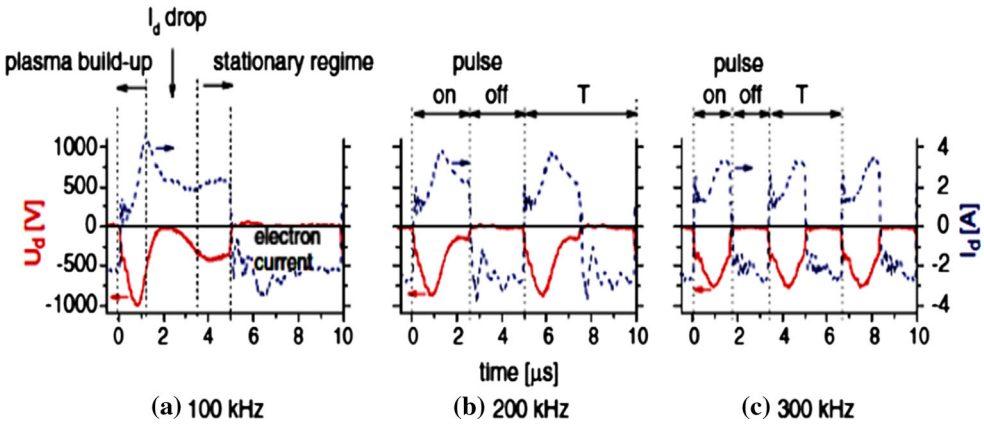

Fig. 7 The time evolution of discharge voltage U_d and current I_d in the DC pulsed discharge generated by the dual magnetron equipped with Ti targets at $I_{da1,2} = 3$ A, $P_{O_2} = 0.15$ Pa (oxide mode), $P_T = 0.9$ Pa and three values of repetition frequency (f_r) = 100, 200, and 300 kHz; $I_{da1,2}$ is the discharge current averaged over the pulse lengths. Reproduced from [103] with permission from © 2007 Springer-Verlag

substrate-to-target distance $d_{s-t} = 100$ mm and $T_{surf} \approx 180$ °C. TiO_2 film with excellent hydrophilic properties was successfully sputtered in oxide mode at $T_{surf} \approx 120$ °C, $a_D = 5.2$ nm/min, and $f_r = 350$ kHz on a PC substrate without thermal destruction. The evolution of the film structure with increasing f_r is shown in Fig. 8. Nb-doped anatase TiO_2 ($Ti_{1-x}Nb_xO_2$; TNO) has a high refractive index (~2.4), which plays an important role in increasing the plasma wavelength and suppressing electron scattering by impurities [106]. Excellent electrical conductivity ($\sigma \sim 2173.9$ Ω cm) and visible transparency of 60–80 % were achieved, even with polycrystalline TNO films on glass prepared by crystallizing amorphous films at high temperature (>500 °C) [107]. This demonstrates the potential of TNO as a next-generation TSO.

Maghanga et al. [108] deposited TiO_2:Nb thin films on glass substrate by DC magnetron sputtering followed by optical characterization to extract the related optical parameters. They used these parameters to model optimized solar effective reflectors (SSRs) for solar cell applications. SSRs may offer advantages in photovoltaic systems by concentrating sunlight. When the reflector in a photovoltaic concentrator is replaced with an SSR, such as in a compound parabolic reflector (CPC), the reflectance for the SSR should depend on the wavelength λ. Ideally, the reflectance should also be unity for wavelengths below that corresponding to the bandgap of the absorber (λ_c) and zero for $\lambda > \lambda_c$. Then, the SSR can direct the solar radiation that is effective for photoelectric conversion towards the solar cell and simultaneously suppress radiation that would only heat up the cell and thereby reduce its efficiency.

The significant design parameters are the integrated reflectance values (R_{cell} and R_{therm}):

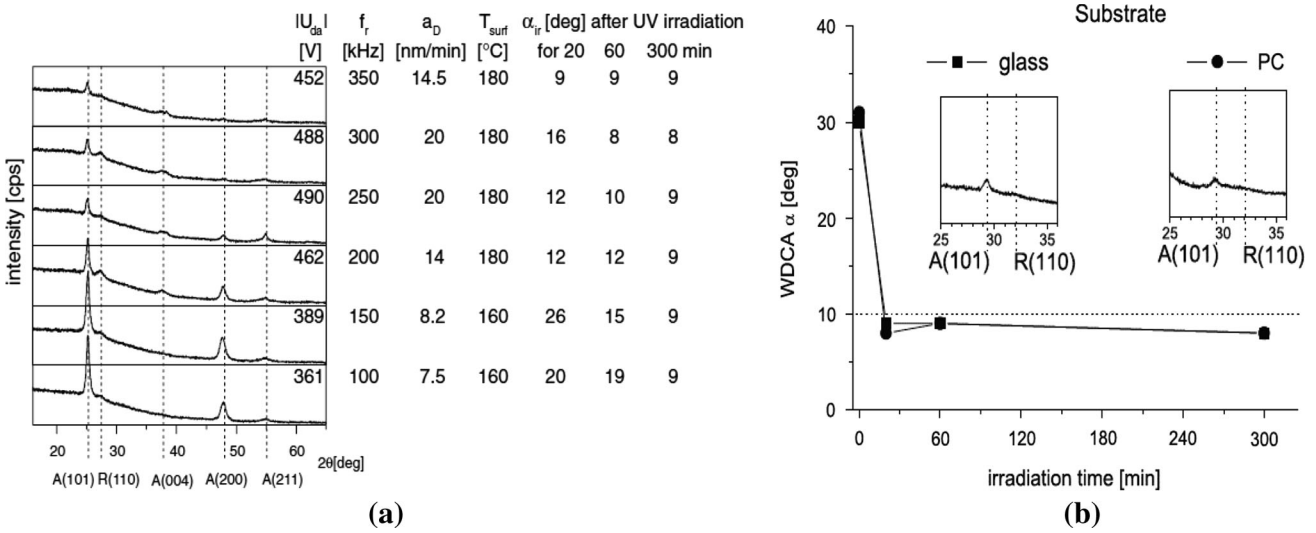

Fig. 8 **a** Development of the structure in the ~1000-nm-thick transparent TiO_2 films reactively sputtered on unheated glass substrates at $I_{da1,2} = 3$ A, $d_{s-t} = 100$ mm and $T_{surf} \approx 160$–180 °C, $P_T = 0.9$ Pa and $P_{O_2} = 0.15$ Pa with increasing f_r. **b** The X-ray structure of the 1000-nm-thick transparent TiO_2 films sputtered on glass and polycarbonate substrates at $f_r = 350$ kHz, $I_{da1,2} = 2$ A, $P_T = 0.9$ Pa, $P_{O_2} = 0.2$ Pa, $d_{s-t} = 100$ mm, $T_{surf} \approx 120$ °C, and $a_D = 5.2$ nm/min and their hydrophilicity as a function of time of UV irradiation. Reproduced from [103] with permission from © 2007 Springer-Verlag

$$R_{\text{cell}} = \int_{300}^{\lambda_c} G(\lambda)R(\lambda)\mathrm{d}\lambda / \int_{300}^{\lambda_c} G(\lambda)\mathrm{d}\lambda \quad (1)$$

$$R_{\text{therm}} = \int_{\lambda_c}^{2500} G(\lambda)R(\lambda)\mathrm{d}\lambda / \int_{\lambda_c}^{2500} G(\lambda)\mathrm{d}\lambda, \quad (2)$$

where $G(\lambda)$ is the AM 1.5 solar spectrum. A structure with a TSO on top of an aluminum substrate coated with an aluminum oxide layer was considered, and literature data for the optical constants of Al [109] and Al_2O_3 [110] were used. Corresponding films were then successfully produced. The best wavelength-integrated reflectance values were 79 and 31 % in the ranges of $300 < \lambda < 1100$ nm and $1100 < \lambda < 2500$ nm, respectively. An SSR based on TiO_2:Nb film was modeled and then successfully produced experimentally [108]. An intermediate buffer layer of Al_2O_3 deposited between a reflective substrate and the TSO is necessary to suppress the deep fringes arising from the high refractive index of the TiO_2:Nb film. This intermediate film also plays a role in reducing the reflectance around the absorption edge.

An increase in the doping concentration reduces R_{therm} drastically due to increased free carrier absorption. The modeled reflectance data in Fig. 9a show that the reflectance around λ_{min} is systematically reduced as the Nb concentration is increased, while λ_{min} seems to shift to lower wavelengths as the Nb content is increased. This is due to free carrier absorption. The variation of R_{cell} and R_{therm} is a function of the Nb concentration in the film based on the modeled reflectance data (Fig. 9b). R_{therm} drops sharply with increasing Nb concentration, whereas R_{cell} is not affected. Experimental and theoretical reflectance data agree well, as shown in Fig. 9c for TiO_2:Nb film on Al substrate without an intermediate layer and for a three-layer construction with a 90-nm Al_2O_3 intermediate layer. The minor deviations can be attributed to the non-ideal thickness of the Al_2O_3 layer. The inconsistency in thickness could also be due to oxidation of the Al substrate. There is an additional layer besides the sputtered layer before the sputter deposition. The effect may vary depending on how successful the initial etching of the substrate is. Moreover, the optical constants of Al obtained from the literature may differ slightly from those of the actual Al substrate used. Comparison of the two figures shows that besides minimizing the fringe depth, the Al_2O_3 layer reduces the reflectance around the absorption edge and shifts it toward longer wavelengths.

Kasai et al. [111] reported anatase Nb-doped TiO_2 TCO formation on GaN(0001) surfaces using a sputtering method. Thin films of Nb-doped TiO_2 were deposited on an insulating GaN(0001) template using RF sputtering at substrate temperatures (T_s) ranging from RT to 400 °C. A two-inch $Ti_{0.94}Nb_{0.06}O_2$ disk was used as a target [101], with the base pressure of the sputter chamber below 5×10^{-5} Pa prior to each deposition. Film deposition was carried out in a mixture of Ar and O_2 with various O_2/(Ar + O_2) flow ratios with f (O_2) in the range of 0–0.2 % and a total pressure of 0.8 Pa. The RF power applied to the target was kept constant at 100 W during sputtering, and the target-sample distance was set to 75 mm.

The films had a resistivity of 8.1×10^{-4} Ω cm with absorption less than 5 % at a wavelength of 460 nm (film thickness ~170 nm). The refractive index values of the Nb-doped TiO_2 and GaN match very well with each other, and the results appear to indicate that the light extraction efficiency of GaN-based LEDs can be further enhanced using TiO_2-based films as transparent electrodes. Figure 10(1) shows the transport properties of annealed films as functions of oxygen partial pressure [$f(O_2)$]. The resistivity value (ρ) tends to decrease with increasing $f(O_2)$ from 0 to 0.1 % (Fig. 101a). This may be due to the volume fraction of rutile phase (which has a higher ρ than anatase) decreasing with $f(O_2)$. At $f(O_2) = 0.125$ %, ρ shows a minimum value of 8.1×10^{-4} Ω cm. However, further increases in $f(O_2)$ result in increased ρ. The carrier concentration n_e shows a weak dependence on $f(O_2)$ and reaches a maximum of $n_e = 1.5 \times 10^{21}$ cm^{-3} at $f(O_2) = 0.125$ % (Fig. 101b). The activation efficiency of Nb donors exceeds 90 %, which is a characteristic feature of TNO. The Hall mobility μ_H attained a maximum value of 4.5 cm^2/V s, which is approximately half that of TNO on glass substrate.

Figure 10(2) shows the optical transmittance (T), reflectance (R), and absorbance spectra of a polycrystalline TNO thin film ($f(O_2) = 0.125$ %) and a GaN template. Interference patterns were found to originate from the GaN template on the Al_2O_3 substrate. The optical properties at the wavelength of 460 nm determine the performance of blue or white LEDs. At this wavelength, the reflectance values with and without TNO are almost identical, suggesting that TNO and GaN have nearly equivalent refractive indices. The TNO film on the GaN template has a transmittance of approximately 70 %, and an absorptance as low as 5 % estimated from $A = 100 - (T + R)$. The absorption of the insulating GaN template is less than 1 % at 460 nm. The A value can be further reduced to 3.2 % by increasing $f(O_2)$ to 0.15 %, although a slight increase in ρ to 1.2×10^{-3} Ω cm occurs ($n_e = 1.3 \times 10^{21}$ cm^{-3}, $\mu_H = 3.9$ cm^2/V s).

Pulsed laser deposition

PLD is an efficient technique for producing robust nanostructured films capable of assisting laser desorption/ionization for low-molecular-weight analyses for cationization

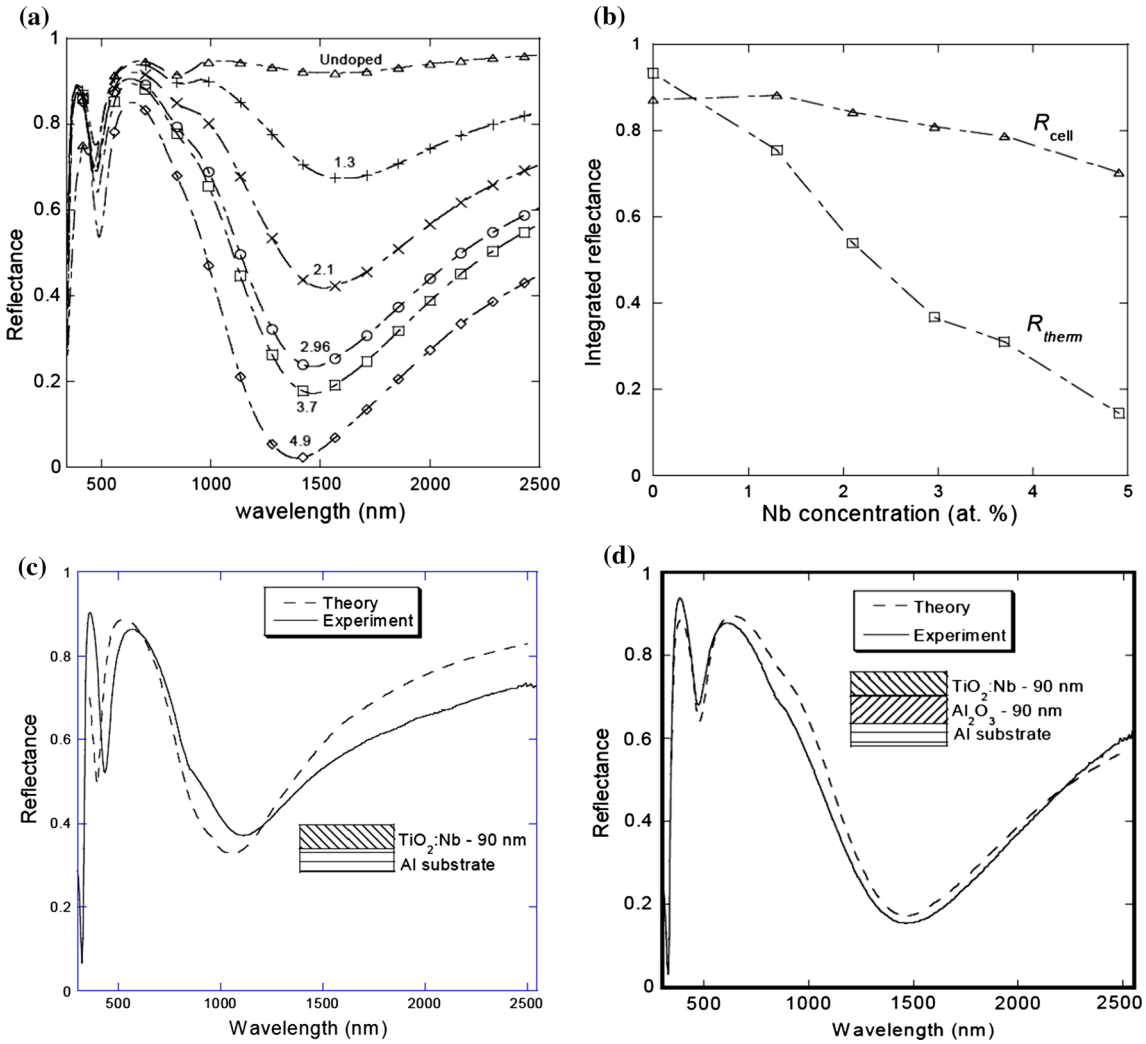

Fig. 9 **a** Modeled reflectance of TiO_2:Nb/Al_2O_3/Al three-layer film. Nb doping level is represented. **b** Variation of R_{cell} and R_{therm} for TiO_2:Nb/Al_2O_3/Al three-layer films with Nb doping, as calculated from the modeled reflectance. **c** Comparison between calculated and measured spectral reflectance for a TiO_2:Nb/Al two-layer structure, **d** TiO_2:Nb/Al_2O_3/Al three-layer structure. The layer thicknesses are shown. Reproduced from [108] with permission from © 2009 SPIE, CCC code: 0277-786X/09/$18

by metals. Tantalum-doped TiO_2 films were synthesized on glass substrate at 300 °C by PLD technique [112–115]. The target used in the experiments was prepared by the traditional ceramic process. TiO_2 and Ta_2O_5 powders with 99.99 % purity were mixed in molar ratio of 0.96:0.04 and then ground by ball milling for 12 h. The homogenous mixture was pelletized, pressed into a disk, calcined at 1100 °C for 5 h in air, and then cooled to room temperature before introduction to a PLD chamber for film deposition.

After film deposition and post-annealing in vacuum ($\sim 10^{-4}$ Pa) at temperatures ranging from 450 to 650 °C, the films crystallize into anatase TiO_2 structure and have very good conductive features. With increasing post-annealing temperature up to 550 °C, the measured resistivity of the films was around 8.7×10^{-4} Ω cm. The films had high transparency over 80 % in the visible light region. These results indicate that tantalum-doped anatase TiO_2 films have great potential as TCOs [114].

The XRD profiles of the deposited films do not show any obvious diffraction peaks, implying an amorphous structure. Diffraction peaks at around 25.1° in Fig. 11a corresponding to the anatase structure were observed for the samples followed by vacuum annealing at temperatures higher than 450 °C. The diffraction profiles change with the annealing temperatures. Figure 11b shows the resistivity of the samples annealed at different temperatures. The sample annealed at 550 °C had the lowest resistivity of 8.7×10^{-4} Ω cm, and the films had the largest crystallite size compared with samples annealed at other temperatures. The resistivity of the films was very large due to the amorphous structure. After post-annealing in vacuum, all

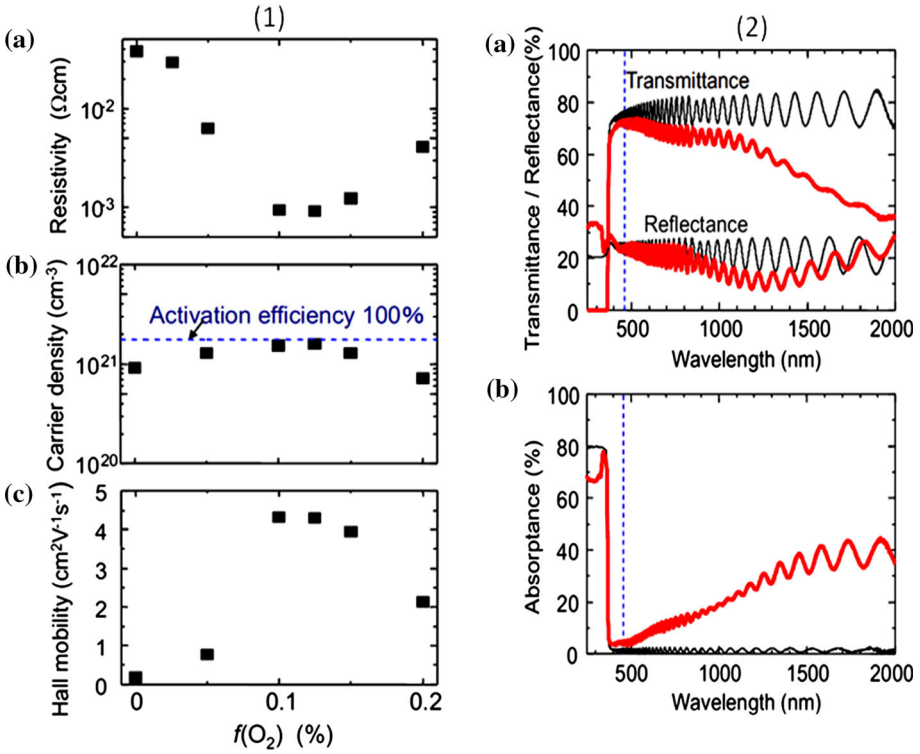

Fig. 10 **1** Transport properties of polycrystalline anatase $Ti_{0.96}Nb_{0.06}O_2$ thin films on insulating GaN template measured at room temperature. **1**(a) resistivity, (b) carrier density, and (c) Hall mobility shown as functions of oxygen flow ratio ($f(O_2)$). **2** *Color line* (a) Optical transmittance T and reflectance R spectra of GaN template (*black* or *thin curves*) and polycrystalline anatase $Ti_{0.96}Nb_{0.06}O_2$ films on GaN template (*red* or *thick curves*). The $Ti_{0.96}Nb_{0.06}O_2$ film was prepared at $f(O_2) = 0.125$ %. (b) Absorbance A evaluated from the relation $A = 100 - T - R$. The *dashed vertical line* indicates the wavelength of 460 nm. The A value of the $Ti_{0.96}Nb_{0.06}O_2$ film is less than 5 % at 460 nm film thickness (170 nm). Reproduced from [111] with permission from © 2010 American Institute of Physics (Color figure online)

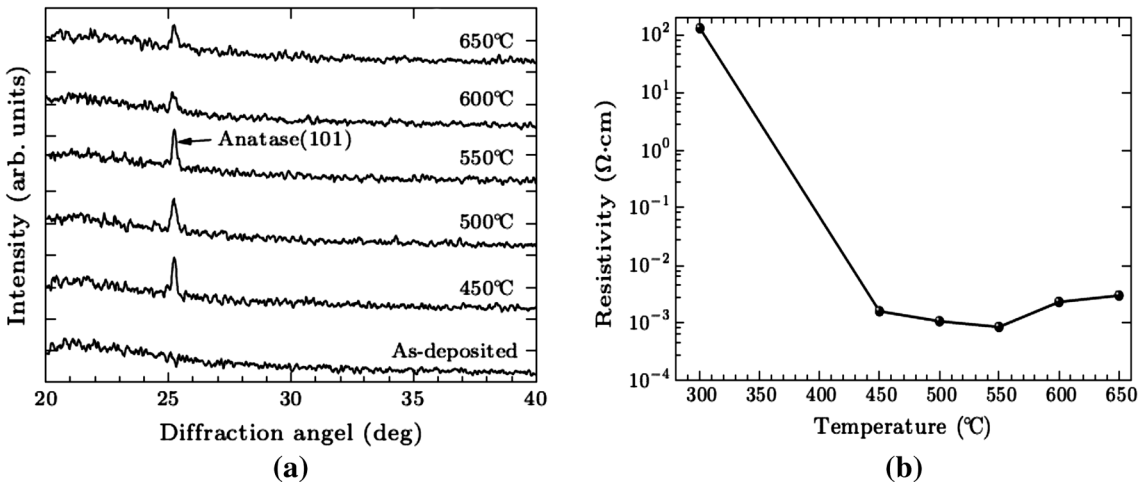

Fig. 11 **a** XRD patterns of the $Ti_{0.96}Ta_{0.04}O_2$ at different temperatures, **b** resistivities of $Ti_{0.96}Ta_{0.04}$ O_2 films on the glass before and after annealing at different temperatures. Reproduced from [114] with permission from © 2011 Chinese Physical Society and IOP Publishing Ltd

the films became conductive. The annealing conditions were very effective for increasing conductivity.

Hsu et al. [115] investigated the morphological, structural, and optical properties of anatase TiO_2 thin films synthesized by PLD technique. High-quality photocatalytic polycrystalline TiO_2 anatase films can be grown by PLD at moderate substrate temperature under oxygen pressures between 1.0 and 20.0 mTorr, followed by annealing with

an O_2 pressure of 1 atm at 600–650 °C for 1 h. A large amount of amorphous phase was found in the as-deposited films. Raman data showed that nano-crystallization occurred in films deposited on SiO_2 and MgO substrates, for which the XRD patterns displayed a lack of crystallinity. The structural data correlate well with the optical and contact-angle results. Films deposited at low pressures are oxygen-deficient and become stoichiometric after subsequent annealing in oxygen. Surface roughness is an additional factor for increased film hydrophilicity.

Tonooka et al. [116] deposited conducting Nb-doped TiO_2 thin films on glass substrates by PLD method and examined the dependence of their electrical and crystalline properties on the deposition and annealing conditions. The development of anatase phase in the Nb-doped TiO_2 film was suggested to be the dominant factor influencing the conductivity of the film. The O_2 pressure during deposition and the annealing temperature were optimized to fabricate the most conductive Nb-doped TiO_2 thin films. The lowest resistivity of 6.7×10^{-4} Ω cm was obtained for the film deposited at RT in 0.92-Pa O_2 partial pressure followed by annealing at 350 °C for 10 min in vacuum ($<10^{-5}$ Pa). The Nb-doped TiO_2 thin films showed high reflectance between 10.0 and 24.0 μm and low absorbance of less than 10 % in the visible region.

Chemical vapor deposition

Among the different TiO_2 deposition techniques, CVD offers several advantages, including purity of the coating, moderately low cost compared to other vacuum-based techniques, versatility to produce different morphologies, and good adhesion to the substrate [117–120]. Mills et al. [121] fabricated a series of novel CVD films of titanium (IV) oxide of different thicknesses in the range of 10–91 nm on quartz substrate by reacting titanium (IV) chloride and ethyl acetate. The films were clear, mechanically robust, and comprised a thin layer of nanocrystalline anatase titania of different thicknesses that absorbs UV light. The photocatalytic activity depended directly on the fraction of light absorbed, and the quantum yield for the overall process was 3.5×10^{-4}, which is lower than that for sol–gel TiO_2 films.

Pazoki et al. [122] developed a simple atmospheric pressure CVD setup to grow different TiO_2 morphologies on glass substrates simultaneously (Fig. 12). Rapid film growth at relatively low temperature (250 °C) was obtained using $TiCl_4$, O_2, and H_2O as reactants. Depending on the zone in the hot-wall reactor, spherical particles, nanowires, and mesoporous structures were found due to local differences in temperatures, reactant concentrations, and boundary layer conditions. Two types of light-scattering paste were tested: the CVD paste and commercial paste PST-400C (JGC Catalysts and Chemicals Ltd.) containing 400-nm-sized anatase TiO_2 microcrystals. Figure 13 shows the total transmission spectra of the different TiO_2 films on the FTO substrates. The transparent film shows a high transmittance of about 82 %.

Adding the CVD scattering layer decreased the transmittance to 33 % in the wavelength range of 600–700 nm, while adding the JGC layer reduced the transmittance to about 22 %. Since TiO_2 does not absorb light at these wavelengths, the decrease in transmittance is directly attributed to the light-scattering properties of the CVD and JGC films. This was confirmed by the pure white appearance of the films. The total reflectances at these wavelengths were thus 67 and 78 % for the CVD and JGC film, respectively. Table 3 presents the optical and electrical properties of TiO_2 thin films obtained with different dopant concentrations and various vacuum-based synthesis processes.

Solution-based techniques

Sol–gel

The sol–gel process has distinct advantages over other techniques, including excellent compositional control, homogeneity at the molecular level due to the mixing of liquid precursors, and lower crystallization temperature [123–126]. Moreover, the microstructure (i.e., the pore size, pore volume, and surface area) of films can be tailored by controlling the processing parameters such as the ratio of the components and temperature [127]. TiO_2 thin films prepared by sol–gel processing have been reported as new materials for humidity sensors [128]. TiO_2–SnO_2 sol–gel thin films were also investigated for this application. The film with 20 wt% TiO_2 had the highest sensitivity with a change of over three orders of magnitude in resistance when varying the relative humidity (RH) between 20 and 90 % [129].

Figure 14(1) shows SEM images of TiO_2 and TiO_2–SnO_2 thin films. The images reveal that the TiO_2–SnO_2 films have rougher surfaces than TiO_2 films, which may be due to slight agglomeration by mixtures of both SnO_2 and TiO_2 colloids. The TiO_2–SnO_2 films have nanometer grain size and nanoporous structure. This structure is likely to facilitate the adsorption process of water molecules because of the capillary pores and large surface area. Figure 14(2) shows the resistance as a function of RH for the TiO_2 and TiO_2–SnO_2 thin films. All the films were annealed at 500 °C for 30 min. The resistance of the films decreases linearly with increasing RH with about three orders change at RH of 20–90 % with a good exponential relationship. In particular, the resistance of the TiO_2-20 wt% film decreases considerably in this range, showing

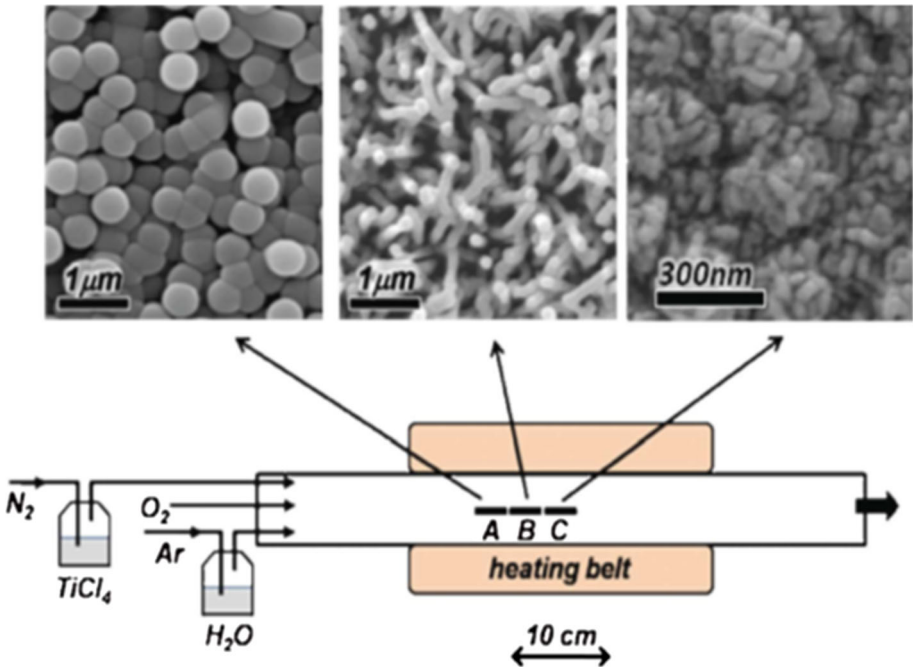

Fig. 12 Schematic representation of the CVD setup, illustrating 3 sample zones A, B, and C, separated by 3 cm from each other. Zone C is in the center of the reactor. The corresponding SEM images of the deposited films at each sample zone are shown on *top*. Reproduced from [122] with permission from © 2012 The Royal Society of Chemistry

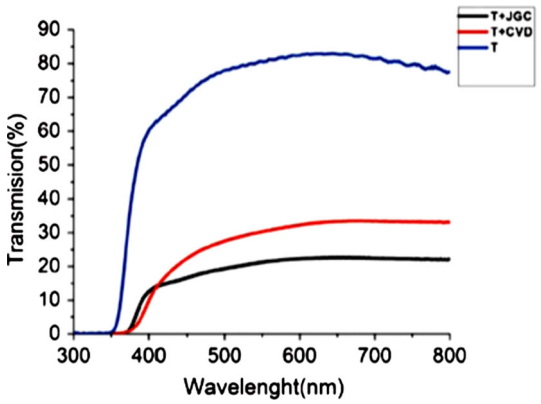

Fig. 13 Total (specular + diffuse) transmission of *T*, *T* + CVD, and *T* + JGC films on TEC15 substrates [70]. *T*, *T* + CVD, and *T* + JGC are representative of DSCs with 1 layer of transparent Dyesol paste, 1 layer of Dyesol paste plus 1 layer of CVD paste, and 1 layer of Dyesol paste plus 1 layer of JGC_PST-400C scattering paste, respectively. Reproduced from [122] with permission from © 2012 The Royal Society of Chemistry

very high sensitivity. The electrical properties of the films responded quickly to exposure to water in the atmosphere. The response times at 70 % RH for the TiO_2–SnO_2 films with 0, 5, 20, and 40 wt% SnO_2 content were 5, 6, 15, and 20 s, respectively. The shorter response time in the films with increased TiO_2 content seems to be due to the hydrophilic property of TiO_2.

Humidity sensors consisting of ceramic particles are quite stable for about 3 h at 60 % RH. Thin films of mixed oxides of CeO_2–TiO_2 with a Ce/Ti molar ratio of 0.5 have been obtained by a sonocatalytic sol–gel method [130]. The precursor sols consist of a mixture of $Ce(NH_4)_2(NO_3)_6$, titanium alkoxide ($Ti(OiPr)_4$), and isopropanol. The films were deposited by dip coating technique and calcined at 450 °C in an oxygen atmosphere. The films prepared from the precursor sols were subjected to electrochemical measurements (cyclic voltammetry and chronoamperometry), SEM, and AFM. CeO_2-TiO_2 films approximately 100 nm thick presented good electrochemical response under Li ion insertion. The cathodic and anodic charges at a scan rage of 50 mV/s were about 16 mC/cm^2, and the process was fully reversible. The values were constant for up to 4500 cycles, indicating good electrochemical stability of the films. The stability test and optical measurements confirm that the films can be used for ion storage (as counter electrodes) in electrochromic devices [130]. TiO_2 is considered a promising candidate for TSO applications, and the ion-storage and humidity sensing properties of this technologically important material could lead to very important TSO-related electronic/optoelectronic applications in electrochromic or smart windows, defrosting windows, and transparent functional window sensors, among others.

Spray pyrolysis

Spray pyrolysis is particularly attractive because it is scalable and a potential low-cost process suitable for highly uniform deposition of dense TiO_2 layers onto large-area substrates [107, 131–133]. Abou-Helala et al. [134] successfully prepared transparent TiO_2 thin films on glass substrates using spray pyrolysis technique. The films were amorphous at deposition temperatures up to 450 °C.

Table 3 Optical and electrical properties of TiO_2 thin films with dopant concentration synthesized by various growth techniques

Synthesis process	Dopant	% of doping	Transmittance (%) visible	E_g (eV) bandgap	Resistivity (Ω cm)	Carrier concentration (cm^{-3})	References	Remarks
Sputtering								
DC magnetron Sputtering	Nb	9.5 at.%	60–80 %	3.68	6.63×10^{-4}	10×10^{20}	[45]	Used various H_2 and O_2 flows
Pulsed laser deposition	Ta	–	80 %	3.63	8.7×1^{-4}	4.7×10^{21}	[58]	After post-annealing films were crystallized ~450–650
Chemical vapor deposition	–	–	76.5–71.5 %	–	–	1.8×10^{20}	[61]	–

Reproduced from [102, 103, 114] with permission from © 2005 Elsevier B.V., © 2007 Springer-Verlag, © 2011 Chinese Physical Society and IOP Publishing Ltd.

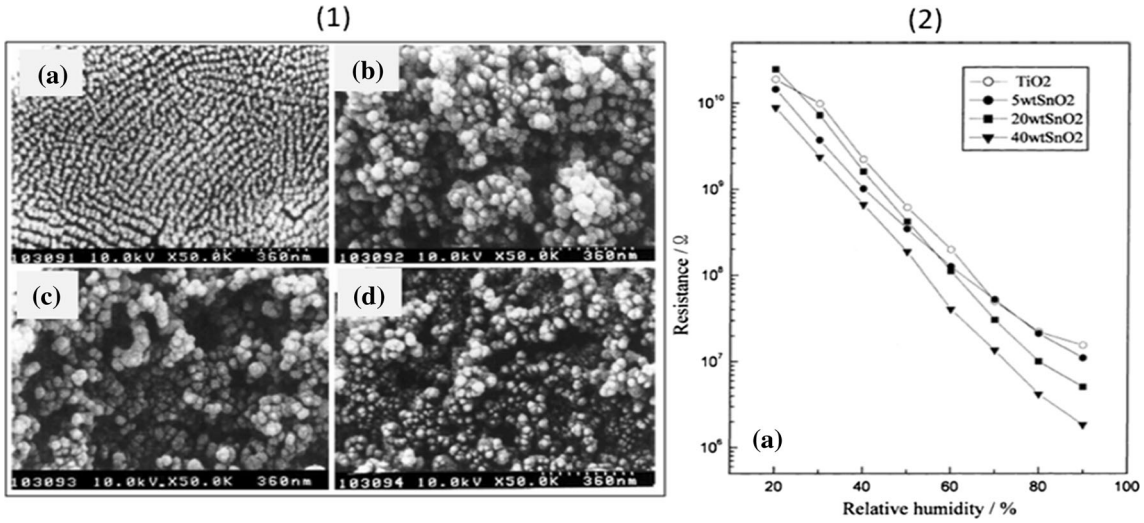

Fig. 14 **1** The SEM micrographs for TiO_2–SnO_2 films: (a) TiO_2–5 wt% SnO_2; (c) TiO_2–20 wt% SnO_2; (d) TiO_2–40 wt% SnO_2. **2** Humidity sensing properties for TiO_2–SnO_2 films with different SnO_2 contents. Reproduced from [129] with permission from © 2002 Published by Elsevier Science B.V.

Starting at about 550 °C, the films partially crystallized (anatase phase; Fig. 15).

The prepared films have good homogeneity with some porosity, which is suitable for photocatalytic applications. TiO_2 films can be prepared by spray pyrolysis at different substrate temperatures. The film thickness can be controlled by the number of spray pulses. Deposition or annealing at 500 °C results in anatase phase without contaminants. Annealing at 700 °C in air leads to crystalline anatase formation for films deposited below 400 °C. Films prepared at 435 °C are a mixture of anatase and rutile, and those obtained at 500 °C are rutile. Transparent TiO_2 anatase films grown at 375 °C and annealed at 700 °C show refractive indices of 2.2–2.4 and RMS roughness of 2.6 nm.

Cost-effective spray pyrolysis methods could be used to prepare TiO_2 films with an effective dielectric constant of 75 at 10 kHz [135]. TiO_2 thin film deposited by spray pyrolysis at a substrate temperature of 100 °C is amorphous, but when annealed at 400 °C, it changes phase to anatase with sharp XRD peaks showing crystallization as temperature increases. XRD studies showed that after annealing, the films were predominantly anatase with characteristic (101), (112), and (204) planes [135]. Table 4 compares the properties of TiO_2 thin films prepared by sol–gel and spray pyrolysis methods.

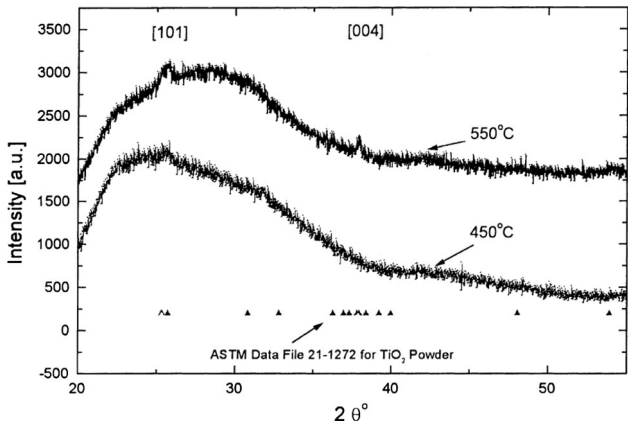

Fig. 15 XRD of TiO_2 films at different deposition temperatures and 10 min spray time. Reproduced from [134] with permission from © 2002 Published by Elsevier Science B.V.

Fabrication of p-type TiO_2

One of the efficient ways to modify the physical and chemical properties of TiO_2 is doping with other elements. However, the low electrical n-type semiconductivity of TiO_2 inhibits its practical implementation as a conductometric sensor. The addition of foreign atoms into a TiO_2 host such as Sn, Cr, Nb, W, and Mo has been widely studied to improve gas sensing behaviors [136–145]. p-type conductivity in TiO_2 can be achieved by doping with a suitable acceptor (Cr^{3+}, Fe^{3+}, Ni^{2+}, or Co^{+2}) at various concentrations [146–153]. Cation doping provides additional bands within the bandgap of TiO_2 for easy charge transportation. This can also be used to optimize charge injection and transport for efficient organic light-emitting devices [154] and to reduce the turn-on voltage in optoelectronic devices [155].

Bally et al. [156] prepared Fe-doped TiO_2 thin films by reactive RF sputtering (power-700 W) with deposition rates between 0.2 and 0.4 Å/s under a pressure of 10^{-1} Pa in a mixed Ar and O_2 atmosphere (33 % of oxygen). Silicon, glass, and indium tin-oxide (ITO)-coated glass substrates were heated to 260 °C during the deposition. The target was a metallic titanium disk (99.5 % purity, 60-mm diameter). Holes drilled into the titanium target (3-mm diameter) were filled with iron oxide powder to obtain Fe-doped TiO_2 thin films. The iron doping induces transformation from anatase to rutile without amorphization for doping lower than 1.3 at.%. The transition from n-type to p-type electrical conduction occurs with iron concentration around 0.13 at.%.

The highest p-type conductivity reached at room temperature is 10^{-6} S/m. The dispersion of the permittivity with frequency indicates that the electrical conduction of the thin films is inhomogeneous. The influence of the iron atoms depends on the crystal structure of the oxide. The introduction of iron generates more oxygen vacancies in anatase than in rutile. A large fraction of the acceptors created by the iron atoms is compensated by the oxygen vacancies created by the same iron atoms. The results show that pure rutile TiO_2 doped with iron has higher p-type conductivity than mixed anatase/rutile TiO_2 iron-doped thin films.

Cr-doped TiO_2 could exhibit p-type properties under high Cr doping (higher than 8 %) or high preparation temperature (up to 900 °C) [157, 158]. The high preparation temperature melts down TSO substrates, and the high Cr doping results in strong electron–hole recombination, which greatly hinders the fabrication and application of p-type Cr-TiO_2 photo-electrodes. As a photo-electrode material, TiO_2 has the advantages of large carrier diffusion length ($\sim$1 mm), high chemical stability, and non-toxicity [159]. Based on the excellent PEC properties of TiO_2-related materials, p-type photo-electrodes are predicted to have high potential for use as a cathode for photo-reduction. Cao et al. [77] prepared p-type Cr-doped TiO_2 photo-electrodes on an ITO substrate using the PLD method. Figure 16 presents the STEM/SEM images with *I-V* characteristics of the films. A uniformly Cr-doped TiO_2 photo-electrode, an inner Cr-doped TiO_2 photo-electrode, and an inner Cr-doped TiO_2 photo-electrode with Pt loading were

Table 4 Properties of TiO_2 thin films with dopant concentration synthesized by sol–gel and spray pyrolysis

Synthesis process	Dopant	% of doping	Transmittance (%) visible	E_g (eV) bandgap	Resistivity (Ω cm)	Carrier concentration	References	Remarks
Sol–gel	Nb	12 at.%	–	–	0.5	–	[68]	Two different annealing processes (a) Three times vaccum annealing (b) Multi-round annealing
Spray pyrolysis	N	–	–	3.1–3.25	–	–	[76]	–

Reproduced from [124, 135] with permission from © 2011 Elsevier B.V., © 2012 Scientific & Academic Publishing

fabricated, and their PEC properties were discussed in detail (Fig. 17).

TiO_2-based mixed oxides have also been reported to show p-type semiconductivity and good visible transparency for interesting TSO applications. For example, Li et al. [160] prepared Ti–Al-V–O oxide nanofilms with anatase structures by anodization and annealing. Anatase TiO_2 nanofilms doped with Al and V were fabricated through anodic oxidation of Ti6Al4 V alloy and annealing treatment. The anodic substrate was Ti6Al4V alloy plate. Cast plate samples with dimensions of 10 × 10 × 1 mm were ground and polished with emery paper and ultrasonically cleaned with absolute alcohol. Finally, they were rinsed with deionized water and dried in a N_2 stream. All of the samples were anodized using a DC voltage stabilizer at 15 V for 1.5 h in electrolytes of 1 M NaH_2PO_4 containing 0.5 wt% HF. The as-anodized samples were annealed at either 450 °C or 550 °C for 1 h in air to obtain crystallized nanofilms.

Nanofilm sensors were fabricated using circular Pt electrodes and conductive wires for printed circuit board (PCB) assembly. During hydrogen sensing experiments, a Keithley 2700 multimeter (Cleveland, OH, USA) was used to test the resistance of the nanofilm sensor. The nanofilm sensors were tested in alternating atmospheres of air and 1000-ppm H_2 at temperatures ranging from 25 to 300 °C. Annealing at different temperatures resulted in different hydrogen sensing performance. Al and V doping reduced the bandgap of TiO_2 oxide. The Al- and V-doped anatase nanofilms demonstrated p-type hydrogen sensing characteristics, which was quite different from the undoped TiO_2 nanotubes (Fig. 18). Hydrogen sensing properties of the oxide nanofilms were tested with operating temperature ranging from 25 to 300 °C. The resistance of the Ti–Al–V–O nanofilm sensors tested in the hydrogen atmosphere was recorded. The response ($\Delta R/R_0$) of the nanofilm sensor is defined as follows:

$$\Delta R/R = R - R_0/R_0 \times 100\,\%, \tag{3}$$

where R_0 is the original resistance of the sensor before exposure to the hydrogen-containing atmosphere, and R is the sensor resistance after exposure to or removal of the hydrogen-containing atmosphere. The Ti–Al–V–O nanofilms annealed at 450 °C demonstrated sensitivity to

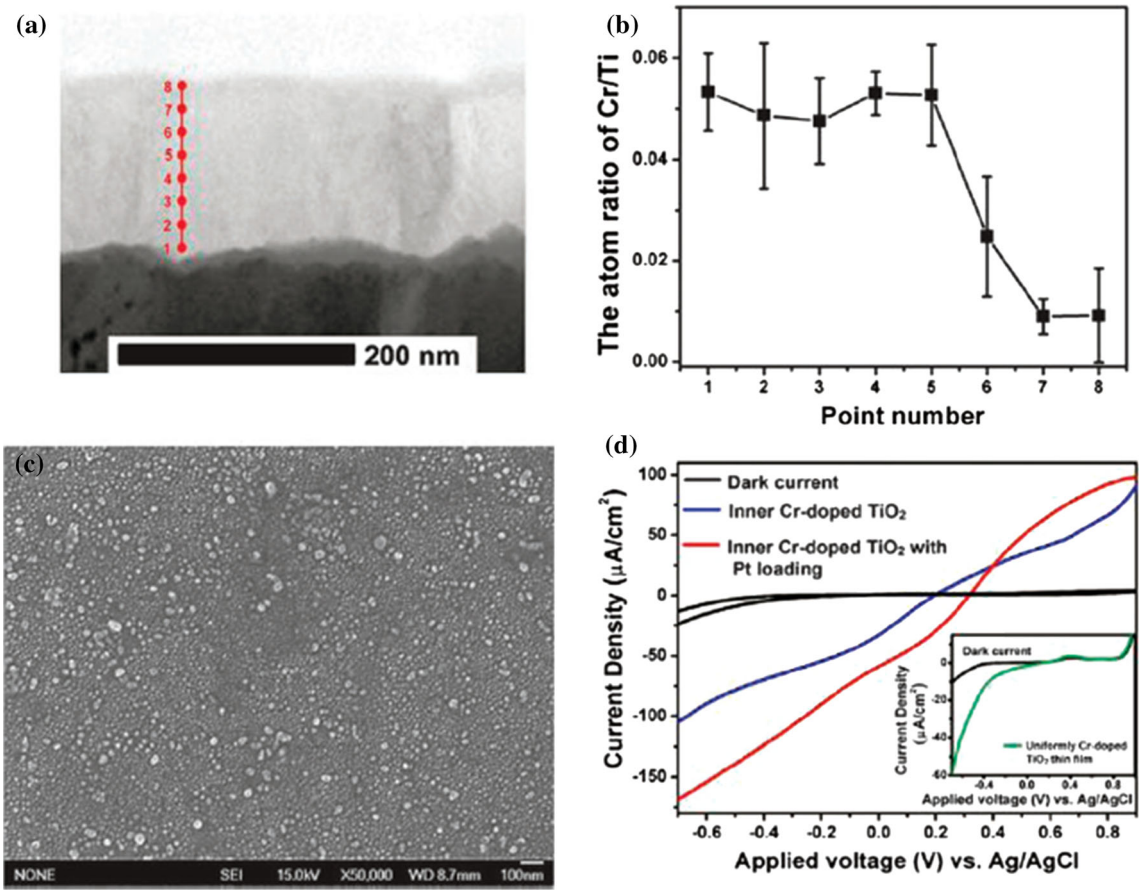

Fig. 16 **a** STEM cross-section image of the inner Cr-doped TiO_2 thin film; **b** atom ratio of Cr/Ti at different thicknesses of the TiO_2 layer; **c** SEM image of the Pt-loaded inner Cr-doped TiO_2 thin film **d** the *I–V* curves of the as-prepared thin films. The *inset* shows the *I–V* curves of the uniformly Cr-doped TiO_2 thin film. Reproduced from [77] with permission from © 2013 The Royal Society of Chemistry

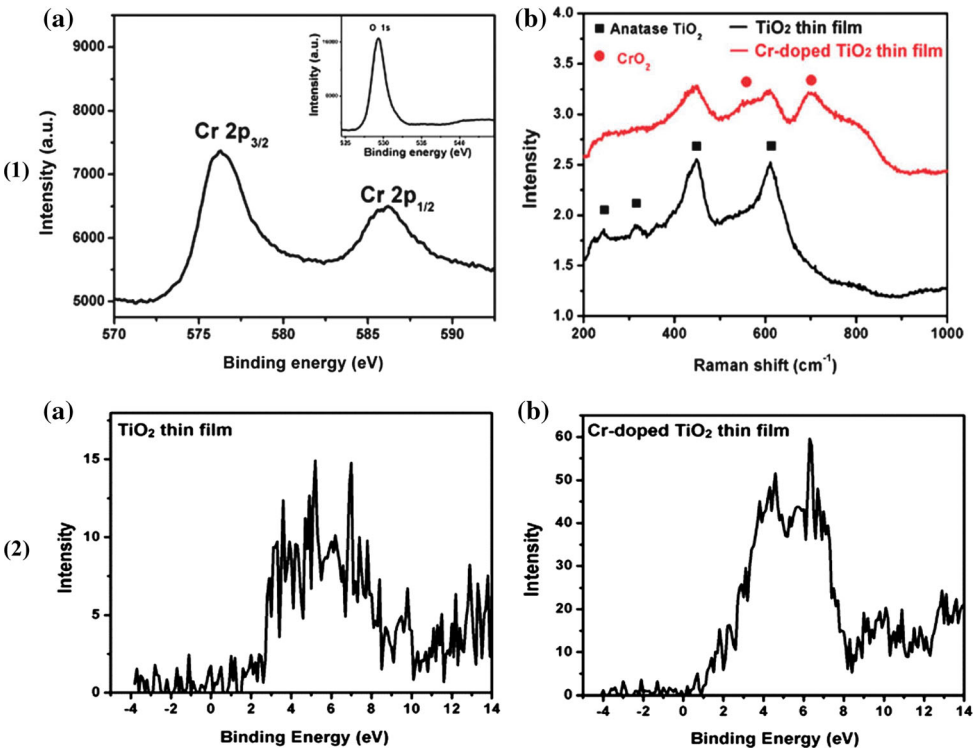

Fig. 17 **1**(a) XPS spectrum of Cr 2p in the uniformly Cr-doped TiO_2 thin film; *inset* shows the XPS spectrum of O 1s; (b) Raman spectra of the uniformly Cr-doped TiO_2 thin film and TiO_2 thin film. **2**(a) XPS spectrum of the TiO_2 thin film at the valence band region; (b) XPS spectrum of the uniformly Cr-doped TiO_2 thin film at the valence band region. Furthermore, by utilizing the local doping strategy and Pt loading, the PEC activity of the as-prepared p-type Cr-doped TiO_2 photo-electrodes was improved significantly. Reproduced from [77] with permission from © 2013 The Royal Society of Chemistry

1000-ppm H_2 at elevated operating temperatures, while Ti–Al–V–O nanofilms annealed at 550 °C had good sensing response at both room temperature and elevated temperatures.

Similarly, Sieradzka et al. [161, 162] reported a p-type transparent Ti–V oxides semiconductor thin film obtained by reactive magnetron sputtering technique. The sputter target was Ti pellets combined with V metallic foils, and the sputtering was performed in an oxygen-diluted Ar atmosphere with special conditions of the magnetron power to enhance the nucleation energy. A nearly 334-nm-thick film of Ti–V mixed oxide was deposited on glass, Si, and SiO_2 substrates. The optical transmittance spectra depict more than 60 % visible transparency for the Ti–V mixed oxide thin film, and electrical measurements reveal thermally activated conduction. This is often found in semiconductor thin films with considerably higher room temperature conductivity over undoped film, indicating potential applications in transparent electronics (Fig. 19). The p-type conductivity of the mixed oxide film was confirmed by thermopower measurements, and the room temperature Seebeck coefficient was +685 μV/K. The p-type semiconductivity of this Ti–V mixed oxide film is considered to come from the reduced oxidation state of V (+3 valance state of V_2O_3), which manifests vanadium vacancies that act as acceptor levels and introduce holes in the VB.

The same group further verified the p-type semiconductivity of their Ti–V mixed oxide film by fabricating an *n*-Si/*p*-Ti–V oxide heterojunction to show rectifying characteristics (Fig. 19). Although the use of Si as the *n*-layer is restricted in transparent diodes, some well-known *n*-TSOs (like ITO, ZnO, SnO_2, and TiO_2) can potentially be used in transparent electronics. Sieradzka et al. also reported multi-element doping into rutile TiO_2 to observe inversion in the semiconductivity of the magnetron sputtered thin film [163]. Simultaneous doping of Tb and Pd into TiO_2 (TiO_2:Tb + Pd) produces p-type semiconductivity, whereas Eu and Pd doping (TiO_2: Eu + Pd) produces an n-type thin film. Both films showed considerably high visible transparency and carrier concentrations for potential use in TSO applications.

Properties

Structures

There are four commonly known polymorphs of TiO_2 found in nature: anatase (tetragonal), brookite (orthorhombic), rutile (tetragonal), and TiO_2 (B) (monoclinic) [164–168]. Among the many poly types of TiO_2, the technologically important crystal structures are rutile and anatase (Fig. 20). Although TSOs have been investigated for many years, the mechanisms accounting for their electrical and optical properties are still somewhat poorly understood. Over the last few years, TiO_2 has gained increasing attention as a TSO material after by Furubayashi

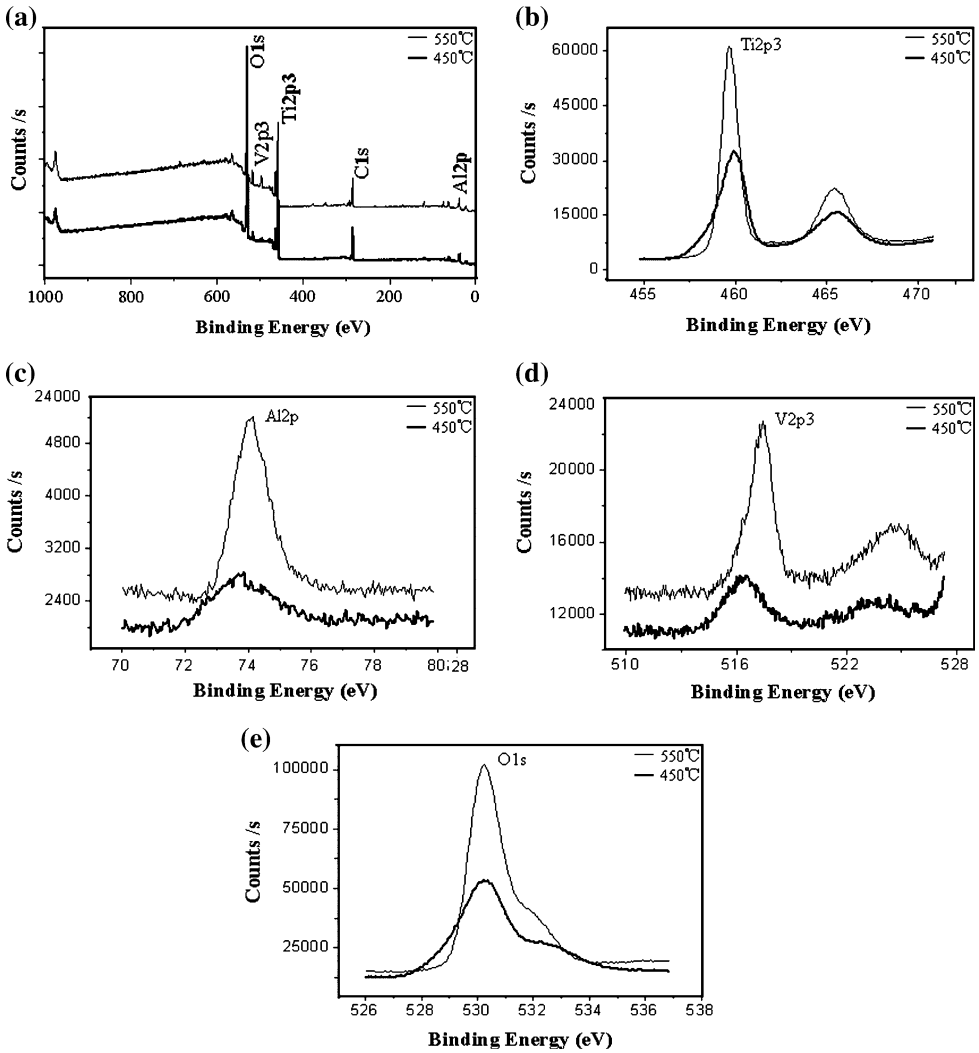

Fig. 18 XPS analyses of the Ti–Al–V–O oxide nanofilms annealed at different temperatures. **a** Deconvolution of survey spectrum and **b** Ti 2p3, **c** Al 2p, **d** V 2p3, **e** O 1s scan curves. Reproduced from [160] with permission from © 2013 licensee Springer

et al. produced an Nb-doped anatase TiO_2 film with excellent conductivity and transmittance comparable to ITO. [44]. The advantages of anatase TiO_2 as a TSO include relatively low effective mass, low cost, and stability in a hydrogen plasma atmosphere, which is used to produce solar cells. Undoped anatase is an anisotropic tetragonal insulator (a¼ 0.378 nm and c¼ 0.952 nm) with a bandgap of 3.2 eV [44].

Rutile

Rutile TiO_2 has a tetragonal structure and contains 6 atoms per unit cell (Fig. 20b). The TiO_6 octahedron is slightly distorted [81, 169–171]. The rutile phase is stable at most temperatures and pressures up to 60 kbar, where TiO_2(II) becomes the thermodynamically favorable phase [172]. Anatase and brookite structures transform to the rutile phase after reaching a certain nanoparticle size, with the rutile phase becoming more stable than anatase for particle sizes greater than 14 nm [173]. Once the rutile phase forms, it grows much faster than the anatase. The activity of the rutile phase as a photocatalyst is generally very poor. However, it was suggested that the rutile phase can be active or inactive, depending on its preparation conditions [81].

Anatase

Anatase TiO_2 also has a tetragonal structure, but the distortion of the TiO_6 octahedron is slightly larger [167, 174]. The anatase phase is more stable than the rutile at 0 K, but the energy difference between these two phases is small (2–10 kJ/mol) [175]. The photoreactivity is increased by the slightly higher Fermi level, lower capacity to adsorb oxygen, and higher degree of hydroxylation in the anatase phase [176]. The reactivity of (001) facets is greater than that of (101) facets in an anatase crystal [177]. Uniform anatase crystals containing 47 % (001) facets were synthesized using hydrofluoric acid as a morphology-controlling agent [178].

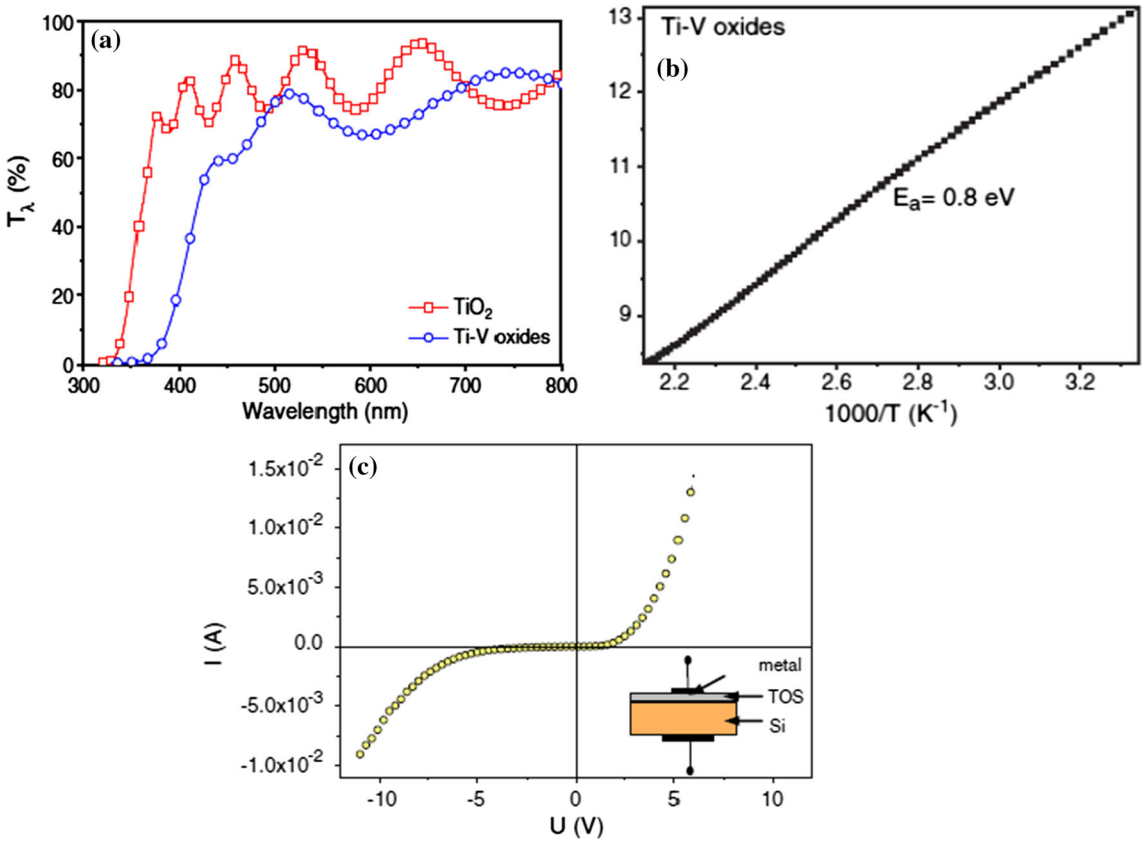

Fig. 19 **a** Transmission spectra of TiO_2 and Ti–V oxides thin films, **b** Temperature-dependent resistivity measurements of Ti–V oxides thin film deposited on glass, **c** *p*-TSO/*n*-Si heterojunction based on Ti–V oxides thin films. Reproduced from [161] with permission from © 2011 Elsevier B.V.

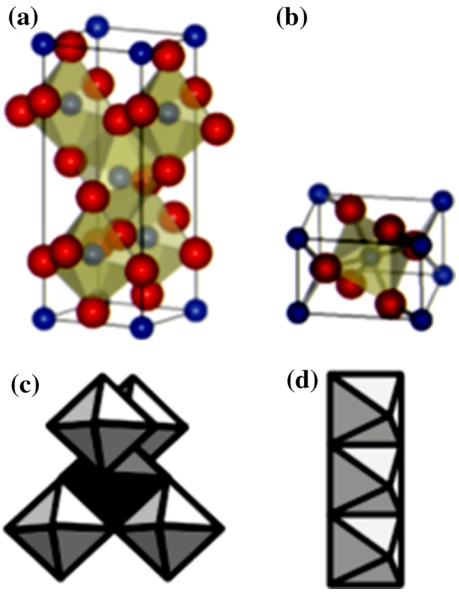

Fig. 20 Crystal structures of **a** anatase and **b** rutile, and a schematic representation of the TiO_6 networks in **c** anatase and **d** rutile. *Red* and *blue spheres* denote Ti and O atoms, respectively. Reproduced from [41] with permission from © 2010 Wiley-VCH Verlag GmbH & Co. KGaA, Weinheim (Color figure online)

Brookite

Brookite TiO_2 belongs to the orthorhombic crystal system. Its unit cell is composed of 8 formula units of TiO_2 and is formed by edge-sharing TiO_6 octahedra. It is more complicated, has a larger cell volume, it is the least dense of the 3 forms, and it is not often used for experimental investigations. TiO_2 is a large-band semiconductor with bandgaps of 3.2, 3.02, and 2.96 eV for the anatase, rutile, and brookite phases, respectively [179]. The VB of TiO_2 is composed of the 2*p* orbitals of oxygen hybridized with the 3*d* orbitals of titanium, while the CB is only the 3*d* orbitals of titanium [180].

Raman spectroscopy

Raman spectroscopy is a powerful tool in studying microstructure or nanostructure of materials. Depending on various vibrational modes, different phases can be obtained in a mixed crystal. Hence, this technique is promising for microstructural characterization and phase identification of TiO_2 [181–183]. Additionally, Raman spectroscopy can

also be used to identify and quantify the amorphous and crystalline TiO_2 phases [183]. Figure 21 presents typical Raman spectra of amorphous, brookite, anatase, and rutile TiO_2. As expected, amorphous TiO_2 has the lowest Raman activity and does not show any significant Raman peak except for some broad bands.

Temperature treatments convert the amorphous TiO_2 into crystalline phases by the evolution of sharp Raman peaks, as shown in the figure. The Raman spectrum of rutile TiO_2 shows some sharp and broad peaks assigned with different Raman-active lattice vibrations: B_{1g} (144 cm^{-1}), B_{1g} (236–242 cm^{-1}), E_g (300–400 cm^{-1}), $E_g + A_{1g}$ (unresolved doublet around 440–446 cm^{-1}), B_{2g} (589 cm^{-1}), A_{1g} (610 cm^{-1}), and B_{2g} (827 cm^{-1}) [169, 184, 185]. Although phonon vibrations corresponding to E_g @ 300–440 cm^{-1}, B_{2g} @ 589 cm^{-1}, and B_{2g} @ 827 cm^{-1} are masked either by neighboring stronger peaks or high background noise, several groups reported significant intensities of these peaks, which are hence assigned here for completeness [183].

For anatase TiO_2, the factor group analysis reveals six Raman-active modes (one A_{1g}, two B_{1g}, and three E_g) [184], which were also experimentally observed by various groups and assigned as follows [181, 182, 185–187]: E_g (144/147 cm^{-1}), E_g (197 cm^{-1}), B_{1g} (397/399 cm^{-1}), $A_{1g} + B_{1g}$ (unresolved doublet around 513–519 cm^{-1}), E_g (639/640 cm^{-1}). According to space group theory, 36 Raman-active modes are predicted for Brookite TiO_2 (nine A_{1g}, nine B_{1g}, nine B_{2g} and nine B_{3g}) [188–190], out of which 17 bands were experimentally observed by several groups and assigned as follows: A_{1g} (127/128, 155/156, 194, 245/246, 412, 637/638 cm^{-1}), B_{1g} (133, 213/214, 322/323, 501/502 cm^{-1}), B_{2g} (365/366, 395/396, 460/461, 583 cm^{-1}), and B_{3g} (172, 287/288, 545 cm^{-1}) [191–195]. Other Raman modes are masked by a high level of coincidence and weak band intensities.

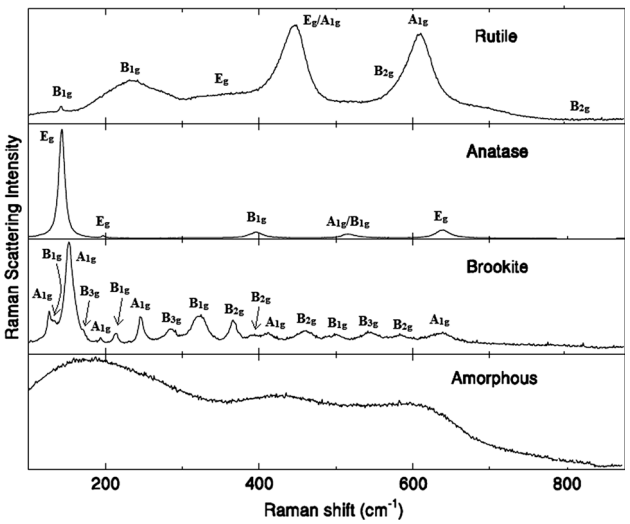

Fig. 21 Room temperature Raman spectra of the various phases of Titania. Reproduced from [188] with permission from Gonzalez RJ, Ph.D. Thesis, Virginia Polytechnic Institute and State University (1996) Raman, Infrared, X-ray, and EELS Studies of Nanophase Titania

Apart from phase identification, Raman characterization is also used for the determination of size and non-stoichiometry of TiO_2 nanocrystals [182, 186, 196–201], both of which are very important in TSO-related applications. Broadening and shifting of Raman bands are observed when particle dimensions change or oxygen deficiency is induced in the TiO_2 crystal lattice (also, to some extent, strain, non-homogeneity of the size distribution, and anharmonic effects due to temperature increase can contribute to changes in the peak position and shape [182]). Regarding the size effect, Raman bands broaden and blue-shift with decreasing nanocrystal dimension d [187]. In a low-dimensional nanocrystal of size d, the phonon wave vector (k) is subjected to a k-space uncertainty that is inversely proportional to the nanocrystal dimension ($1/d$). Thus, the "infinite-crystal" k-space selection rule is replaced by a relaxed version with order $1/d$, and instead of only the $k = 0$ mode of a phonon branch being Raman-active (for a Raman-allowed mode symmetry), all modes of the phonon branch within a range of k values (approximately $k = 0$–$1/d$) become Raman-active, leading to broadening of the Raman bands with decreases in the nanocrystal dimension. The blue-shift of the bands is due to the effect of smaller particle size on the force constants, where a volume contraction occurs within the nanoparticles, resulting in decreased interatomic distances and an increase in the force constant. This leads to shifting of the Raman bands toward a higher frequency region [201].

Knowing the phonon dispersion relation, it is possible to estimate the crystallite sizes from the Raman shift and broadening. In particular, this phonon confinement effect is more dominant at low frequency, so it is possible to determine the size of nanoparticles from a measurement of the maximum of the low frequency Raman band [201–203]. Additionally, because of the increase in the surface-to-volume ratio at the nanoscale, the surface modes become dominant as particle size decreases. This technique provides valuable information about the effects of the finite size of the nanoparticles on the surface modes, which means that new bands can be observed [200]. Several groups experimentally observed this size effect in nanocrystalline TiO_2 [182, 186, 200].

Electro-optical properties

TSO materials are electrically conductive due to either intrinsic defects (oxygen vacancies or metal interstitials) or extrinsic dopants (typically a higher-valency metal). The

extrinsic dopant concentration of the well-developed TSOs typically varies from 10^{20} to 10^{21} cm^{-3}. Usually, the resistivity, $\rho = 1/\sigma$, rather than the conductivity, σ, is used as the figure of merit, which is on the order of 10^{-4} Ω cm for many TSO materials of practical viability. While the carrier concentration in TSO is limited by the solubility of dopants, the mobility μ is limited by scattering of the charge carriers in the lattice. Several electron scattering mechanisms could be operative in TSO, such as scattering by ionized impurities, neutral centers (point defects and their complexes), thermal vibrations of the lattice (acoustical and optical phonons), structural defects (vacancies, dislocations, stacking faults), and grain boundaries, depending on the carrier concentration and crystal quality of the material [204–214].

The transmission window of TSOs is defined by two imposed boundaries. One is in the near-UV region and determined by the effective bandgap E_g, which is blue shifted due to the Burstein–Moss effect [215, 216]. Owing to high electron concentrations, the absorption edge is shifted to higher photon energies. The sharp absorption edge near the band edge typically corresponds to the direct transition of electrons from the VB to the CB. The other is in the near-infrared (NIR) region due to the increase in reflectance caused by the plasma resonance of electron gas in the CB.

The absorption coefficient α is very small within the defined window, and transparency is consequently very high [13, 217–220]. The positions of the two boundaries defining the transmission window are closely related to the carrier concentration. For TSOs, both boundaries defining the transmission window shift to shorter wavelength with the increase of carrier concentration. The plasma frequency at which the free carriers are absorbed has a negative correlation with the free carrier concentration. The shift in the near-IR region is more pronounced than in the near-UV region. Therefore, the transmission window becomes narrower as the carrier concentration increases. This means that both the conductivity and the transmittance window are interconnected since the conductivity is also related to the carrier concentration, as discussed above. Thus, a compromise between material conductivity and transmittance window is needed, and the specifics are application dependent. For LED applications, the transparency is needed in only a narrow range around the emission wavelengths, while solar cells require high transparency in the whole visible solar spectral range. Therefore, for photovoltaics, the carrier concentration should be as low as possible for reducing the unwanted free carrier absorption in the IR spectral range, while the carrier mobility should be as high as possible to retain a sufficiently high conductivity.

Among the many polytypes of TiO_2, the most technologically important crystal structures are rutile and anatase (Fig. 20). Both have tetragonal symmetry and can be described as networks of TiO_6 octahedra, but the two structures differ in the distortion and linkage of these octahedra. In the anatase structure, each octahedron is in contact with eight neighbors (four shared edges and four shared corners), as shown in Fig. 20, while the coordination number of rutile is 10 (two shared edges and eight shared corners) (Fig. 20d). Anatase TiO_2 tends to incorporate oxygen vacancies, which can be expressed as TiO_2-d. The amount of oxygen vacancies in d can be controlled by adjusting film growth or annealing conditions. The oxygen vacancies generate n-type carriers in the Ti-3d CB, so the resistivity (ρ) of TiO_2 can be decreased by introducing oxygen vacancies. However, oxygen-deficient TiO_2-d films lose their transparency and thus cannot be used as a TSO.

In addition to the introduction of oxygen vacancies, the substitution of Nb for Ti could introduce charge carriers. Indeed, Nb doping in rutile TiO_2 decreases ρ by a factor of more than 5500 [221], although the minimum ρ value ($\sim 10^{-2}$ Ω cm at room temperature) [222, 223] is insufficient for TSO applications due to the low electron mass ($\ll 1$ m_0) in rutile [224]. Anatase has a higher mobility than rutile and is more suited to TSO applications. However, the transport properties of anatase have not been thoroughly studied since anatase is a thermodynamically metastable structure and it is difficult to grow single crystals in bulk form. Lévy et al. [225] first reported single-crystal growth of anatase using chemical vapor transport. They measured the optical and transport properties and obtained ρ on the order of 10^{-1} Ω cm with an electron mobility exceeding 600 cm^2/V_s at 50 K [226]. Single crystals of Nb-doped anatase TiO_2 were investigated by Mulmi et al. [226], who reported ρ values of 5×10^{-2} Ω cm. Their ρ versus temperature (ρ–T) curve exhibited semiconducting behavior, possibly due to the low Nb concentration. Anatase TiO_2 films have been fabricated by various techniques [227, 228], as discussed in "Basic electronic band structure of TSO" section.

Maghanga et al. [228] prepared transparent and conducting thin films of TiO_2:Nb on glass by reactive DC magnetron sputtering in $Ar + O_2$ atmosphere at 8.5 mTorr pressure. Post-deposition annealing in vacuum at 450 °C led to good electrical conductivity and optical transparency. Sputtering was conducted with 220 W of power applied to the Ti target. The power applied to the Nb target was between zero and 45 W to make films with different Nb contents. Sputtering was performed on glass microscope slides, and Si plates were positioned ~13 cm below the targets on a rotatable holder. A small amount of H_2 was added to avoid target poisoning. The substrates were maintained at 330 °C during sputtering, as measured by a thermocouple. After the deposition, the films were first

allowed to cool within the sputter unit and then vacuum-annealed at 450 °C for 30 min in the deposition chamber.

Figure 22a, b show a comparison between experimental spectra on $R(\lambda)$ and $T(\lambda)$ for two Nb concentrations with the best fit obtained with the Drude–Brendel model [229]. The agreement between the experiment and the fitted data is generally good with standard deviation between 0.0001 and 0.0004 according to the fitting software. Some inconsistency occurred in the bandgap region and the long wavelength region for samples with more than 2 at.% Nb. This is due to the approximate nature of Drude–Brendel Equations for the case of complex conducting oxides.

Figures 22c, d show $n(\lambda)$ and $k(\lambda)$ for TiO_2 and for TiO_2:Nb with two different doping levels. The undoped film has dielectric behavior with $n \approx 2.2$, irrespective of wavelength for $\lambda > 500$ nm. For the Nb-doped films, the optical constants are qualitatively different. In this case, $k(\lambda)$ increases with λ, as expected for a metallic material, while $n(\lambda)$ drops gently with larger λ. These effects increase the magnitude with increasing doping level of Nb. This study summarized the combined effect of doping and post-deposition heat treatment, which inhibited the formation of the rutile phase of TiO_2. The optical properties were well illustrated by Drude free electron theory for frequencies below the bandgap in the case of doped films. Analysis of the individual contributions to the optical constants demonstrated that the Drude contribution increases with increasing Nb content. Good harmony was found between measured DC resistivity and the resistivity obtained from optical data.

A majority of researchers have reported that rutile TiO_2 has both direct and indirect bandgap values around $\sim$3.6 and $\sim$3.10 eV, respectively [230, 231]. However, there is controversy over the exact bandgap transition (direct or indirect) within anatase TiO_2. Although many groups predicted indirect transition [232], few have reported direct bandgap transition within nanostructured anatase TiO_2 [233, 234]. In either case, the reported values of the bandgap of anatase TiO_2 fall within the range of 2.86–3.34 eV [232]. For Brookite TiO_2, theoretical and experimental works reported bandgap values both smaller and larger than that of anatase. For natural brookite mineral, the bandgap is reported to be indirect, but there is disagreement on whether the optical response of synthetic

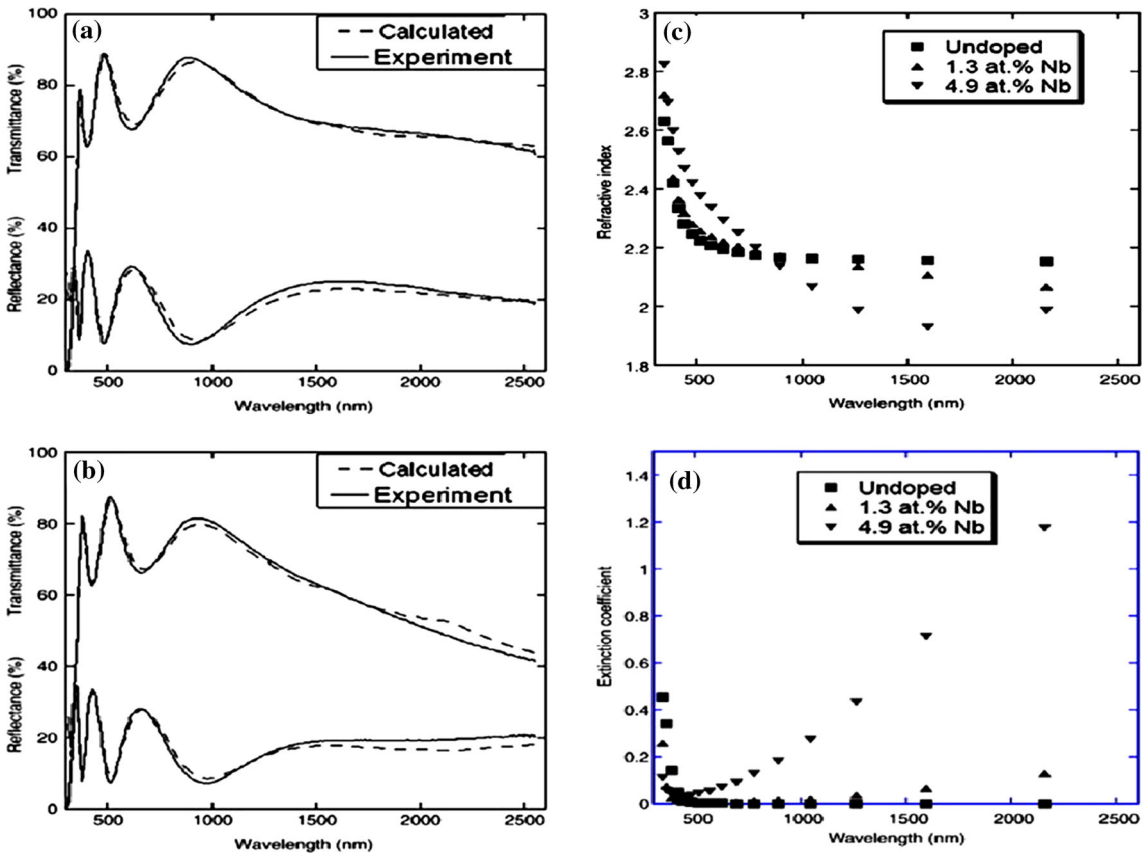

Fig. 22 Spectral normal transmittance (*upper set of curves*) and near-normal reflectance (*lower set of curves*) for sputter-deposited and annealed TiO_2:Nb films with **a** 1.3 at.% Nb and **b** 2.1 at.% Nb. Spectral refractive index, $n(\lambda)$, **c** and extinction coefficient, $k(\lambda)$ **d** for sputter-deposited and annealed TiO_2:Nb films with the shown Nb contents. Reproduced from [228] with permission from © 2009 Elsevier B.V.

Brookite is attributable to direct or indirect transitions. In any case, the experimentally reported bandgap values lie within the range of 3.1–3.4 eV [192, 194], but in nanostructured brookite TiO_2, direct band transition with considerably high bandgap values (>3.4 eV) is reported, which is very useful for TSO applications [235]. Generally, a lower bandgap of TiO_2 (less than the energy of a blue photon (~3.1 eV)) is suitable for visible light-induced photocatalysis, whereas higher bandgap (>3.1 eV) is preferred for TSO applications.

Apart from the Burstein–Moss effect of the blue-shift of the fundamental absorption edge discussed earlier, the quantum size effect is also used to enhance the bandgap of TiO_2 nanostructures for suitable TSO applications [48]. It is well known that in semiconductor nanocrystals, when the nanoparticle dimension becomes comparable to the bulk excitonic Bohr radius, the bandgap of the nanomaterial tends to increase due to the quantum confinement effect [236–238]. By proper tuning of the particle size, one can effectively enhance the bandgap, and especially for TSO nanomaterials, this bandgap enhancement is very useful for photovoltaics and other TSO electronics [239–245].

Several groups theoretically predicted a strong confinement effect in rutile TiO_2 nanocrystals and proposed that around a crystallite size of 2.5 nm, the bandgap enhancement would be considerable [245, 246]. Similarly, several groups experimentally observed the size effect of bandgap enhancement in TiO_2 nanocrystals and reported a considerable increase in the bandgap to beyond 3.1 eV, which is suitable for TSO-related applications [246–249]. Several groups observed this quantum size effect in multilayer/heterojunction/nanocomposite TiO_2/Ge and TiO_2/ZnO films with interesting photovoltaic/photoconductive applications [250–252].

Defect chemistry in TiO_2

In general, stoichiometric metal oxides are considered to act insulators, and the corresponding bandgap values are effectively governed by the electropositivity and the outer-shell configuration of the metal ions (cations) within the lattice. For example, electropositive atoms without *d*-electron effects form wide-bandgap oxides that are essentially insulating. In contrast, metal atoms with *d*-electron effects form semiconducting oxide, and the defect mechanism plays an important role in the type of charge conduction within these types of metal oxides [70]. Metal excess (or oxygen deficiency) generally induces n-type semiconductivity, whereas metal deficiency (or oxygen excess) produces p-type semiconductivity in TSOs [253]. The general defect equilibrium for n- and p-type TSOs is respectively given by [253, 254]

$$O_O^X \leftrightarrow \frac{1}{2}O_2(g) + V_O^{2+} + 2e^- \quad (4)$$

$$\frac{1}{2}O_2(g) \leftrightarrow O_O^X + V_M^{2-} + 2h^+, \quad (5)$$

where O_O, V_O, V_M, *e,* and *h* denote lattice oxygen, an oxygen vacancy, metal vacancy, electron, and hole, respectively. Superscripts X, −, and + denote effective neutral, negative, and positive charge states, respectively. The equations indicate that for *n*-TSOs, lattice oxygen is diffused to the gaseous state to produce oxygen vacancy, thus creating excess electrons for charge transport. Similarly, for *p*-TSOs, excess oxygen is intercalated from the gaseous state into the lattice site of metal atoms to create metal vacancy, which is compensated by creation of holes for p-type conduction.

TiO_2 is a wide-bandgap semiconductor and a non-stoichiometric compound. The properties of TiO_2 include light absorption, charge transport, and surface adsorption, which are closely related to defect disorder. These properties play a significant role in the utilization of solar energy, the photocatalytic performance, and the electrochemical performance [255–257]. The defect disorder of TiO_2 has been considered in terms of oxygen vacancies, titanium interstitials, and titanium vacancies [254]. The equilibrium concentration of these defects is established instantly at the gas/solid interface, and their transport from the surface into the bulk is extremely slow. Therefore, prolonged time is required for their propagation into the lattice.

In general, TiO_2 nanocrystals are an intrinsically n-type semiconductor (*i.e.*, oxygen-deficient oxide), and studies showed that the imposition of excess (non-stoichiometric) oxygen may lead to p-type conductivity at high oxygen partial pressure [258]. The basic quantities describing the defect equilibria are the equilibrium constants. Kofstad [253] reported the equilibrium constants for the formation of oxygen vacancies and titanium interstitials in TiO_2, and the intrinsic electronic equilibrium constant was reported by Bak et al. [259]. These data have led to the derivation of the full defect disorder diagram of TiO_2 [260].

The general defect chemistry of undoped TiO_2 treated under elevated temperature can be represented in terms of oxygen vacancies, titanium interstitials, and titanium vacancies according to the following equilibria [261, 262]:

$$O_o^X \leftrightarrow V_O^{2+} + 2e^- + \frac{1}{2}O_2(g) \quad (6)$$

$$2O_O^X + Ti_{Ti} \Leftrightarrow Ti_i^{3+} + 3e^- + O_2(g) \quad (7)$$

$$O_2(g) \Leftrightarrow 2O_O^X + V_{Ti}^{4-} + 4h^+ \quad (8)$$

$$\text{nil} \Leftrightarrow e^- + h^+, \quad (9)$$

where Ti_{Ti} and Ti_i are the lattice interstitial Ti atoms, respectively (other terms were already defined for Eqs. (4)

and (5)). The equations make it apparent that the predominant non-stoichiometric defect in the undoped TiO_2 is the doubly ionized oxygen vacancies, which induce dominant electron conduction, and to some extent, metal vacancies try to induce hole conduction. That means undoped TiO_2 would contain both electrons and holes under high-temperature oxygen activity. But because of the strong electronegativity of the O-2*p* level, the holes will be localized around the oxygen ions and make the hole mobility very low (as discussed in "Basic electronic band structure of TSO" section), while mostly acting as traps that impair conduction [70]. In contrast, electrons at the CB will have considerably high mobility and induce intrinsic n-type characteristics in undoped TiO_2.

The equilibrium constants for the equilibria are explained by the following equations [261]:

$$K_1 \Leftrightarrow [V_O^{\cdot\cdot}]n^2p(O_2)^{1/2} \tag{10}$$

$$K_2 \Leftrightarrow [Ti_i^{\cdot\cdot\cdot\cdot}]n^3p(O_2) \tag{11}$$

$$K_3 \Leftrightarrow [V_{Ti}^{''''}]p^4p(O_2)^{-1} \tag{12}$$

$$K_i = np, \tag{13}$$

where $V_O^{\cdot\cdot} \equiv V_O^{2+}$; $V_{Ti}^{''''} \equiv V_{Ti}^{4-}$; $Ti_i^{\cdot\cdot\cdot\cdot} \equiv Ti_i^{3+}$ (according to Kröger–Vink notation [262]), n and p represent the concentrations of electrons and holes, and $p(O_2)$ is the oxygen activity (partial pressure). The equilibrium constant K_i is derived from the electrical conductivity data by Bak et al. [259], and K_3 has not been reported yet. The equilibrium constants K_1 and K_2 are estimated from thermogravimetric data from Kofstad [253].

From these equations, it becomes clear that $p(O_2)$ (oxygen activity/partial pressure) plays an important role in the non-stoichiometric defect and carrier compensation of undoped TiO_2, during sample preparation or annealing [262]. By changing the value of $p(O_2)$ during sample processing from an extremely low value (extremely reduced condition, $p(O_2) \sim 10^{-14}$ Pa) to a very high value (strong oxidizing condition, $p(O_2) \sim 10^3$ Pa) [261], the carrier conductivity and charge compensation in defect disorder can be tuned accordingly. For example, (a) at extremely reduced conditions, the dominant charge carrier will be electrons, which would compensate some of the predominant tri-valent Ti interstitials ($n = 3[Ti_i^{\cdot\cdot\cdot\cdot}]$). (b) In strongly reduced conditions, the dominant charge carrier will be electrons, which would compensate predominant oxygen vacancies ($n = 2[V_O^{\cdot\cdot}]$). (c) In reduced conditions, the dominant charge carrier will again be electrons, which would compensate some of the oxygen vacancies, while the rest will be compensated by Ti vacancies ($[V_{Ti}^{''''}] = \frac{1}{2}[V_O^{\cdot\cdot}]$). (d) In oxidized conditions, the dominant charge carrier will be holes, which would compensate some of the oxygen vacancies while the rest will be compensated by Ti vacancies, and (e) in strongly oxidized conditions, the dominant charge carrier will again be holes, which would compensate the Ti vacancies ($p = [V_{Ti}^{''''}]$) [262]. Figure 23 shows a schematic representation of the effect of $p(O_2)$ on the concentration of both electronic and ionic defects in undoped TiO_2.

Regarding doped TiO_2, the concentrations of both electronic and ionic defects satisfy the lattice charge neutrality condition according to the following general equation [262]:

$$2V_O^{\cdot\cdot} + 3[Ti_{Ti}^{\cdot\cdot\cdot\cdot}] + [D^{\cdot}] + p = n + 4[V_{Ti}^{''''}] + [A'], \tag{14}$$

where $[D^{\cdot}]$ and $[A']$ are the concentrations of singly ionized donor-type and acceptor-type foreign ions introduced as dopants (or impurities), respectively. The defect equilibrium of Nb- and Ta-doped TiO_2 has been considered by several groups since metal-doped TiO_2 is very important for TSO applications [43, 44, 261]. The approximate defect equilibrium for Nb/Ta-doped TiO_2 can be represented as [261]

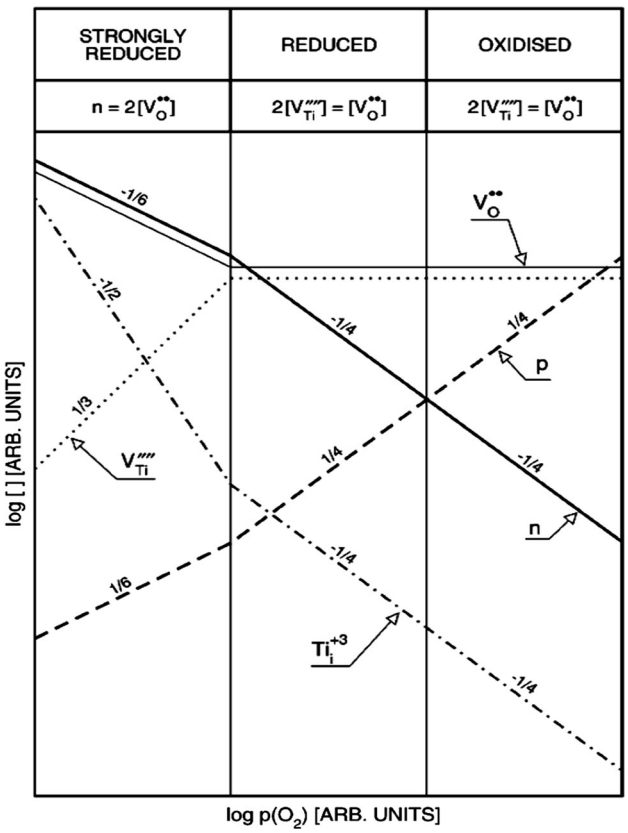

Fig. 23 Pictorial representation of the defect diagram based on simplified charge neutralities showing the effect of oxygen activity, $p(O_2)$ in undoped TiO_2 on the concentration of ionic and electronic defects. Reproduced from [260] with permission from © 2006 American Chemical Society

$$M_2O_5 \leftrightarrow 2M_{Ti}^{+} + 2e^{-} + 4O_O^X + \frac{1}{2}O_2(g), \quad (15)$$

where M is the pentavalent Nb^{+5} or Ta^{+5} cations incorporated into Ti lattice position (M_{Ti}^{+}) to create excess electrons for enhanced n-type semiconductivity. Similarly, for acceptor-type metal doping in TiO_2–TSOs, tri- and di-valent cation doping shows p-type semiconductivity in metal-doped TiO_2–TSOs [136–141]. The approximate defect equilibrium for tri-valent (M^{3+}: Cr^{3+}, Fe^{3+}) and di-valent (M^{2+}: Ni^{2+}, Co^{2+}) cation doping into a TiO_2 matrix can, respectively, be represented as

$$M_2O_3 \leftrightarrow 2M_{Ti}^{-} + 2h^{+} + 2O_O^X + \frac{1}{2}O_2(g) \quad (16)$$

$$2MO \leftrightarrow 2M_{Ti}^{2-} + 4h^{+} + O_O^X + \frac{1}{2}O_2(g), \quad (17)$$

where the cations are inserted into Ti lattice (M_{Ti}) positions to create excess holes for enhanced p-type semiconductivity.

Applications

Transparent devices have received considerable attention in recent years due to their potential applications in fields where traditional silicon-based techniques cannot be used, such as transparent displays, flexible displays, transparent transistors, organic solar cells, transparent super capacitors, and UV detectors [262–267]. As one of the most important wide-bandgap semiconductors, TiO_2 has been studied for use in transparent devices because of its outstanding physical and chemical properties. For example, TiO_2 transparent thin films would have a great impact in photoelectrodes [268], antireflection films, self-cleaning glass [267], and nonlinear optical devices [269]. The wide range of applications for TCO films in electronic devices has generated great interest in understanding the growth and characterization of these materials. These applications include flat-panel displays, low-e windows, thin-film solar cells, electrochromic devices, electromagnetic-shielding coatings, antennas for cars, radar protection for fighter planes, and heated windows [180, 270–273]. Below, we will discuss some of these applications of TiO_2 as an effective TSO material.

Heterojunction for transparent electronics

Thin-film transistors or field-effect transistors (FETs) based on TOSs have attracted considerable attention for their good transparency and high field-effect mobility [180, 271–274]. Most of the high-mobility oxide semiconductors show n-type conduction, and only a limited number of oxides exhibit p-type conduction with acceptable hole mobility. For example, *p*-NiO is used in DSSCs, despite its hole diffusion coefficient (10^{-8}–10^{-7} cm^2/s) being two orders of magnitude lower than that of TiO_2 [274]. Therefore, the higher conductivities of *p*-TiO_2 than NiO could certainly be beneficial for building efficient *p*-DSSCs. The p-type semiconductivity in TiO_2 can be achieved by suitable acceptor doping (Cr^{3+}, Fe^{3+}, Ni^{2+}, or Co^{+2}) with varying concentrations [146, 275–279]. Cation doping would provide additional bands within the bandgap of TiO_2 for easy charge transportation. This can also be used to optimize charge injection and transport for efficient organic light-emitting devices [148–154, 280–283] and reduce the turn-on voltage in optoelectronic devices [284].

Das et al. [282] reported on the heterojunction behavior of *p*-TiO_2 as an active material in bipolar field-effect transistor devices. Solution-processed field-effect transistor structures were fabricated by inserting a $Ba_{0.5}Sr_{0.5}TiO_3$ layer to form an assembly of Ag/ZnO/$Ba_{0.5}Sr_{0.5}TiO_3$/Ni^{2+}:TiO_2/*n*-Si (Fig. 24). The assembly registered an on-to-off current ratio as large as 10^3 with a very low off-state current $\sim 10^{-12}$ A. The low leakage current is attributed to the appreciably higher values of VB/CB off-set of the $Ba_{0.5}Sr_{0.5}TiO_3$/semiconductor heterojunction. A schematic representation of the device and a cross-sectional FESEM image of a ZnO/$Ba_{0.5}Sr_{0.5}TiO_3$/Ni_{2+}:TiO_2/*n*-Si FET assembly are shown in Figs. 24a, b, respectively. The thickness of the $Ba_{0.5}Sr_{0.5}TiO_3$/Ni_{2+}:TiO_2 combined layer is $\sim$100 nm. The average thickness of the $Ba_{0.5}Sr_{0.5}TiO_3$ layer is $\sim$10 nm from the AFM image (Fig. 24c) and depth profile (Fig. 24d) data. Table 4 shows the parameters obtained from the study. The FET behavior of the assembly was evaluated by calculating the sub-threshold swing, $SS = -d(V_{GS})/d(\log|I_{DS}|)$, which shows how efficiently the transistor executes on/off operations. A small *SS* is desired for fast switching performance. This device yielded SS = 370–680 mV per decade, which is comparable to a back-gated silicon nanowire FET (SS = 100–600 mV per decade).

The device response was studied as a function of temperature in the range of 25–175 °C. The hole diffusion coefficient and mobility of *p*-TiO_2 were calculated as $\sim 10^{-3}$ cm^2/s and $\sim$0.13–0.15 cm^{-2}/V s, respectively. Recently, Das et al. [283] reported a detailed study of consistent p-type conductivity in extrinsic TiO_2 upon doping with metal ions (i.e., Al^{3+}, Cr^{3+}, Ni^{2+}). The characteristic features of the samples were studied through XPS, UPS, and current–voltage responses to explain the p-type conductivity. The temperature-dependent performance of *p*-TiO_2 in heterojunction devices and the variations of different parameters were analyzed to evaluate the efficiencies of the FET assembly. X-ray photoelectron spectroscopy (XPS) showed shifting of VB edges with

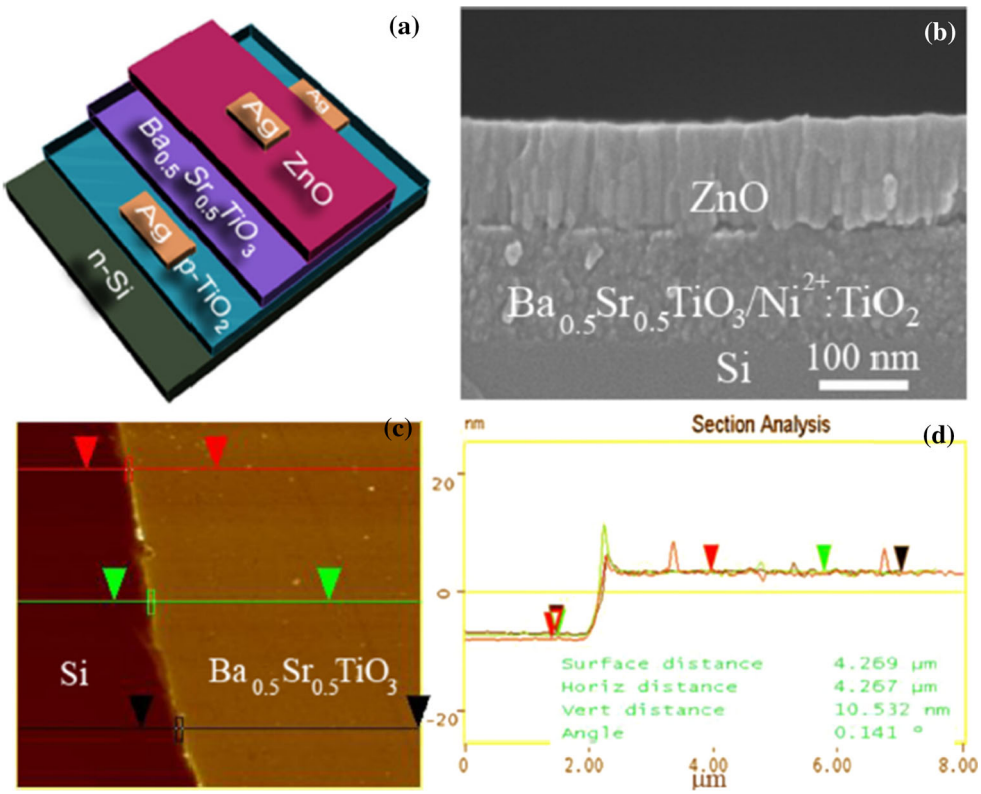

Fig. 24 **a** Schematic representation of the FET device with active *p*-TiO_2 channel, **b** cross-sectional FESEM image of the ZnO/$Ba_{0.5}Sr_{0.5}TiO_3/Ni^{2+}$:$TiO_2$/*n*-Si assembly, **c** AFM image, **d** depth profile of the $Ba_{0.5}Sr_{0.5}TiO_3$ layer with thickness of 10 nm. Reproduced from [282] with permission from © 2011 American Institute of physics

increasing doping concentration. The shape of the UPS spectra changes, and a doublet structure appears after inserting metal ions in the lattice of TiO_2. The position of the second peak is around 6 eV, and the width and shape of the spectra remain unaffected by the doping concentration, although it has an appreciable effect on the work function (W_0) (Table 5).

The metal-ion-doped TiO_2 films were employed as an active component in bipolar heterojunction devices, which had low turn-on voltage and rectification behavior. The crystallographic phase of the annealed samples was identified through X-ray diffraction data (Fig. 251a, b). The typical (101), (200), (211), and (204) lattice planes belonging to anatase TiO_2 are shown for $Al_xTi_{1-x}O_2$, $Cr_xTi_{1-x}O_2$, and $Ni_xTi_{1-x}O_2$ ($x = 0.01$) samples and $Ni_xTi_{1-x}O_2$ ($x = 0.01$, 0.05, 0.1) samples. Figure 25(2) shows the core level Zn2p peaks, VB spectra of ZnO, TiO_2, $Ni_{0.10}Ti_{0.90}O_2$, and the optical absorption spectra of $Ni_xTi_{1-x}O_2$ ($x = 0$, 0.01, 0.05, 0.1, 0.15, 0.2) with optical bandgap calculated in the range of 3.68–3.79 eV with increasing doping concentration (x). Figure 26(1a) shows the current response of heterojunction assembly at room temperature (25 °C) with sweeping bias voltage at different doping concentrations. The reverse current is insignificant while the forward current is appreciable, signifying p-type conductivity in the TiO_2 thin film.

The temperature-dependent response (25–150 °C) at a molar fraction of $x = 0.05$ is shown in Fig. 26(1b). The inset of each figure shows corresponding characteristics of ln(J) versus V. The p-type conductivity is ascribed to the acceptor level doping in TiO_2, which significantly influences the local chemical environment of Ti ions. When metal ions are incorporated into the TiO_2 lattice, the binding energy of each atom changes from the transfer of electrons from the Ti2p band to the core level of the dopant ions. Thus, the electronic structure gradually acquires more p-type conductivity with increasing doping concentrations [283].

Figure 26(2) shows a schematic representation of the studied FET devices with a dielectric layer sandwiched between the *n*-ZnO and *p*-TiO_2 layers, along with the current–voltage response under negative gate bias. The calculated μ_{sat} and D_h of *p*-TiO_2 for these FET devices at different temperatures are given in Table 6. Sarkar et al. [284] developed Type-II *p–n* junction three-dimensional Ag_2O/TiO_2 microspheres, which have been fabricated by assembling p-type Ag_2O nanoparticles on n-type TiO_2 3D microspheres. Ag_2O/TiO_2 microsphere nano-heterojunctions were obtained by hydrothermal synthesis of TiO_2 microspheres at 180 °C followed by photo-reduction of $AgNO_3$. Uniform assembly of Ag_2O nanoparticles was observed on the surface of the TiO_2, which produces a large number of *p–n* nano-heterojunctions. The Ag_2O/TiO_2 nanoheterostructure promotes charge separation due to the built-in electrostatic field at the junction and has higher photocatalytic activity than pure TiO_2.

Table 5 Details of the temperature-dependent parameters: saturation current (J_0), mobility (μ_{sat}), hole diffusion coefficient (D_h), mutual conductance (g_m), on–off ratio (I_{on}/I_{off}), and SS for ZnO/$Ba_{0.5}Sr_{0.5}TiO_3$/Ni^{2+}:TiO_2/*n*-Si assembly with $V_{GS} = -3$ V

	T (K)	J_0 (A/m^2)	μ_{sat} (cm^2/Vs)	D_h (cm^2/s)	$g_m = dI_{DS}/dV_{GS}$ ($\times 10^{-9}$) S	I_{on}/I_{off} ($\times 10^2$)	SS (V/decade)
$V_{GS} = -3$ V	348	0.00584	0.147	0.00441	3.004	0.412	0.368
	373	0.01878	0.144	0.00463	4.79	0.535	0.418
	398	0.08208	0.136	0.00467	12.74	0.405	0.513
	423	0.20271	0.154	0.00562	21.48	4.40	0.565
	448	0.68045	0.132	0.00503	25.56	2.00	0.681

Reproduced from [282] with permission from © 2011 American Institute of physics

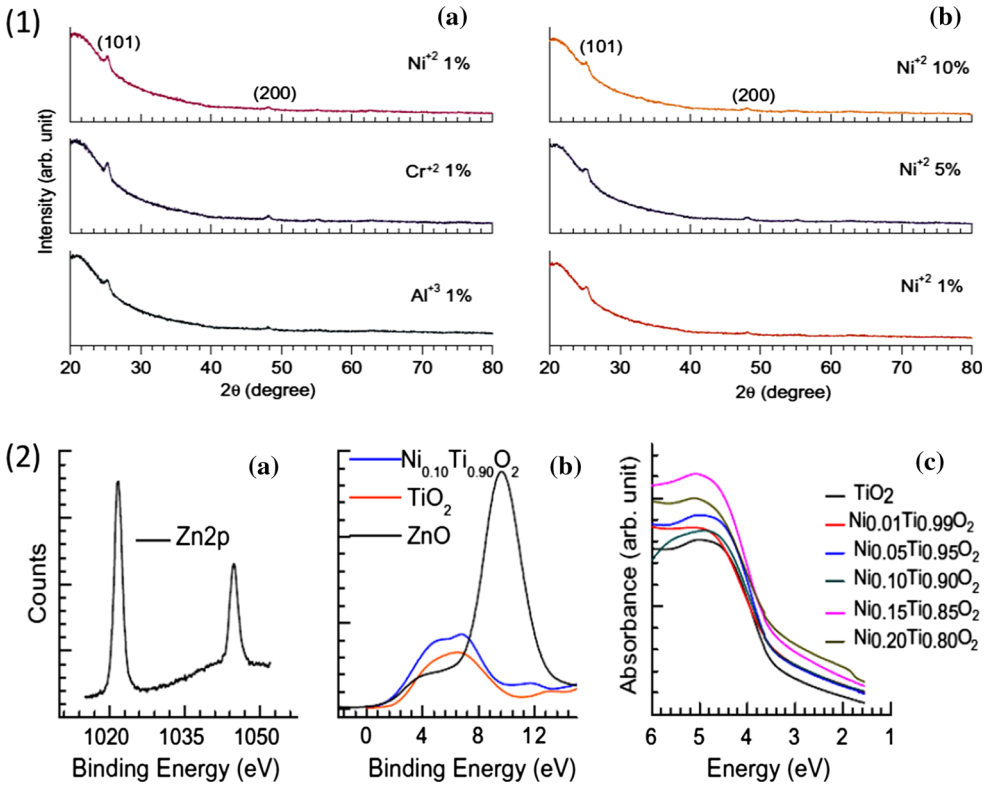

Fig. 25 1 The XRD patterns for typical lattice planes of (101), (200), (211), and (204) belonging to anatase phase of TiO_2 are shown for (a) $Al_xTi_{1-x}O_2$, $Cr_xTi_{1-x}O_2$, and $Ni_xTi_{1-x}O_2$ ($x = 0.01$) samples, and (b) for $Ni_xTi_{1-x}O_2$ ($x = 0.01$, 0.05, 0.1) samples. **2**(a) the core level Zn2p peaks, (b) and the VB spectra of ZnO, TiO_2, and $Ni_{0.10}Ti_{0.90}O_2$, (c) the optical absorption spectra of $Ni_xTi_{1-x}O_2$ ($x = 0$, 0.01,0.05,0.1,0.15,0.2) thin films with optical bandgap calculated in the range of 3.68–3.79 eV with increasing x. Reproduced from [71] with permission from © 2012 Elsevier B.V.

TiO_2 and $AgNO_3$ with optimum molar ratios are promising for industrial applications to eliminate organic pollutants from wastewater due to their large surface area, high surface-to-volume ratios, superior photocatalytic activity, and unique, stable, three-dimensional structures. The morphology and microstructural details of the as-prepared Ag_2O/TiO_2 *p–n* heterostructures were studied by FESEM and HRTEM observation, as shown in Fig. 27. Figures 27a, b show Ag_2O nanoparticles with size of 5–20 nm, which are tightly coupled on the TiO_2 nanorod surface within the microspheres. The formation of heterostructure was confirmed by transmission electron microscopy (TEM) images.

Figure 27b shows the TEM images of the TiO_2/Ag_2O nanostructure. The high-resolution TEM images of the region marked by a red square are displayed in Fig. 27c, d, which show the simultaneous presence of crystalline TiO_2 and Ag_2O. The interplanar spacing of 0.266 nm corresponds to the (100) plane of Ag_2O, while 0.249 nm corresponds to the (101) plane of rutile TiO_2. A continuity of lattice fringes between the interface of TiO_2 and Ag_2O is shown in Fig. 27(d), which indicates the formation of a *p–n* nano-heterojunction. Based on FESEM and HRTEM analysis, an atomic model of this heterostructure is illustrated in Fig. 27e, where red and white balls correspond to O and Ti atoms and yellow balls correspond to Ag atoms.

Dye-sensitized solar cells

DSSCs were proposed by O'Regan and Grätzel [285] and received much attention as an attractive alternative to semiconductor photovoltaic devices because of their

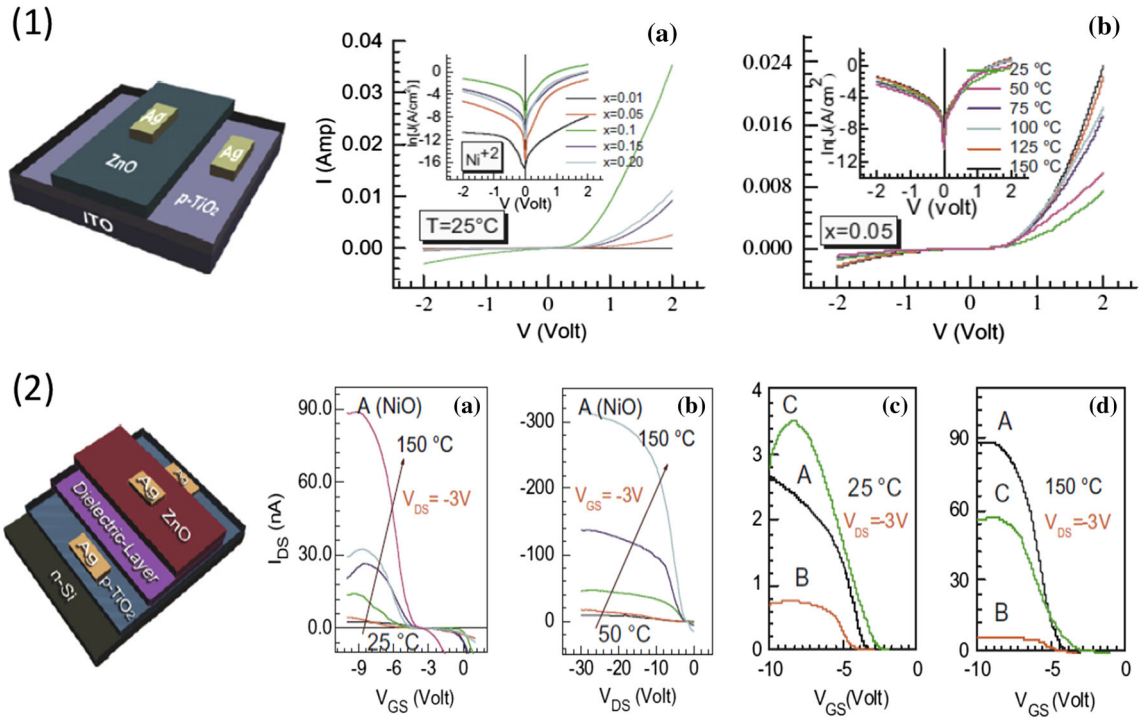

Fig. 26 **1** The schematic diagram of *n*-ZnO/*p*-TiO_2 is shown in the *left*. The current–voltage response of the assembly (a) at room temperature for different doping concentrations, (b) the temperature-dependent responses of the assembly. **2** The schematic representation for band alignment of *n*-ZnO/anatase *p*-TiO_2 heterojunction. **2** Schematic representation of the FET structure with NiO (labeled A), Al_2O_3 (labeled B), and $Ba_{0.5}Sr_{0.5}TiO_3$ (labeled C) as dielectric layers (*left*). Temperature-dependent (25–150 °C) variation of (a) drain current (I_{DS}) versus gate voltage (V_{GS}) plots at fixed drain-source voltages ($V_{DS} = -3$ V) and (b) $I_{DS} \sim$ gate voltage (V_{DS}) plots at fixed gate voltages ($V_{GS} = -3$ V) are shown for FET devices with NiO as dielectrics (labeled A). (c), (d) show a comparative study of temperature-dependent $I_{DS} \sim V_{GS}$ at fixed drain-source voltages ($V_{DS} = -3$ V) for the FET devices with NiO (A), $Ba_{0.5}Sr_{0.5}TiO_3$ (B) and Al_2O_3 (C) as dielectric layers. Reproduced from [283] with permission from © 2012 Elsevier B.V.

Table 6 Details of the temperature-dependent mobility and diffusion parameters of ZnO/dielectric constant/Ni^{2+}:TiO_2/*n*-Si assembly with $V_{GS} = \sim 3$ V

T [K (°C)]	μ_{sat} (cm^2/Vs)			D_h (cm^2/s)		
	NiO (A)	BSTO (B)	Al_2O_3 (C)	NiO (A)	BSTO (B)	Al_2O_3 (C)
323 (50)	0.386	0.149	0.342	0.01077	0.00415	0.0095
348 (75)	0.531	0.147	0.458	0.01595	0.00441	0.0137
373 (100)	0.715	0.144	0.647	0.02303	0.00463	0.0272
398 (125)	1.153	0.136	0.833	0.03958	0.00467	0.0285
423 (150)	2.914	0.154	1.265	0.10631	0.00562	0.0461

Reproduced from [283] with permission from © 2012 Elsevier B.V.

projected low manufacturing cost [286–288]. A typical DSSC consists of a nanostructured oxide layer (usually TiO_2) deposited on a glass substrate covered with TSO (typically FTO) acting as an anode (Fig. 28). The TiO_2 layer is sensitized with a monolayer of light-absorbing dye. A counter electrode is made of metal (Pt) or TSO coated with a catalyst. A redox-active electrolyte is placed between the electrodes. Sunlight passes through the transparent electrode and is absorbed in the dye layer. Electrons then transfer from the excited states of the dye into the TiO_2 CB. The electrons move to the anode by diffusion through TiO_2 nanoparticles, and after passing through the external circuit, they are re-introduced into the electrolyte from the cathode. The oxidized dye restores its original state by accepting electrons from the electrolyte.

Electron transport occurs in DSSCs due to the difference in the lowest unoccupied molecular orbital (LUMO) between the Fermi-level energy of oxides and the LUMO-energy of the dye material [289, 290], as shown in Fig. 28. The difference between the Fermi level of the oxide and the redox potential of the electrolyte determines the voltage generated by the cell under illumination [291, 292]. A cross

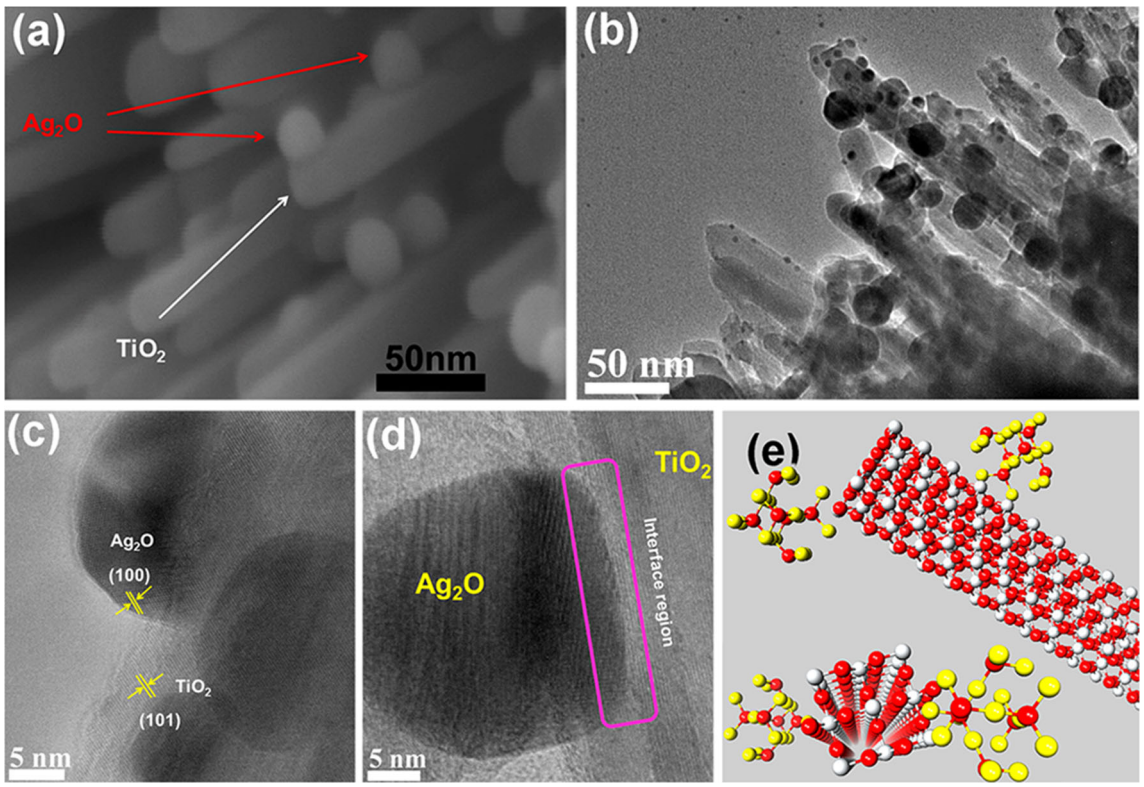

Fig. 27 **a** High-magnification FESEM image of heterojunction; **b–d** TEM and HRTEM images of the TiO_2/Ag_2O heterojunction. **e** Schematic atomic model. Reproduced from [284] with permission from © 2012 American Chemical Society

section of the DSSC geometry with transparent TiO_2 nanotube arrays on FTO-coated glass is illustrated in Fig. 29. 400-nm-thick titanium films were sputter-deposited on fluorine-doped tin-oxide (FTO)-coated glass and anodized at a constant potential of 10 V in an electrolyte of 0.5 % HF + acetic acid mixed in a 7:1 volume ratio [293]. The electrolyte contained 0.5 M LiI, 0.05 M I_2, 0.6 M *N*-methylbenzimidazole, 0.10 M guanidinium thiocyanate, and 0.5 M *tert*-butylpyridine in methoxypropionitrile (MPN). A conductive glass slide sputter-coated with 25 nm of Pt was used at the counter electrode. Electrolyte was introduced into the clamped electrodes by capillary action. The photocurrent (I) and photovoltage (V) of the resulting solar cells were measured for sizes ranging from 0.2 to 0.8 cm^2.

The AM-1.5 (150 W Oriel Solar Simulator) I–V characteristics of an illustrative 0.25 cm^2 device are shown in Fig. 30. At 100 % sun light, the DSSCs with a 3600-nm-thick nanotube array have a short circuit current density (J_{sc}) of 10.3 mA/cm^2, open-circuit voltage (V_{oc}) of 0.84 V, fill factor (ff) of 0.54, and overall conversion efficiency of 4.7 %. It is possible to fabricate highly efficient dye solar cells by increasing the length of the nanotube array on the negative electrode, and the amount of the absorbed dye

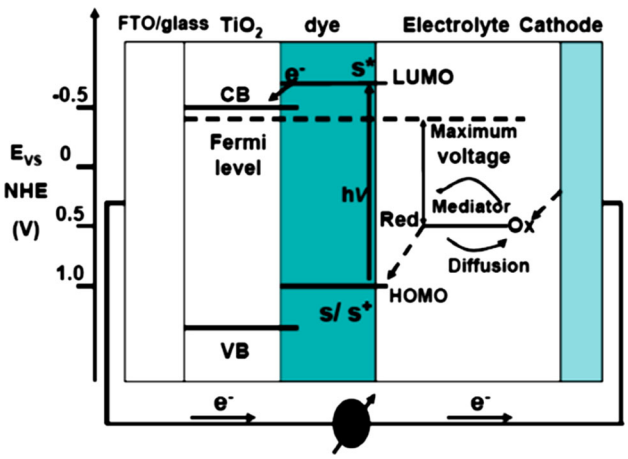

Fig. 28 Principle of operation and energy-level scheme of the dye-sensitized nanocrystalline solar cell. Photo-excitation of the sensitizer (S) is followed by electron injection into the conduction band of the mesoporous oxide semiconductor. The dye molecule is regenerated by the redox system, which itself is regenerated at the counter electrode by electrons passed through the load. Potentials are referred to the normal hydrogen electrode (NHE). The open-circuit voltage of the solar cell corresponds to the difference between the redox potential of the mediator and the Fermi level of the nanocrystalline oxide (TiO_2). Reproduced from [286] with permission from © 2010 Elsevier Ltd.

appears to be the limiting factor [294, 295]. A second key factor that impacts photoconversion efficiency is uniform dye absorption within the pores of the nanotube arrays. The nanotube array geometry has only one entrance or exit, which makes the prospect of pore filling by a liquid more challenging since air may be trapped inside.

Kim et al. [266] reported the preparation of transparent oriented titania nanotube (TNT) photo-electrodes and the effect of illumination direction on light harvesting, electron transport, and recombination in DSSCs. 10 at.% Nb-doped TiO_2 (NTO) thin layers were deposited on fluorine-doped SnO_2 conducting glass substrates (TCO, Pilkington TEC15) by RF-magnetron sputtering using a Nb-doped TiO_2 target at 400 °C under Ar flow (20 sccm) with a working pressure of 5 mTorr. Titanium films were deposited on top of the NTO layer by RF-magnetron sputtering using a Ti target (99.9 %) under the same sputtering conditions used for the NTO deposition. The thickness of the Ti films was about 5 μm. The aligned TNTs were produced by electrochemically anodizing the Ti films at 50 V (ramping rate; 1 V/s) in a mixture of 0.25 wt% NH_4F (99.9 %) and ethylene glycol (99 %) using a Pt counter electrode [296]. After prolonged anodization, the NTO layer was still strongly bonded to the TNT array and the TCO substrate, resulting in transparent TNT arrays without residual Ti. The solar conversion efficiency of the cell was about 2 times higher for collector-side illumination than for the counter electrode side. The higher conversion efficiency was mainly due to a larger photocurrent density associated with the higher light-harvesting efficiency of the cell.

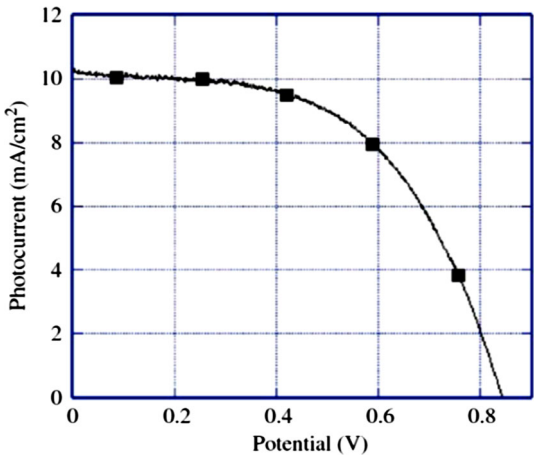

Fig. 30 Photocurrent–photovoltage characteristics of TiO_2-based transparent nanotube array DSSC using N719 dye under AM 1.5 illumination. Reproduced from [293] with permission from © 2006 Elsevier B.V.

Lee et al. [297] fabricated a transparent TiO_2 nanotube electrode by evaporating 5-μm-thick metallic Ti layers on FTO glass. The metal layers were completely anodized to form aligned nanotube layers. They compared the different conductivities and transparencies of FTO glass, which was used for the working electrodes and transparent platinized counter electrodes. Different types of FTO substrates (TCO22-7 (7 Ω/□) and TCO22-15 (15 Ω/□), Solaronix) were coated with 5-μm-thick Ti layers using electron beam evaporation with a deposition rate of 0.6 nm/min at 5×10^{-7} to 2×10^{-6} mbar. The resulting light conversion

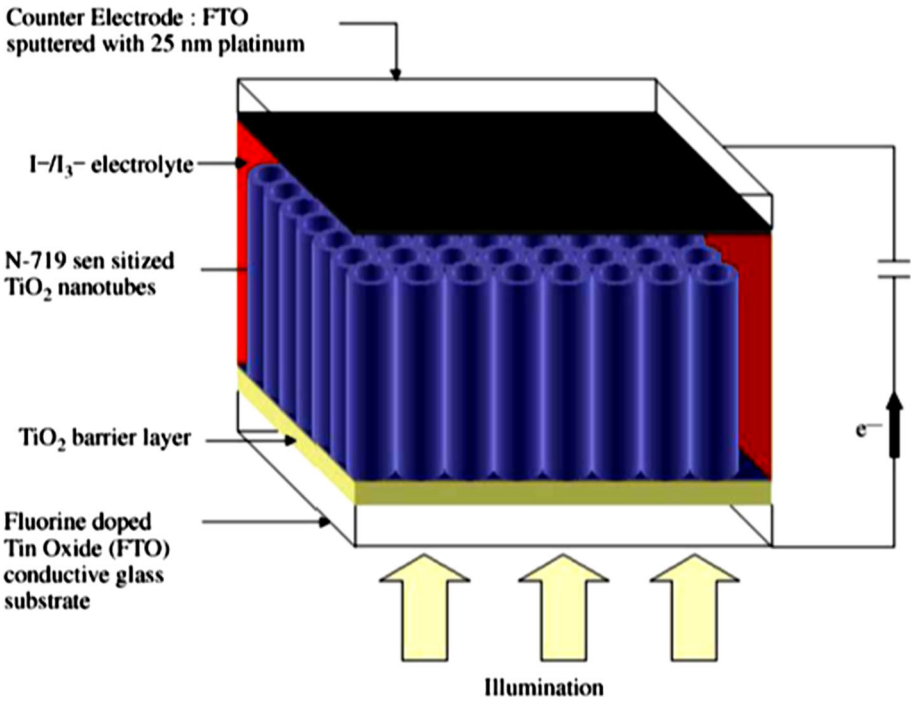

Fig. 29 Integration of transparent nanotube array architecture into front-side illuminated dye solar cell structure. Reproduced from [293] with permission from © 2006 Elsevier B.V.

efficiency of the TiO_2 nanotube electrodes in DSSCs was highly affected by the type of glass used. The results show that with increasing conductivity of the working electrode, the photoconversion efficiency is significantly increased. However, the conductivity of the counter electrode substrate is not a major influence. Additionally, in TiO_2 nanotube-based solar cells, lower resistance of the electrode is more important than losses of the light absorption in the working electrode if a more conductive glass is used. The efficiency range was 4.62–7.58 %, depending on the configuration of the electrodes.

Electrochromic display

Electrochromic display devices (ECD) are non-emissive, similar to a liquid crystal display (LCD). These materials show reversible optical absorption in the visible range when switched electrochemically [298–308]. One common characteristic of electrochromic materials is that they are wide-bandgap semiconductors with a lattice structure that allows easy field-aided proton or Li^+ ion intercalation [309–315]. In the case of TiO_2, the insertion process is accompanied by a reduction process: $TiO_2 + Y^+ + -ne^- = YTiO_2$ (Y^+ is the charged ion (e.g. H^+ or Li^+), e^- is an electron, and n is a number). This forms Ti^{3+} species and leads to a color change of the material [223, 316–319].

To fabricate a device that is transparent in the unbiased state, the active oxide layer is usually put on a conductive glass, and another conductive electrode is mounted on top. The space between the electrodes is filled with an electrolyte that contains the ions to be inserted. The kinetics and magnitude of proton or lithium ion insertion and the reversibility of the electrochromic reaction (contrast) are controlled by the solid-state diffusion and migration of the incorporated species. To shorten the solid-state diffusion path, many efforts have been made to operate these devices with nanoparticulate systems prepared from compacted TiO_2 nanoparticles [320–324], such as commercially available Degussa P25 sintered into a porous layer on conductive glass. However, TiO_2 nanotubes provide a valuable alternative.

A key advantage of nanotubes is the controllability of the surface area and morphology in an extremely wide range, as the aspect ratio of the nanotubes can be as high as 1700 [325]. Moreover, the as-prepared nanotubular layers are amorphous but can be easily transformed to anatase or a mixture of anatase and rutile by thermal treatment. The electronic structure can be significantly changed and influence the switchability properties. Over the past few years, TiO_2 nanotube layers have demonstrated very high electrochromic contrast [321], high switching speed, and tube layers that are more stable against cycling deterioration than layers made from particles. The devices are fabricated by lifting off the TiO_2 nanotube layers and transferring them to conducting glass (Fig. 31), or entire sputtered Ti layers can be successfully converted to a TiO_2 nanotube layer.

Other energy-related applications

Other applications of transparent titania are hydrogen sensing, photoelectrochemical, and water photolysis devices [325–328]. The demand for a highly sensitive, selective, and stable hydrogen sensor has increased in recent years mainly due to the continued and growing importance of hydrogen in fuel cell applications [329], as well as the chemical, semiconductor, food processing, and petroleum industries. Various types of sensor technologies are being developed [330], such as Schottky junctions [331–334], fiber optics [335–339], catalysis [338–340], electrochemical techniques [341–344], field-effect transistors (FETs) [345–347], oxide semiconductors [72, 325, 348–352], and combinations of these. Gasochromic TiO_2 devices have been gaining importance in recent years due to a large number of applications, such as gas sensing, smart windows, and display industries [353, 354]. Gasochromic device structures are much simpler than electrochromic devices, and they are of great value in large-area applications. Domaradzki et al. [355] studied the gasochromic effect in TiO_2 thin films doped with palladium and tantalum. Gasochromic change in the properties of TiO_2:(Pd, Ta) was induced by reaction of ethanol thermal decomposition products with a thin film surface and caused by adsorption of decomposition products on the surface.

Grimes et al. [293] have shown manifold increase in electrical conductivity of the TiO_2 nanotube layer upon exposure to H_2 environments. For example, a response on

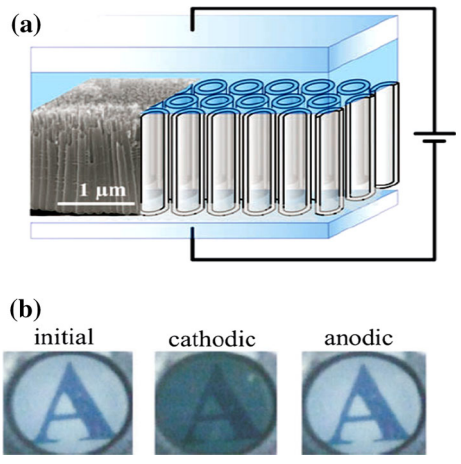

Fig. 31 Schematic view (**a**) and photographs (**b**) from an electrochromic switching window based on oriented TiO_2 nanotubes. Reproduced from [324] with permission from © 2009 The Royal Society of chemistry

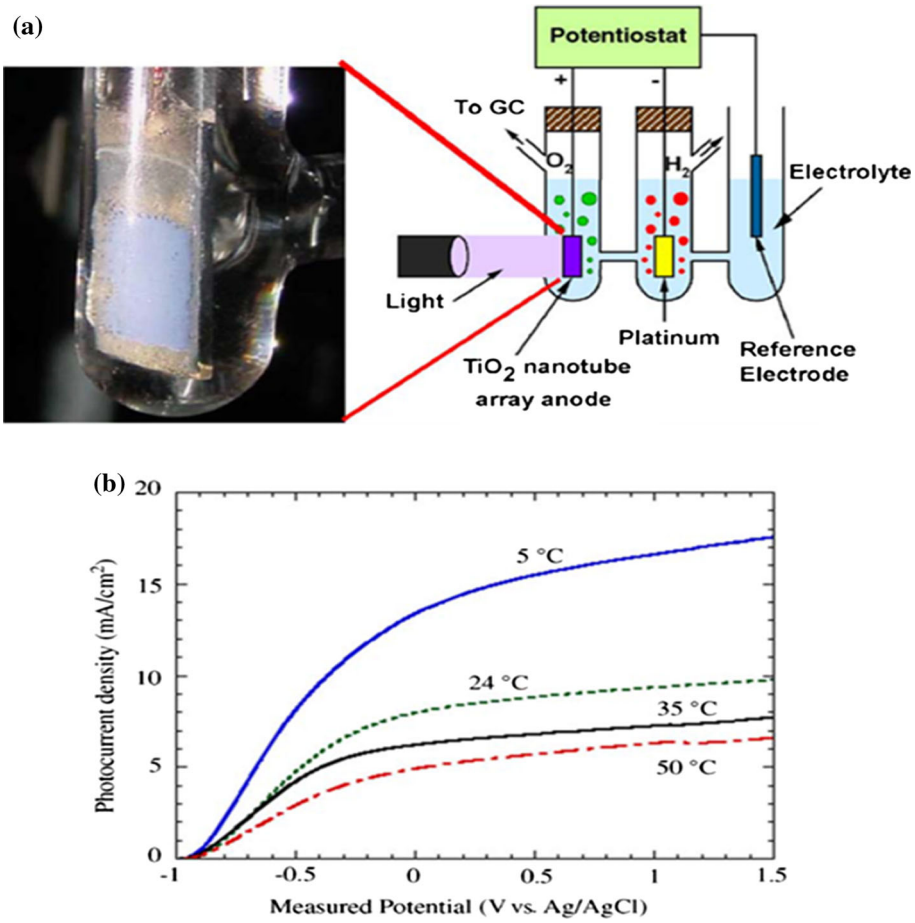

Fig. 32 **a** Illustrative drawing of experimental setup for hydrogen generation by water photoelectrolysis, **b** Variation of photocurrent density (in 1 M KOH solution) versus measured potential versus Ag/AgCl for 10 V samples anodized at four anodization bath temperatures of 5, 25, 35, and 50 °C. The samples were measured under 320–400-nm illumination at 100 mW/cm^2. Reproduced from [293] with permission from © 2006 Elsevier B.V.

the order of several magnitudes has been determined for 1000 ppm H_2 containing nitrogen atmospheres. Figure 32a illustrates an experimental setup for water photoelectrolysis measurements with the nanotube arrays used as the photoanodes from which oxygen is evolved. Figure 32b shows the *I–V* characteristics of the titania nanotube array electrodes (the photocurrent density vs. potential) measured in 1 M KOH electrolyte as a function of the anodization bath temperature under UV illumination (320–400 nm, 100 mW/cm^2). The samples were fabricated using HF electrolyte.

At 1.5 V, the photocurrent density of the sample anodized at 5 °C is more than three times that for the sample anodized at 50 °C. The lower anodization temperature also increases the slope of the photocurrent–potential characteristic curve. For a sample anodized at 10 V and 5 °C, the photoresponse to monochromatic illumination at 337 nm and 2.7 mW/cm^2 showed high anodic polarization greater than 1 V and quantum efficiency greater than 90 %. The photoconversion efficiency for converting light energy to chemical energy in the presence of an external applied potential was calculated using the following expression:

$$\%\,\eta = [(\text{Total power output} - \text{electrical power output}) / \text{light power}] \times 100 \tag{18}$$

$$\%\,\eta = j_p[(E^0_{rev} - |E_{app}|)/I_0 \times 100, \tag{19}$$

where $E_{app} = E_{meas} - E_{aoc}$, the total power output is j_p-E^0_{rev}, the electrical power input is $j_p|E_{app}|$, and j_p is the photocurrent density in mA/cm^2. E^0_{rev} is the standard reversible potential of 1.23 V/NHE. E_{meas} is the electrode potential (vs. Ag/AgCl) of the working electrode at which photocurrent was measured under light illumination. E_{aoc} is the electrode potential (vs. Ag/AgCl) of the same working electrode in open-circuit conditions under the same illumination and in the same electrolyte solution. I_0 is the intensity of incident light in mW/cm^2.

Future developments

There are several interesting future aspects of TiO_2 that make it an important candidate for TSO-related applications. Firstly, cost-effective yet highly efficient synthesis

strategies for both undoped and doped TiO_2 thin films and nanomaterials have to be investigated for superior device applications and volume production. If the fabrication method is compatible with CMOS-IC techniques, it can easily be integrated with silicon electronics for diverse industrial applications. Secondly, new doping strategies with newer dopants have to be examined for bandgap engineering of TiO_2–TSOs for improved electrical properties without compromising the visible transparency, which is extremely important for TSO-related applications. Thirdly, and most importantly, syntheses of p-type semiconducting transparent TiO_2 thin films and nanomaterials have to be explored for highly important transparent homojunction fabrication (in the form of *n*-TiO_2/*p*-TiO_2) for emerging transparent electronics applications.

New dopants can be investigated in this regard to have high p-type conductivity comparable to the corresponding n-type counterparts. This may give added impetus to the field of "invisible electronics" [69]. Furthermore, careful band-gap engineering of TiO_2–TSO by meticulous selection of a proper dopant for infrared (IR) transmittance would improve the efficiency of solar cells and OLEDs. Hence, there is tremendous scope for pursuing research on the potential applications of *p*-TiO_2 as an active element in electronic and photovoltaic devices.

Conclusions

TiO_2 is a class of material that simultaneously has high visible transparency and significant electrical conductivity. Most of the TiO_2-based applications involve photocatalytic activities for environmental remediation, along with antibacterial activity and superhydrophilicity, but its applications as TSOs in the field of transparent electronics are limited. Since emerging applications in the field require new materials and improved syntheses strategies for high efficient devices, a detailed review of the synthesis and applications of this technologically important material as a transparent semiconducting oxide warrants considerable attention.

A comprehensive review of the latest developments in the synthesis, properties, modification, and application of TiO_2-based TSOs has been presented. Synthesis strategies of both chemical and physical techniques to fabricate TiO_2–TSOs with relatively good opto-electrical properties have been discussed. Modification of the band structure by doping and the use of non-stoichiometry have been presented in detail. With better understanding of the defect chemistry and the role of dopants to increase the conductivity of these materials, newer and higher-quality TiO_2–TSOs can be developed for diverse device applications.

Generally, TiO_2 is an intrinsically n-type semiconductor, and the electron conductivity can be increased by doping with pentavalent cations (Nb, Ta, etc.). But most importantly, it can be doped into a p-type TSO with di-valent or tri-valent cations (Cr, Fe, Ni, Co, etc.). The p-type TSOs are extremely important in the field of emerging transparent electronics for the potential fabrication of invisible circuits [69] for UV-based solar cells [351, 352]. Hence, considerable attention was given to the syntheses and doping strategies to fabricate p-type TiO_2 as TSOs. Also, the applications of both n- and p-type TiO_2–TSOs in relation to transparent junctions for thin film transparent electrodes, DSSC, electrochromic displays, and other energy-related applications have been reviewed.

TiO_2–TSOs are now a vital part of modern light-emitting and photovoltaic devices and FPDs owing to high conductivity and high transmittance. The coexistence of electrical conductivity and optical transparency in TiO_2–TSO-based devices depends on the nature, number, and atomic arrangements of metal cations in the crystalline or amorphous oxide structures, the resident morphology, and the presence of intrinsic or intentionally introduced defects. This review may provide important insights to improve the electro-optical properties of TiO_2 for applications in transparent electronics and other fields related to TSO and energy.

Acknowledgements This work is funded by the Grant NRF-2015-002423 of the National Research Foundation of Korea.

References

1. Cava RJ, Phillips JM, Kwo J, Thomas GA, van Dover RB, Carter SA, Krajewski JJ, Peck WF Jr, Marshall JH, Rapkine DH (1994) $GaInO_3$: a new transparent conducting oxide. Appl Phys Lett 64:2071–2072
2. Phillips JM, Cava RJ, Thomas GA, Carter SA, Kwo J, Siegrist T, Krajewski JJ, Marshall JH, Peck WF Jr, Rapkine DH (1995) A highly-conducting transparent conductor: zinc indium tin oxide. Appl Phys Lett 67:2246–2248
3. Badeker K (1907) Über die elektrische Leitfähigkeit und die thermoelektrische Kraft einiger Schwermetallverbindungen. Ann Phys (Leipz) 22:749–766
4. Brabec CJ, Sariciftci NS, Hummelen JC (2001) Plastic solar cells. Adv Funct Mater 11:15–26
5. Peumans P, Yakimov A, Forrest SR (2003) Small molecular weight organic thin-film photo detectors and solar cells. J Appl Phys 93:3693–3723
6. Yu G, Gao J, Hummelen JC, Wudl F, Heeger AJ (1995) Polymer photovoltaic cells: enhanced efficiencies via a network of internal donor-acceptor heterojunctions. Science 270:1789–1936
7. Ihara T, Miyoshi M, Ando M, Sugihara S, Iriyama Y (2001) Preparation of a visible-light-active TiO_2 photocatalyst by RF plasma treatment. J Mater Sci 36:4201–4207. doi:10.1023/A:1017929207882
8. Bhosle V, Prater JT, Yang F, Burk D, Forrest SR, Narayan J (2007) Gallium-doped zinc oxide films as transparent electrodes

for organic solar cell applications. J Appl Phys 102:0235 01–023505
9. Fortunato E, Ginley D, Hosono H, Paine DC (2007) Transparent conducting oxides for photovoltaics. MRS Bull 32:242–247
10. Fortunato E, Raniero L, Silva L, Gonçalves A, Pimentel A, Barquinha P, Guas HA, Pereira L, Gonçalves G, Ferreira I, Elangovan E, Martins R (2008) Highly stable transparent and conducting gallium-doped zinc oxide thin films for photovoltaic applications. Sol Energy Mater Sol Cells 92:1605–1610
11. Hartnagel HL, Dawar AL, Jain AK, Jagadish C (1995) Semiconducting transparent thin films. Institute of Physics, Bristol
12. Pan CA, Ma TP (1980) High quality transparent conductive indium oxide films prepared by thermal evaporation. Appl Phys Lett 37:163–165
13. Hamberg I, Granqvist CG (1986) Evaporated Sn-doped In_2O_3 films: basic optical properties and applications to energy-efficient windows. J Appl Phys 60:R123–R160
14. Calnan S, Tiwari AN (2010) High mobility transparent conducting oxides for thin film solar cells. Thin Solid Films 518:1839–1849
15. Minami T (2000) New n-type transparent conducting oxides. Mater Res Bull 25:38–44
16. Pimputkar S, Speck JS, DenBaars SP, Nakamura S (2009) Prospects for LED lighting. Nat Photonics 3:180–182
17. Lim JH, Hwang DK, Kim HS, Oh JY, Yang JH, Navamathavan R, Park SJ (2004) Low-resistivity and transparent indium-oxide-doped ZnO ohmic contact to p-type GaN. Appl Phys Lett 85:6191–6193
18. Gordon RG (2000) Criteria for choosing transparent conductors. MRS Bull 25:52–57
19. Banerjee AN, Joo SW, Min BK (2014) Nanocrystalline ZnO film deposition on flexible substrate by low-temperature sputtering process for plastic displays. J Nanosci Nanotechnol 14:7970–7975
20. Banerjee AN, Ghosh CK, Chattopadhyay KK, Minoura H, Sarkar AK, Akiba A, Kamiya A, Endo T (2006) Low-temperature deposition of ZnO thin films on PET and glass substrates by DC-sputtering technique. Thin Solid Films 496:112–116
21. Banerjee AN, Maity R, Kundoo S, Chattopadhyay KK (2004) Poole–Frenkel effect in nanocrystalline SnO_2: F thin films prepared by sol–gel-dip-coating technique. Phys Status Solid A 201:983–989
22. Banerjee AN, Kundoo S, Saha P, Chattopadhyay KK (2003) Synthesis and characterization of nano-crystalline fluorine-doped tin oxide thin films by sol–gel method. J Sol Gel Sci Technol 28:105–110
23. Maity R, Banerjee AN, Chattopadhyay K (2004) Low-macroscopic field emission from fibrous ZnO thin film prepared by catalyst-free solution route. Appl Surf Sci 236:231
24. Banerjee AN, Chattopadhyay KK (2004) Low-threshold field-emission from transparent p-type $CuAlO_2$ thin film prepared by dc sputtering. Appl Surf Sci 225:243
25. Banerjee AN, Ghosh CK, Das S, Chattopadhyay KK (2005) Electro-optical characteristics and field-emission properties of reactive DC sputtered p-$CuAlO_{2+x}$ thin films. Phys B 370:264–276
26. Norton DP (2004) Synthesis and properties of epitaxial electronic oxide thin-film materials. Mater. Sci. Eng R 43:139–247
27. Major S, Banerjee A, Chopra KL (1984) Annealing studies of undoped and indium-doped zinc oxide. Thin Solid Films 122:31–43
28. Minami T, Nanto H, Takata S (1984) Highly conductive and transparent aluminium doped zinc oxide thin films prepared by RF magnetron sputtering. Jpn J Appl Phys 23:L280–L282
29. Hu J, Gordon RG (1991) Textured fluorine doped ZnO films by atmospheric pressure chemical vapor deposition and their use in amorphous silicon solar cells. Sol Cells 30:437–450
30. Choi BH, Im HB, Song JS, Yoon KH (1990) Optical and electrical properties of Ga_2O_3-doped ZnO films by r.f. sputtering. Thin Solid Films 193:712–720
31. Avaritsiotis N, Howson RP (1981) Composition and conductivity of fluorine-doped conducting indium oxide films prepared by reactive ion plating. Thin Solid Films 77:351–357
32. Haacke G, Mealmaker WE, Siegel LA (1978) Sputter deposition and characterization of Cd_2SnO_4 films. Thin Solid Films 55:67–81
33. Otabe T, Ueda K, Kudoh A, Hosono H, Kawazoe H (1998) n-type electrical conduction in transparent thin films of delafossite-type $AgInO_2$. Appl Phys Lett 72:1036–1038
34. Dali SE, Sai Sunder VVSS, Jayachandran M, Chockalingam MJ (1998) Synthesis and characterization of Aln_2O_4 indates, A = Mg, Ca, Sr, Ba. J Mater Sci Lett 17:619–623
35. Edwards DD, Mason TO, Goutenoire F, Poeppelmeier KR (1997) A new transparent conducting oxide in the Ga_2O_3–In_2O_3–SnO_2 system. Appl Phys Lett 70:1706–1708
36. Minami T, Takata S, Kakumu T, Sonohara H (1995) New transparent conducting $MgIn_2O_4$ $Zn_2In_2O_5$ thin films prepared by magnetron sputtering. Thin Solid Films 270:22–26
37. Minami T, Kakumu T, Shimokawa K, Takata S (1998) New transparent conducting ZnO–In_2O_3–SnO_2 thin films prepared by magnetron sputtering. Thin Solid Films 317:318–321
38. Omata T, Ueda N, Ueda K, Kawazoe H (1994) New ultraviolet-transport electroconductive oxide, $ZnGa_2O_4$ spinel. Appl Phys Lett 64:1077–1078
39. Kammler DR, Mason TO, Young DL, Coutts TJ, Ko D, Poeppelemier KR, Williamson DL (2001) Comparison of thin film and bulk forms of the transparent conducting oxide solution Cd_{1+x} In_{2-2x} Sn_xO_4. J Appl Phys 90:5980–5985
40. Lewis BG, Paine D (2000) Applications and processing of transparent conducting oxides. MRS Bull 25:22–27
41. Hitosugi T, Yamada N, Nakao S, Hirose Y, Hasegawa T (2010) Properties of TiO_2-based transparent conducting oxides. Phys Status Solid A 207:1529–1537
42. Kasai J, Hitosugi T, Moriyama M, Goshonoo K, Hoang NLH, Nakao S, Yamada N, Hasegawa T (2010) Properties of TiO_2-based transparent conducting oxide thin films on GaN(0001) surfaces. J Appl Phys 107:53110-1–53110-4
43. Gillespie MA (2007) Sputtered Nb-and Ta-doped TiO_2 transparent conducting oxide films on glass. J Mater Res 22:2832–2837
44. Hitosugi Furubayashi T, Yamamoto Y, Inaba K, Kinoda G, Hirose Y, Shimada T, Hasegawa T (2005) A transparent metal:Nb-doped anatase TiO_2. Appl Phys Lett 86:252101–252103
45. Hitosugi T, Furubayashi Y, Ueda A, Itabashi K, Inaba K, Hirose Y, Kinoda G, Yamamoto Y, Shimada T, Hasegawa T (2005) Ta-doped anatase TiO_2 epitaxial film as transparent conducting oxide. Jpn J Appl Phys 44:33–36
46. Yamada N, Hitosugi T, Kasai J, Hoang NLH, Nakao S, Hirose Y, Shimada T, Hasegawa T (2010) Transparent conducting Nb-doped anatase TiO_2 (TNO) thin films sputtered from various oxide targets. Thin Solid Films 518:3101–3104
47. Anitha VC, Deepthy M, Nair SV, Prasanth R (2010) Electrochemical tuning of titania nanotube morphology in inhibitor electrolytes. Electrochim Acta 55:3703–3713
48. Banerjee AN (2011) The design, fabrication, and photocatalytic utility of nanostructured semiconductors: focus on TiO_2-based nanostructures. Nanotechnol Sci Appl 4:35–65
49. Roy P, Berger S, Schmuki P (2011) TiO_2 nanotubes: synthesis and applications. Angew Chem Int Ed 50:2904–2939
50. Linsebigler AL, Lu G, Yates JT Jr (1995) Photocatalysis on TiO_2 surfaces: principles, mechanisms, and selected results. Chem Rev 95:735–758

51. Sirghi L, Hatanaka Y (2003) Hydrophilicity of amorphous TiO_2 ultra-thin films. Surf Sci 530:L323–L327
52. Kim HR, Lee TG, Shul YG (2007) Photoluminescence of La/Ti mixed oxides prepared using sol–gel process and their pCBA photodecomposition. J Photochem Photobiol A 185:156–160
53. Saif M, Abdel-Mottaleb MSA (2007) Titanium dioxide nanomaterial doped with trivalent lanthanide ions of Tb, Eu and Sm: preparation, characterization and potential applications. Inorg Chim Acta 360:2863–2874
54. Asghar MH, Shoaib M, Placido F, Naseem S (2009) Modeling and preparation of practical optical filters. Curr Appl Phys 9:1046–1053
55. Frindell KL, Bartl MH, Robinson MR, Bazan GC, Popitsch A, Stucky GD (2003) Visible and near IR luminescence via energy transfer in rare earth doped mesoporous titania thin films with nanocrystalline walls. J Solid State Chem 172:81–88
56. Thi Vu TH, Thi AuH, Tran LT, Nguyen TMT, Tran TTT, Pham MT, Do MH, Nguyen DL (2014) Synthesis of titanium dioxide nanotubes via one-step dynamic hydrothermal process. Mater Sci 49:5617–5625
57. Bumajdad A, Madkour M, Abdel-Moneam Y, El-Kemary M (2014) Nanostructured mesoporous Au/TiO_2 for photocatalytic degradation of a textile dye: the effect of size similarity of the deposited Au with that of TiO_2 pores. J Mater Sci 49:1743–1754. doi:10.1007/s10853-013-7861-0
58. Banerjee AN, Joo SW, Min BK (2012) Photocatalytic degradation of organic dye by sol–gel-derived gallium-doped anatase titanium oxide nanoparticles for environmental remediation. J Nanomater 2012:201492
59. Ni M, Leung MKH, Leung DYC, Sumathy K (2007) A review and recent developments in photocatalytic water-splitting using TiO_2 for hydrogen production. Renew Sustain Energy Rev 11:401–425
60. Thompson TL, Yates JT Jr (2006) Surface science studies of the photoactivation of TiO_2 new photochemical processes. Chem Rev 106:4428–4453
61. Diebold U (2003) Structure and properties of TiO_2 surfaces: a brief review. Appl Phys A 76:681–687
62. Girish Kumar S, Gomathi Devi L (2011) Review on modified TiO_2 photocatalysis under UV/visible light: selected results and related mechanisms on interfacial charge carrier transfer dynamics. J Phys Chem A 115:13211–13241
63. McCullagh C, Robertson JMC, Bahnemann DW, Robertson PKJ (2007) The application of TiO_2 photocatalysis for disinfection of water contaminated with pathogenic microorganisms: a review. Res Chem Intermed 33:359–375
64. Macwan DP, Dave Pragnesh N, Chaturvedi Shalini (2011) A review on nano-TiO_2 sol–gel type syntheses and its applications. J Mater Sci 46:3669–3686. doi:10.1007/s10853-011-5378-y
65. Gupta SM, Tripathi M (2011) A review of TiO_2 nanoparticles. Chin Sci Bull 56:1639–1657
66. Anitha VC, Lee J-H, Jintae L, Banerjee AN, Joo SW, Min B-K (2015) Biofilm formation on TiO_2 nanotube with controlled pore diameter and surface wettability. Nanotechnology 26:065102
67. Zeman P, Takabayashi S (2002) Self-cleaning and antifogging effects of TiO_2 films prepared by radio frequency magnetron sputtering. J Vac Sci Technol A 20:388
68. Zhao G, Tian Q, Liu Q, Han G (2005) Effect of HPC on the microstructure and hydrophilicity of sol–gel-derived TiO_2 films. Surf Coat Technol 198:55
69. Thomas G (1997) Invisible circuits. Nature 389:907–908
70. Nandy S, Banerjee AN, Fortunato E, Martins R (2013) A review on Cu_2O and Cu^I-based p-type semiconducting transparent oxide materials. Rev Adv Sci Eng 2:273–304
71. Banerjee AN, Chattopadhyay KK (2005) Recent developments in the emerging field of crystalline p-type transparent conducting oxide thin films. Prog Cryst Growth Charact Mater 50:52–105
72. Kawazoe H, Yanagi H, Ueda K, Hosono H (2000) Transparent p-type conducting oxides: design and fabrication of *p–n* heterojunctions. MRS Bull 25:28–36
73. Banerjee AN, Joo SW (2013) Poole–Frenkel effect in sputter-deposited $CuAlO_{2+x}$ nanocrystals. Nanotechnology 24:165705–165707
74. Facchetti A, Marks TJ (2010) Transparent electronics: from synthesis to applications. Wiley, West Sussex
75. Sato H, Minami T, Takata S, Yamada T (1993) Transparent conducting p-type NiO thin films prepared by magnetron sputtering. Thin Solid Films 236:27–31
76. Kawazoe H, Yasukawa M, Hyodo H, Kurita M, Yanagi H, Hosono H (1997) p-type electrical conduction in transparent thin films of $CuAlO_2$. Nature 389:939–942
77. Cao J, Zhang Y, Liu L, Ye J (2013) A p-type Cr-doped TiO_2 photo-electrode for photo-reduction. Chem Commun 49: 3440–3442
78. Zaleska A (2008) Doped-TiO_2: a review. Recent Pat Eng 2:157–164
79. Shankar K, Basham JI, Allam NK, Varghese OK, Mor GK, Feng X, Paulose M, Seabold JA, Choi K-S, Grimes CA (2009) Recent advances in the use of TiO_2 nanotube and nanowire arrays for oxidative photoelectrochemistry. J Phys Chem C 113: 6327–6359
80. Juodkazis K, Juodkazyte J, Jelmakas E, Kalinauskas P, Valsiunas I, Miecinskas P, Juodkazis S (2010) Photoelectrolysis of water: solar hydrogen–achievements and perspectives. Opt Express 18:A147–A160
81. Xiaobo C, Mao SS (2007) Titanium dioxide nanomaterials: synthesis, properties, modifications, and applications. Chem Rev 107:2891–2959
82. Wold A (1993) Photocatalytic properties of TiO_2. Chem Mater 5:280–283
83. Han W, Wang YD, Zheng YF (2008) In vitro biocompatibility study of nano TiO_2 materials. Adv Mater Res 47–50:1438–1441
84. Jones RO, Gunnarsson O (1989) The density functional formalism, Its applications and prospects. Rev Mod Phys 61:689
85. Onida G, Reining L, Rubio A (2002) Electronic excitations: density-functional versus many-body Green's-functions approaches. Rev Mod Phys 74:601
86. Gonze X, Amadon B, Anglade P-M, Beuken J-M, Bottin F, Boulanger P, Bruneval F, Caliste D, Caracas R, Cote M, Deutsch T, Genovese L, Ghosez Ph, Giantomassi M, Goedecker S, Hamann D, Hermet P, Jollet F, Jomard G, Oliveira MJT (2009) ABINIT: first-principles approach to material and nanosystem properties. Comput Phys Commun 180:2582–2615
87. Zhu T, Gao S-P (2014) The stability, electronic structure, and optical property of TiO_2 polymorphs. J Phys Chem C 118:11385–11396
88. Kang W, Hybertsen MS (2010) Quasiparticle and optical properties of rutile and anatase TiO_2. Phys Rev B 82:085203
89. Chiodo L, Garcia-Lastra JM, Iacomino A, Ossicini S, Zhao J, Petek H, Rubio A (2010) Self-energy and excitonic effects in the electronic and optical properties of TiO_2 crystalline phases. Phys Rev B 82:045207
90. Patrick CE, Giustino F (2012) GW quasiparticle bandgaps of anatase TiO_2 starting from DFT + U. J Phys Condens Matter 24:202201
91. Landmann M, Rauls E, Schmidt WG (2012) The electronic structure and optical response of rutile, anatase and brookite TiO_2. J Phys Condens Matter 24:195503
92. Thulin L, Guerra J (2008) Calculations of strain-modified anatase TiO_2 band structures. Phys Rev B 77:195112

93. Hitosugi T, Kamisaka H, Yamashita K, Nogawa H, Furubayashi Y, Nakao S, Yamada N, Chikamatsu A, Kumigashira H, Oshima M, Hirose Y, Shimada T, Hasegawa T (2008) Electronic band structure of transparent conductor: Nb-doped anatase TiO_2. Appl Phys Express 1:111203
94. Hirose Y, Yamada N, Nakao S, Hitosugi T, Shimada T, Hasegawa T (2009) Large electron mass anisotropy in a d-electron-based transparent conducting oxide: Nb-doped anatase TiO_2 epitaxial films. Phys Rev B 79:165108
95. Nogawa H, Chikamatsu A, Hirose Y, Nakao S, Kumigashira H, Oshima M, Hasegawa T (2011) Carrier compensation mechanism in heavily Nb-doped anatase $Ti_{1-x}Nb_xO_2 + \delta$ epitaxial thin films. J Phys D Appl Phys 44:365404
96. Modes T, Scheffel B, Chr Meetzner, Zywitzki O, Reinhold E (2005) Structure and properties of titanium oxide layers deposited by reactive plasma activated electron beam evaporation. Surf Coat Technol 200:306–309
97. Ho W, Yu JC, Lee S (2007) Photocatalytic activity and photo-induced hyrophilicity of mesoporous TiO_2 thin films coated on aluminium substrate. Appl Catal B Environ 73:135–143
98. Mathur S, Kuhn P (2006) CVD of titanium oxide coatings: comparative evaluation of thermal and plasma assisted processes. Surf Coat Technol 201:807–814
99. Frach P, Gloss D, Chr Metzner, Modes T, Scheffel B, Zywitzki O (2006) Deposition of photocatalytic TiO_2 layers by pulse magnetron sputtering and by plasma-activated evaporation. Vacuum 80:679–683
100. Amor SB, Guedri L, Baud G, Jacquet M, Ghedira M (2002) Influence of the temperature on the properties of sputtered titanium oxide films. Mater Chem Phys 77:903–911
101. Sato Y, Sanno Y, Tasaki C, Oka N (2010) Electrical and optical properties of Nb-doped TiO_2 films deposited by dc magnetron sputtering using slightly reduced Nb-doped TiO_{2-x} ceramic targets. J Vac Sci Technol A 28:4
102. Niu Z, Gaob F, Jia X, Zhang W, Chena W, Qian K (2006) Synthesis studies of sputtering TiO_2 films on poly(dimethylsiloxane) for surface modification. Colloids Surf A Physicochem Eng Asp 272:170–175
103. Sicha J, Herman D, Musil J, Stryhal Z, Pavlik J (2007) High-rate low-temperature dc pulsed magnetron sputtering of photocatalytic TiO_2 films: the effect of repetition frequency. Nanoscale Res Lett 2:123–129
104. Musil J, Herman D, Sicha J (2006) Low-temperature sputtering of crystalline TiO_2 films. J Vac Sci Technol A 24:521
105. Herman D, Musil J, Sicha J (2006) Photoactivated properties of TiO_2 films prepared by magnetron sputtering. In: Proceedings of the PSE 2006 in plasma processes & polymers
106. Hitosugi T, Ueda A, Nakao S, Yamada N, Furubayashi Y, Hirose Y, Shimada T, Hasegawa T (2007) Fabrication of highly conductive $Ti_{1-x}Nb_xO_2$ polycrystalline films on glass substrates via crystallization of amorphous phase grown by pulsed laser deposition. Appl Phys Lett 90:212106
107. Yamada N, Hitosugi T, Hoang NLH, Furubayashi Y, Hirose Y, Shimada T, Hasegawa T (2007) Fabrication of low resistivity Nb-doped TiO_2 transparent conductive polycrystalline films on glass by reactive sputtering. Jpn J Appl Phys 46:5275
108. Maghanga CM, Niklasson GA, Granqvist CG (2009) Optical modelling of spectrally selective reflectors based on TiO_2: Nb transparent conducting oxide films for silicon solar cell applications. Proc SPIE 7407:74070F-3
109. Smith DY, Shiles E, Inokuti M (1985) The optical properties of metallic aluminum. In: Palik ED (ed) Handbook of optical constants of solids. Academic, San Diego, pp 369–406
110. Eriksson TS, Hjortsberg A, Niklasson GA, Granqvist CG (1981) Infrared optical properties of evaporated alumina films. Appl Opt 20:2742–2746
111. Kasai J, Hitosugi T, Moriyama M, Goshonoo K, Hoang NLH, Nakao S, Yamada N, Hasegawa T (2010) Properties of TiO_2-based transparent conducting oxide thin films on GaN(0001) surfaces. J Appl Phys 107:053110
112. Hitosugi T, Hirose Y, Kasai J, Furubayashi Y, Ohtani M, Inaba K, Nakajima K, Chikyow T, Shimada T, Hasegawa T (2005) Heteroepitaxial growth of rutile TiO_2 on GaN(0001) by pulsed laser deposition. Jpn J Appl Phys 44:L1503–L1505
113. Hoang NLH, Yamada N, Hitosugi T, Kasai J, Nakao S, Shimada T, Hasegawa T (2008) Low-temperature fabrication of transparent conducting anatase Nb-doped TiO_2 films by sputtering. Appl Phys Express 1:115001
114. Wu B-B, Pan F-M, Yang Y-E (2011) Annealing effect of pulsed laser deposited transparent conductive Ta-doped titanium oxide films. Chin Phys Lett 28(11):118102
115. Hsu LS, Lucaa D (2003) Substrate and annealing effects on the pulsed-laser deposited TiO_2 thin films. J Optoelectron Adv Mater 5:841–847
116. Tonooka K, Chiu Te-Wei, Kikuchi N (2009) Preparation of transparent conductive TiO2: Nb thin films by pulsed laser deposition. Appl Surf Sci 255:9695–9698
117. Kambe M, Sato K, Kobayashi D, Kurokawa Y, Miyajimai S, Fukawa M, Taneda N, Yamada A, Konagai M (2006) TiO_2-coated transparent conductive oxide (SnO_2:F) films prepared by atmospheric pressure chemical vapor deposition with high durability against atomic hydrogen. Jpn J Appl Phys 45:L29–L293
118. Iida T, Takamidou Y, Watabe T, Yoshida N, Itoh T, Nonomura S (2006) High conductive TiO_2 films due to auto doping by hot wire CVD method for protecting materials of TCO against atomic hydrogen exposures 1-4244-0016-3. In: IEEE 4th world conference on photovoltaic energy conversion, conference record of the 2006, pp 1537–1539
119. Fanga Q, Zhanga J-Y, Wang ZM, Wub JX, O'Sullivanc BJ, Hurleyc PK, Leedhamd TL, Davies H, Audier MA, Jimenez C, Senateure J-P, Boyd Ian W (2003) Investigation of TiO_2-doped HfO_2 thin films deposited by photo-CVD. Thin Solid Films 428:263–268
120. Yazawa T, Machida F, Kubo N, Jin T (2009) Photocatalytic activity of transparent porous glass supported TiO_2. Ceram Int 35:3321–3325
121. Mills A, Lee S-K, Lepre A, Parkin IP, O'Neill SA (2002) Spectral and photocatalytic characteristics of TiO_2 CVD films on quartz. Photochem Photobiol Sci 1:865–868
122. Pazoki M, Taghavinia N, Abdi Y, Tajabadi F, Boschloo G, Hagfeldt A (2012) CVD-grown TiO_2 particles as light scattering structures in dye-sensitized solar cells. RSC Adv 2:12278–12285
123. Manolea AV, Dobromirb M, Gırtanc M, Mallet R, Rusua G, Lucaa D (2013) Optical properties of Nb-doped TiO_2 thin films prepared by sol–gel method. Ceram Int 39:4771–4776
124. Liu J, Zhao X, Duan L, Cao M, Sun H, Shao J, Chen S, Xie H, Chang X, Chen C (2011) Influence of annealing process on conductive properties of Nb-doped TiO_2 polycrystalline films prepared by sol–gel method. Appl Surf Sci 257:10156–10160
125. Malengreaux CM, Timmermans A, Pirard SL, Lambert SD, Pirard J-P, Poelman D, Heinrichs B (2012) Optimized deposition of TiO_2 thin films produced by a non-aqueous sol–gel method and quantification of their photocatalytic activity. Chem Eng J 195–196:347–358
126. Sharma SK, Vishwas M, Rao NK, Mohan S, Reddy SD, Gowda KVA (2009) Structural and optical investigations of TiO_2 films deposited on transparent substrates by sol–gel technique. J Alloys Compd 471:244–247
127. Wen T, Gao J, Shen J, Zhou Z (2001) Preparation and characterization of TiO_2 thin films by sol–gel process. J Mater Sci 36:5923–5926. doi:10.1023/A:1012989012840

128. Gusmano G, Montesperelli G, Nunziante P, Traversa E, Montenero A, Braghini M, Mattogno G, Bearzotti A (1993) Humidity-sensitive properties of titania films prepared using the sol–gel process. J Ceram Soc Jpn 101:1095–1100
129. Tai W-P, Oh J-H (2002) Fabrication and humidity properties of nanostructured TiO_2–SnO_2 thin films. Sens Actuators B 85:154–157
130. Avellaneda CO, Pawlick A (1998) Preparation of transparent CeO_2–TiO_2 coatings for electrochromic devices. Thin Solid Films 335:245–248
131. Oja I, Mere A, Krunks M, Solterbeck C-H, Es-Souni M (2004) Properties of TiO_2 films prepared by the spray pyrolysis method. Solid State Phenom 99–100:259–264
132. Negishi N, Takeuchi K, Ibusuki T (1998) Surface structure of the TiO_2 thin film photocatalyst. J Mater Sci 33:5789–5794. doi:10.1023/A:1004441829285
133. Bashir A, Wöbkenberg PH, Smith J, Ball JM, Adamopoulos G, Bradley DDC, Thomas D (2009) Anthopoulos high-performance zinc oxide transistors and circuits fabricated by spray pyrolysis in ambient atmosphere. Adv Mater 21:2226–2231
134. Abou-Helal MO, Seeber WT (2002) Preparation of TiO_2 thin films by spray pyrolysis to be used as a photocatalyst. Appl Surf Sci 195:53–62
135. Ayieko CO, Musembi RJ, Waita SM, Aduda BO, Jain PK (2012) Structural and optical characterization of nitrogen-doped TiO_2 thin films deposited by spray pyrolysis on fluorine doped tin oxide (FTO) coated glass slides. J Energy Eng 2(3):67–72
136. Comini E, Guidi V, Ferroni M, Sberveglieri G (2004) TiO_2:Mo, MoO_3:Ti, TiO + WO_3 and TiO: W layer for landfill produced gases sensing. Sens Actuators B100:41–46
137. Comini E, Sberveglieri G, Guidi V (2000) Ti–W–O sputtered thin film as n- or p-type gas sensors. Sens Actuators B 70:108–114
138. Galatsis K, Li YX, Wlodarski W, Comini E, Sberveglieri G, Cantalini C, Santucci S, Passacantando M (2002) Comparison of single and binary oxide MoO_3, TiO_2 and WO_3 sol–gel gas sensors. Sens Actuators B 83:276–280
139. Ferroni M, Guidi V, Martinelli G, Comini E, Sberveglieri G, Boscarino D, Della G (2000) Electron microscopy and Rutherford backscattering study of nucleation and growth in nanosized W–Ti–O thin films. J Appl Phys 88:1097
140. Ferroni M, Guidi V, Martinelli G, Nelli P, Sberveglieri G (1997) Gas sensing applications of W–Ti–O-based nanosized thin films prepared by r.f. reactive sputtering. Sens Actuators B 44:499–502
141. Gerlicha M, Kornely S, Fleischer M, Meixner H, Kassing R (2003) Selectivity enhancement of a WO_3/TiO_2 gas sensor by the use of a four-point electrode structure. Sens Actuators B 83:503–508
142. Yamada Y, Seno Y, Masuoka Y, Nakamura T, Yamashita K (2000) NO_2 sensing characteristic of Nb doped TiO_2 thin films and their electronic properties. Sens Actuators B 66:164–166
143. Zakrzewska K, Radecka M, Rekas M (1997) Effect of Nb, Cr, Sn additions on gas sensing properties of TiO_2 thin films. Thin Solid Films 310:161–166
144. Ruiz A, Dezanneau G, Arbiol J, Cornet A, Morante JR (2003) Study of the influence of Nb content and sintering temperature on TiO_2 sensing films. Thin Solid Films 436:90–94
145. Oyabu T (1982) Sensing characteristics of SnO_2 thin film gas sensors. J Appl Phys 53:2785
146. Das S, Kim SH, Park YK, Choi CM, Kim DY, Hahn YB (2010) Heterojunction bipolar assembly with $Cr_xTi_{1-x}O_2$ thin films and vertically aligned ZnO nanorods. Mater Chem Phys 124:704–708
147. Ruiz A, Cornet A, Sakai G, Shimanoe K, Morante JR, Yamazoe N (2002) Preparation of Cr-doped TiO_2 thin film of p-type conduction for gas sensor application. Chem Lett 9:892–893
148. Liau LCK, Lin C-C (2008) Semiconductor characterization of Cr^{3+}-doped titania electrodes with p–n homojunction devices. Thin Solid Films 516:1998–2002
149. Domaradzki J, Kaczmarek D (2008) Electrical and optical properties of TOS–S heterojunction devices. Thin Solid Films 516:1473–1475
150. Mowbray DJ, Martinez JI, García Lastra JM, Thygesen KS, Jacobsen KW (2009) Stability and electronic properties of TiO_2 nanostructures with and without B and N doping. J Phys Chem C 113:12301–12309
151. Zhang Z-F, Deng Z-B, Liang C-J, Zhang M-X, Xu D-H (2003) Organic light-emitting diodes with a nanostructured TiO_2 layer at the interface between ITO and NPB layers. Displays 24:231–234
152. Haque SA, Koops S, Tokmoldin N, Durrant JR, Huang J, Bradley DDC, Palomares E (2007) A multilayered polymer light-emitting diode using a nanocrystalline metal-oxide film as a charge-injection electrode. Adv Mater 19:683–687
153. Könenkamp R, Word RC, Godinez M (2006) Electroluminescence in nanoporous TiO_2 solid-state heterojunctions. Nanotechnology 17:1858
154. Hou L, Liu P, Li Y, Wu C (2009) Enhanced performance in organic light-emitting diodes by sputtering TiO_2 ultra-thin film as the hole buffer layer. Thin Solid Films 517:4926–4929
155. Aziz THT, Salleh MM, Yahaya M (2007) Reduction of turn-on voltage in polymer organic light-emitting diode using nanoparticles TiO_2 thin film as a hole injection layer. Solid State Sci Technol 15:75–83
156. Bally A, Korobeinikova EN, Schmid PE, Levy F, Bussy F (1998) Structural and electrical properties of Fe-doped TiO_2 thin films. J Phys D Appl Phys 31:1149–1154
157. Li Y, Wlodarski W, Galatsis K, Moslih S, Cole J, Russo S, Rockelmann N (2002) Gas sensing properties of p-type semiconducting Cr-doped TiO_2 thin films. Sens Actuators B 83:160–163
158. Ruiz A, Sakai G, Cornet A, Shimanoe K, Morante J, Yamazoe N (2003) Cr-doped TiO_2 gas sensor for exhaust NO_2 monitoring. Sens Actuators B 93:509–518
159. Salvador P (1984) Hole diffusion length in n-TiO_2 single crystals and sintered electrodes: photoelectrochemical determination and comparative analysis. J Appl Phys 55:2977
160. Li Z, Ding D, Ning C (2013) p-type hydrogen sensing with Al- and V-doped TiO_2 nanostructures. Nanoscale Res Lett 8:25
161. Sieradzka K, Mazur M, Wojcieszak D, Domaradzki J, Kaczmarek D, Prociow E (2012) p-type transparent Ti–V oxides semiconductor thin film as a prospective material for transparent electronics. Thin Solid Films 520:3472–3476
162. Sieradzka K, Domaradzki J, Prociow E, Mazur M, Lapinski M (2009) Properties of Nanocrystalline TiO_2: V thin films as a transparent semiconducting oxide. Acta Phys Pol A 116:S33–S35
163. Prociow EL, Sieradzka K, Domaradzki J, Kaczmarek D, Mazur M (2009) Thin films based on nanocrystalline TiO_2 for transparent electronics. Acta Phys Pol A 116:S72–S74
164. Carp O, Huisman CL, Reller A (2004) Photoinduced reactivity of titanium dioxide. Prog Solid Stat Chem 32:33–177
165. Cromer DT, Herrington K (1955) The structure of anatase and rutile. J Am Chem Soc 77:4708–4709
166. Baur VWH (1961) Atomabstande und binungswinkel im brookit, TiO_2. Acta Cryst 14:214–216
167. Mo S-D, Ching WY (1995) Electronic and optical properties of three phases of titanium dioxide: rutile, anatase, and brookite. Phys Rev B 51:13023
168. Avaraham S, Kaplan WD (2005) Reactive wetting of rutile by liquid aluminium. Mater Sci 40:1093–1100

169. Thompson TL, Yates JT Jr (2006) Surface science studies of the photoactivation of TiO_2-new photochemical processes. Chem Rev 196:4428–4453
170. Hanaor DAH, Sorrell CC (2011) Review of the anatase to rutile phase transformation. J Mater Sci 46:855–874. doi:10.1007/s10853-010-5113-0
171. Norotsky A, Jamieson JC, Kleppa OJ (1967) Enthalpy of transformation of a high pressure polymorph of titanium dioxide to the rutile modification. Science 158:338–339
172. Zhang Q, Gao L, Guo J (2000) Preparation of plasma sprayed titania/hydroxyapatite photocatalytic coatings with nanostructured powder. Appl Catal B 26:207–215
173. Sclafani A, Palmisano L, Schiavello M (1990) Influence of the preparation methods of TiO, on the photocatalytic degradation of phenol in aqueous dispersion. J Phys Chem 94:829–832
174. Muscat J, Swamy V, Harrison NM (2002) First-principles calculations of the phase stability of TiO_2. Phys Rev B 65:224112
175. Tanaka Keiichi, Capule Mario FV, Hisanaga Teruaki (1991) Effect of crystallinity of TiO_2 on is photocatalytic action. Appl Phys Lett 187:73–76
176. Selloni A (2008) Crystal growth: anatase shows its reactive side. Nat Mater 7:613–615
177. Yang HG, Sun CH, Qiao SZ, Zhou J, Smith SC, Cheng HM, Lu GQ (2008) Anatase TiO_2 single crystals with a large percentage of reactive facets. Nature 453:638
178. Wunderlich W, Oekermann T, Miao L, Nguyen TH, Tanemura S, Tanemura M (2004) Electronic properties of nanoporous TiO_2- and ZnO thin films—comparison of simulations and experiments. J Ceram Process Res 5:343
179. Paxton AT, Thien-Nga L (1998) Electronic structure of reduced titanium dioxide. Phys Rev B 57:1579
180. Bellingham JR, Phillips WA, Adkins CJ (1992) Intrinsic performance limits in transparent conducting oxides. J Mater Sci Lett 11:263–265
181. Bassi AL, Cattaneo D, Russo V, Bottani CE, Barborini E, Mazza T, Piseri P (2005) Raman spectroscopy characterization of titania nanoparticles produced by flame pyrolysis: the influence of size and stoichiometry. J Appl Phys 98:074305
182. Hardcastle FD (2011) Raman spectroscopy of titania (TiO_2) nanotubular water-splitting catalysts. J Ark Acad Sci 65:43–48
183. Šćepanović MJ, Grujić-Brojčin M, Dohčević-Mitrović ZD, Popović ZV (2009) Characterization of anatase TiO_2 nanopowder by variable-temperature Raman spectroscopy. Sci Sinter 41:67–73
184. Narayanan PS (1950) The Raman spectrum of beryllium silicate. Proc Indian Acad Sci A 32(4):279–283
185. Balachandran U, Eror NG (1982) Raman spectrum of titanium dioxide. J Solid State Chem 42:276–282
186. Ohsaka T (1980) Temperature dependence of the Raman spectrum in anatase TiO_2. J Phys Soc Jpn 48:1661–1668
187. Choi HC, Jung YM, Kim SB (2005) Size effects in the Raman spectra of TiO_2 nanoparticles. Vib Spectrosc 37:33–38
188. Gonzalez RJ (1996) Raman, infrared, X-ray, and EELS studies of nanophase titania. PhD thesis, Virginia Polytechnic Institute and State University
189. Tompsett GA, Bowmaker GA, Cooney RP, Metson JB, Rodgers KA, Seakins JM (1995) The Raman spectrum of brookite, TiO_2 (PbCa, $z = 8$). J Raman Spectrosc 26:57–62
190. Li JG, Ishigaki T, Sun X (2007) Anatase, brookite, and rutile nanocrystals via redox reactions under mild hydrothermal conditions: phase-selective synthesis and physicochemical properties. J Phys Chem C 111:4969–4976
191. Iliev MN, Hadjiev VG, Litvinchuk AP (2013) Raman and infrared spectra of brookite (TiO_2): experimental and theory. Vib Spectrosc 64:148–152
192. Hu W, Li L, Li G, Tang C, Sun L (2009) High-quality brookite TiO_2 flowers: synthesis, characterization, and dielectric performance. Cryst Growth Des 9:3676–3682
193. Triebold S, Luvizotto GL, Tolosana-Delgado R, Zack T, Eynatten HV (2011) Discrimination of TiO_2 polymorphs in sedimentary and metamorphic rocks. Contrib Mineral Petrol 161:581–596
194. Paola AD, Bellardita M, Palmisano L (2013) Brookite, the least known TiO_2 photocatalyst. Catalysts 3:36–73
195. Hu Y, Tsai H-L, Huang C-L (2003) Effect of brookite phase on the anatase-rutile transition in titania nanoparticles. J Eur Ceram Soc 23:691–696
196. Rezaee M, Khoie S, Liu H (2011) The role of brookite in mechanical activation of anatase-to-rutile transformation of nanocrystalline TiO_2: an XRD and Raman spectroscopy investigation. Cryst Eng Commun 13:5055–5061
197. Kelly S, Pollak FH, Tomkiewicz M (1997) Raman spectroscopy as a morphological probe for TiO_2 aerogels. J Phys Chem B 101:2730–2734
198. Bersani D, Lottici PP (1998) Phonon confinement effects in the Raman scattering by TiO_2 nanocrystals. Appl Phys Lett 72:73–75
199. Zhang WF, He YL, Zhang MS, Yin Z, Chen Q (2000) Raman scattering study on anatase TiO_2 nanocrystals. J Phys D Appl Phys 33:912–916
200. Choi HC, Mee JY, Bin KS (2004) Characterization of Raman spectra of size-selected TiO_2 nanoparticles by two-dimensional correlation spectroscopy. Bull Korean Chem Soc 25:426–428
201. Turković A, Ivanda M, Popović S, Tonejc A, Gotić M, Dubček P, Musić S (1997) Comparative Raman, XRD, HRTEM and SAXS studies of grain sizes in nanophase TiO_2. J Mol Struct 410–411:271–273
202. Gotić M, Ivanda M, Popović S, Musić S, Sekulić A, Turković A, Furić K (1997) Raman investigation of nanosized TiO_2. J Raman Spectrosc 28:555–558
203. Musić S, Gotić M, Ivanda M, Popović S, Turković A, Trojko R, Sekulić A, Furić K (1997) Chemical and microstructural properties of TiO_2 synthesized by sol–gel procedure. Mater Sci Eng B 47:33–40
204. Taga N, Odaka H, Shigesato Y, Yasui M Kamei, Haynes TE (1996) Electrical properties of heteroepitaxial grown tin-doped indium oxide films. J Appl Phys 80:978–984
205. Bender M, Trube J, Stollenwerk J (1999) Deposition of transparent and conducting indium-tin-oxide films by the r.f.-superimposed DC sputtering technology. Thin Solid Films 354:100–105
206. Minami T (2000) New n-type transparent conducting oxides MRS Bull. 25:38–44
207. Kikuchi N, Kusano E, Nanto H, Kinbara A, Hosono H (2000) Phonon scattering in electron transport phenomena of ITO films. Vacuum 59:492–499
208. Ellmer K (2001) Resistivity of polycrystalline zinc oxide films: current status and physical limit. J Phys D Appl Phys 34:3097–3108
209. Odaka H, Shigesato Y, Murakani T, Iwata S (2001) Electronic structure analyses of Sn-doped In_2O_3. Jpn J Appl Phys 40:3231–3235
210. Thangaraju B (2002) Structural and electrical studies on highly conducting spray deposited fluorine and antimony doped SnO_2 thin films from $SnCl_2$ precursor. Thin Solid Films 402:71–78
211. Lee H-C, Park OO (2004) Behaviours of carrier concentrations and mobilities in indium-tin oxide thin films by DC magnetron sputtering at various flow rates. Vacuum 77:69–77
212. Lee H-C, Park OO (2004) Electron scattering mechanisms in indium-tin-oxide thin films: grain boundary and ionized impurity. Vacuum 75:275–282

213. Shigesato Y, Paine DC (1993) Study of the effect of Sn doping on the electronic transport properties of thin indium oxide. Appl Phys Lett 62:1268–1270
214. Bunstein E (1954) Anomalous optical absorption limit in InSb. Phys Rev 93:632–633
215. Moss TS (1954) The interpretation of the properties of indium antimonide. Proc Phys Soc Lond B 67:775–782
216. Granqvist CG (1991) Oxide-based electrochromic materials and devices prepared by magnetron sputtering (chapter 5), vol 106. Pergamon, Oxford
217. Shirakata S, Sakemi T, Awai K, Yamamoto T (2006) Electrical and optical properties of large area Ga-doped ZnO thin films prepared by reactive plasma deposition. Superlattices Microstruct 39:218–228
218. Ilican S, Caglar Y, Caglar M, Yakuphanoglu F (2008) Structural, optical and electrical properties of F-doped ZnO nanorod semiconductor thin films deposited by sol–gel process. Appl Surf Sci 255:2353–2359
219. Wu X, Dhere RG, Zhou J, Duda A, Perkins C, Yan Y, Moutinho HR (2003) 3rd World conference on photovoltaic energy conversion, Osako, Japan, May 11–18
220. Grant FA (1959) Properties of rutile (titanium oxide). Rev Mod Phys 31:646
221. Furubayashi Y, Hitosugi T, Hasegawa T (2006) Response to "Comment on 'A transparent metal: Nb-doped anatase TiO_2 [Appl. Phys. Lett. 86, 252101 (2005)]". Appl Phys Lett 88:226103
222. Zhang SX, Kundaliya DC, Yu W, Dhar S, Young SY, Salamanca-Riba LG, Ogale SB, Vispute RD, Venkatesan T (2007) Nb doped TiO_2: intrinsic transparent metallic anatase versus highly resistive rutile phase. J Appl Phys 102:013701
223. Cronemeyer DC (1952) Electrical and optical properties of rutile single crystals. Phys Rev 87:876
224. Berger H, Tang H, Lévy F (1993) Growth and Raman spectroscopic characterization of TiO_2 anatase single crystals. J Cryst Growth 130:108–112
225. Forro L, Chauvet O, Emin D, Zuppiroli Z, Berger H, Lévy F (1994) High mobility n-type charge-carriers in large single-crystals of anatase (TiO_2). J Appl Phys 75:633–635
226. Mulmi DD, Sekiya T, Kamiya N, Kurita S, Murakami Y, Kodaira T (2004) Optical and electrical properties of Nb-doped anatase single crystals. J Phys Chem Solids 65:1181–1185
227. Chambers SA (2000) Epitaxial growth and properties of thin film oxides. Surf Sci Rep 39:105–180
228. Maghanga CM, Niklasson GA, Granqvist CG (2009) Optical properties of sputter deposited transparent and conducting TiO2: Nb films. Thin Solid Films 518:1254–1258
229. Welte A, Waldauf C, Brabec C, Wellmann P (2008) Application of optical for the investigation of electronic and structural properties of sol–gel processed TiO_2 films. Thin Solid Films 516:7256–7259
230. Monllor-Satoca D, Gomez R, González-Hidalgo M, Salvador P (2007) The "diret-indirect" model: an alternative kinetic approach in heterogeneous photocatalysis based on the degree of interaction of dissolved pollutant species with the semiconductor surface. Catal Today 129:247–255
231. Valencia S, Marin JM, Restrepo G (2010) Study of the band gap of synthesized titanium dioxide nanoparticles using the sol–gel method and hydrothermal treatment. TOMSJ 4:9–14
232. Kalathil S, Khan MM, Banerjee AN, Lee J, Cho MH (2012) A simple biogenic route to rapid synthesis of Au@TiO_2 nanocomposites by electrochemically active biofilms. J Nanopart Res 14:1051
233. Reddy K, Manorama S, Redd A (2002) Bandgap studies on anatase titanium dioxide nanoparticles. Mater Chem Phys 78:239–245
234. Zallen R, Moret MP (2006) The optical absorption edge of brookite TiO_2. Solid State Commun 137:154–157
235. Efros AL, Efros AL (1982) Interband absorption of light in a semiconductor sphere. Sov Phys Semicond 16:772–775
236. Brus LE (1984) Electron-electron and electron-hole interactions in small semiconductor crystallites: the size dependence of the lowest excited electronic state. J Chem Phys 80:4403–4409
237. Kayanuma Y (1988) Quantum size effects of interacting electrons and holes in semiconductor microcrystals with spherical shape. Phys Rev B Condens Matter 38:9797–9805
238. Schoenhalz AL, Dalpian GM (2013) Cobalt-doped ZnO nanocrystals: quantum confinement and surface effects from ab initio methods. Phys Chem Chem Phys 15:15863–15868
239. Haranath D, Sahai S, Joshi AG, Gupta BK, Shanker V (2009) Investigation of confinement effects in ZnO quantum dots. Nanotechnology 20:425701
240. Deng H-X, Li S-S, Li J (2010) Quantum confinement effects and electronic properties of SnO_2 quantum wires and dots. J Phys Chem C 114:4841–4845
241. Sahana MB, Sudakar C, Dixit A, Thakur JS, Naik R, Naik VM (2012) Quantum confinement effects and band gap engineering of SnO_2 nanocrystals in a MgO matrix. Acta Mater 60:1072–1078
242. Banerjee AN, Joo SW, Min B-K (2012) Quantum size effect in the photoluminescence properties of p-type semiconducting transparent $CuAlO_2$ nanoparticles. J Appl Phys 112:114329
243. Banerjee AN, Chattopadhyay KK (2005) Size-dependent optical properties of sputter-deposited nanocrystalline p-type transparent $CuAlO_2$ thin films. J Appl Phys 97:084308
244. Hmiel A, Xue Y (2012) Quantum confinement and surface relaxation effects in rutile TiO_2 nanowires. Phys Rev B 85:235461
245. Peng H, Li J (2008) Quantum confinement and electronic properties of rutile TiO_2 nanowires. J Phys Chem C 112: 20241–20245
246. Lin H, Huang CP, Li W, Ni C, Shah SI, Tseng YH (2006) Size dependency of nanocrystalline TiO_2 on its optical property and photocatalytic reactivity exemplified by 2-chlorophenol. Appl Catal B Environ 68:1–11
247. Drbohlavova J, Vorozhtsova M, Hrdy R, Kizek R, Salyk O, Hubalek J (2012) Self-ordered TiO_2 quantum dot array prepared via anodic oxidation. Nanoscale Res Lett 7:123
248. Weng Z, Guo H, Liu X, Wu S, Yeung KWK, Chu PK (2013) Nanostructured TiO_2 for energy conversion and storage. RSC Adv 3:24758–24775
249. Church CP, Muthuswamy E, Zhai G, Kauzlarich SM, Carter SA (2013) Quantum dot Ge/TiO_2 heterojunction photoconductor fabrication and performance. Appl Phys Lett 103:223506
250. Khan AF, Mehmood M, Aslam M, Shah SI (2010) Nanostructured multilayer TiO_2–Ge films with quantum confinement effects for photovoltaic applications. J Colloid Interface Sci 343:271–280
251. Hao YZ, Chun TC, Shan FS (2001) Optical absorption of sol–gel derived ZnO/TiO_2 nanocomposite films. Chin Phys Lett 18:1520–1522
252. Banerjee AN, Ghosh CK, Chattopadhyay KK (2005) Effect of excess oxygen on the electrical properties of transparent p-type conducting $CuAlO_{2+x}$ thin films. Sol Energy Mater Sol Cells 89:75–83
253. Kofstad P (1972) Nonstoichiometry, diffusion and electrical conductivity of binary metal oxides. Wiley, New York
254. Lin H, Kozuka H, Yoko T (2000) Electrical properties of transparent doped oxide films. J Sol Gel Sci Technol 19:529–532
255. Nowotny J, Sorrell CC, Sheppard LR, Bak T (2005) Solar-hydrogen: environmental safe fuel for the future. Int J Hydrogen Energy 30:521–544

256. Nowotny J, Sorrell CC, Bak T, Sheppard LR (2005) Materials for energy conversion devices. Woodhead Publishing, Cambridge, pp 84–116
257. Nowotny MK, Bak T, Nowotny J, Sorrell CC (2005) Titanium vacancies in nonstoichiometric TiO_2 single crystal. Phys Status Solid B 242:R88–R90
258. Bak T, Nowotny J, Rekas M, Sorrell CC (2003) Defect chemistry and semiconducting properties of titanium dioxide: I. Intrinsic electronic equilibrium. J Phys Chem Solids 64: 1043–1056
259. Bak T, Nowotny J, Rekas M, Sorrell CC (2003) Defect chemistry and semiconducting properties of titanium dioxide: II. Defect diagrams. J Phys Chem Solids 64:1057–1067
260. Sheppard LR, Bak T, Nowotny J (2006) Electrical properties of niobium doped titanium dioxide I. Defect disorder. J Phys Chem B 110:22447–22454
261. Bak T, Nowotny J, Nowotny MK, Sheppard LR (2007) Defect chemistry of titanium dioxide effect of interfaces. J Aust Ceram Soc 43:49–55
262. Chen PC, Shen GZ, Chen H (2009) High-performance single-crystalline arsenic-doped indium oxide nanowires for transparent thin-film transistors and active matrix organic light-emitting diode displays. ACS Nano 3:3383–3390
263. Chen P, Shen GZ, Sukcharoenchoke S, Zhou CW (2009) Flexible and transparent supercapacitor based on In_2O_3 nanowire/carbon nanotube heterogeneous films. Appl Phys Lett 94:043113
264. Shen GZ, Xu J, Wang XF, Huang HT, Chen D (2011) Growth of directly transferable In_2O_3 nanowire mats for transparent thin-film transistor applications. Adv Mater 23:771–775
265. Shen GZ, Liang B, Wang XF, Huang HT, Chen D, Wang ZL (2011) Ultrathin In_2O_3 nanowires with diameters below 4 nm: synthesis, reversible wettability switching behaviour and transparent thin-film transistor applications. ACS Nano 5:6148–6155
266. Kim JY, Noh JH, Zhu K, Halverson AF, Neale NR, Park S, Hong KS, Frank AJ (2011) General strategy for fabricating transparent TiO_2 nanotube arrays for dye-sensitized photoelectrodes: illumination geometry and transport properties. ACS Nano 5:2647–2656
267. Nakata K, Sakai M, Ochiai T, Murakami T, Takagi K, Fujishima A (2011) Antireflection and self-cleaning properties of a moth-eye-like surface coated with TiO_2 particles. Langmuir 27:3275–3278
268. Wang R, Hashimoto K, Fujishima A (1997) Light-induced amphiphilic surfaces. Nature 388:431–432
269. Yuwono AH, Xue J, Wang J (2003) Transparent nano hybrids of nanocrystalline TiO_2 in PMMA with unique nonlinear optical behaviour. J Mater Chem 13:1475–1479
270. Nakato Y, Kai K, Kawabe K (1995) Improvement of characteristics of new-type solar cells, having a transparent conductor/thin SiO_2 layer with ultrafine metal particles as conductive channels/n-Si junction. Sol Energy Mater Sol Cells 37:323–335
271. Minami T, Takata S, Kakumu T (1996) New multicomponent transparent conducting oxide films for transparent electrodes of flat panel displays. J Vac Sci Technol A 14:1704–1708
272. Yanagawa K, Ohki Y, Omata T, Hosono H, Ueda N, Kawazoe H (1994) Preparation of $Cd_{1-x}Y_xSb_2O_6$ thin film on glass substrate by radio frequency sputtering. Appl Phys Lett 65:406–408
273. Dong Y, Chao J, Xie Z, Xu X, Wang Z, Chen D (2012) Highly ordered TiO_2 macropore arrays as transparent photocatalysts. J Nanomater. doi:10.1155/2012/762510
274. Nomura K, Ohta H, Ueda K, Kamiya T, Hirano M, Hosono H (2003) Thin-film transistor fabricated in single-crystalline transparent oxide semiconductor. Science 300:1269–1272
275. Ueno K, Inoue IH, Akoh H, Kawasaki M, Tokura Y, Takagi H (2003) Field-effect transistor on $SrTiO_3$ with sputtered Al_2O_3 gate insulator. Appl Phys Lett 83:1755
276. Shibuya K, Ohnishi T, Kawasaki M, Koinuma H, Lippmaa M (2004) Single crystal SrTiO3 field-effect transistors with an atomically flat amorphous $CaHfO_3$ gate insulator. Appl Phys Lett 85:425
277. Ueno K, Inoue IH, Yamada T, Akoh H, Tokura Y, Takagi H (2004) Field-effect transistor based on $KTaO_3$ perovskite. Appl Phys Lett 84:3726
278. Shen G, Chen PC, Ryu K, Zhou C (2009) Devices and chemical sensing applications of metal oxide nanowires. J Mater Chem 19:828–839
279. Odobel F, Pleux LL, Pellegrin Y, Blart E (2010) New photovoltaic devices based on the sensitization of p-type semiconductors: challenges and opportunities. Acc Chem Res 43:1063–1071
280. Ruiz A, Cornet A, Sakai G, Shimanoe K, Morante JR, Yamazoe N (2002) Preparation of Cr-doped TiO_2 thin film of P-type conduction for gas sensor application. Chem Lett 31:892–893
281. Sobajima Y, Kato S, Matsuura T, Toyama T, Okamoto H (2007) Study of the light-trapping effects of textured ZnO:Al/glass structure TCO for improving photocurrent of a-Si: H solar cells. J Mater Sci Mater Electron 18:159–162
282. Das S, Kim JH, Park YK, Hahna YB (2011) Solution processed Ni-doped TiO_2 p-type channel in field effect transistor assemble with <10 nm thin $Ba_{0.5}Sr_{0.5}TiO_3$ dielectric layer. Appl Phys Lett 98:202102
283. Das S, Liu D, Park JB, Hahn YB (2013) Metal-ion doped p-type TiO_2 thin films and their applications for heterojunction devices. J. Alloys Compd 553:188–193
284. Sarkar D, Ghosh CK, Mukherjee S, Chattopadhyay KK (2013) Three dimensional Ag_2O/TiO_2 type-II (p–n) nanoheterojunctions for superior photocatalytic activity. ACS Appl Mater Interfaces 5:331–337
285. O'Regan Grätzel M (1991) A low-cost high-efficiency solar cell based on dye-sensitized colloidal TiO_2 films. Nature 353:737–740
286. Liu H, Avrutin V, Izyumskaya N, Özgür Ü, Morkoç H (2010) Transparent conducting oxides for electrode applications in light emitting and absorbing devices. Superlattices Microstruct 48:458–484
287. Nazeeruddin MK, Kay A, Rodicio I, Humphry-Baker R, Muller E, Liska P, Vlachopoulos N, Gratzel M (1993) Conversion of light to electricity by *cis*-$X_2(dcbpy)_2Ru(II)$ CT sensitizers on nanocrystalline TiO_2 electrodes. J Am Chem Soc 115: 6382–6390
288. Tamura K, Nakahara K, Sakai M, Nakagawa D, Ito N, Sonobe M, Takasu H, Tampo H, Fons P, Matsubara K, Iwata K, Yamada A, Niki S (2004) InGaN-based light-emitting diodes fabricated with transparent Ga-doped ZnO as ohmic p-contact. Phys Status Solid 201:2704–2707
289. Smestad G, Bignozzi C, Argazzi R (1994) Testing of dye sensitized TiO_2 solar cells I: experimental photocurrent output and conversion efficiencies. Sol Energy Mater Sol Cell 32:259–272
290. Rani S, Mehra RM (2009) ZnO solid-state dye sensitized solar cells using composite electrolyte of poly(3-hexylthiophene-2,5-diyl) and carbon nanotubes. J Renew Sustain Energy 1:033109–033112
291. Pradhan B, Batabyal SK, Pal AJ (2007) Vertically aligned ZnO nanowire arrays in Rose Bengal-based dye-sensitizes solar cells. Sol Energy Mater Sol Cells 91:769–773
292. Grätzel M (2003) Dye-sensitized solar cells. J Photochem Photobiol C 4:145–153
293. Mor GK, Varghese OK, Paulose M, Shankar K, Grimes CA (2006) A review on highly ordered, vertically oriented TiO_2

nanotube arrays: fabrication, material properties, and solar energy applications. Sol Energy Mater Sol Cells 90:2011–2075
294. Karthikeyan CS, Thelakkat M (2008) Key aspects of individual layers in solid-state dye-sensitized solar cells and novel concepts to improve their performance. Inorg Chim Acta 361:635–655
295. Suzuki I, Ohtomo A, Tsukazaki A, Sato F, Nishii J, Ohno H, Kawasaki M (2004) Hall and field-effect mobilities of electrons accumulated at a lattice-matched ZnO/$ScAlMgO_4$ heterointerface. Adv Mater 16:1887–1890
296. Paulose M, Shankar K, Yoriya S, Prakasam HE, Varghese OK, Mor GK, Latempa TA, Fitzgerald A, Grimes CA (2006) Anodic growth of highly ordered TiO_2 nanotube arrays to 134 μm in length. J Phys Chem B 110:16179–16184
297. Lee K, Kirchgeorg R, Schmuki P (2014) Role of transparent electrodes for high efficiency TiO_2 nanotube based dye-sensitized solar cells. J Phys Chem C 118:16562–16566
298. Suzuki I, Ohtomo A, Tsukazaki A, Sato F, Nishii J, Ohno H, Kawasaki M (2004) Hall and field-effect mobilities of electrons accumulated at a lattice-matched ZnO/$ScAlMgO_4$ heterointerfaces. Adv M ater 16:1887–1890
299. Chang IF (1976) Electrochromic and electrochemichromic materials and phenomena. In: Proceedings of the 4th Brown Boveri symposium on nonemissive electrooptic displays, pp 155–196
300. Oi T (1986) Electrochromic materials. Annu Rev Mater Sci 16:185–201
301. Hotchandani S, Bedja I, Fessenden R, Kamat P (1994) Electrochromic and photoelectrochromic behaviour of thin WO_3 films prepared from quantum size colloidal particles. Langmuir 10:17–22
302. Deepa M, Sharma N, Varshney P, Varma SP, Agnihotry SA (2000) FTIR investigations of solid precursor materials for sol–gel deposition of WO_3 based electrochromic films. J Mater Sci 35:5313–5318. doi:10.1023/A:1004838627252
303. Agnihotry SA, Sharma N, Deepa M (2002) Ion exchange precursor materials for deposition of WO_3 electrochromic films. J Sol Gel Sci Technol 24:265–270
304. Granqvist CG (1992) Electrochromism and smart window design. Solid State Ion 53–56:479–489
305. Reichman B, Bard AJ (1980) Electrochromism at niobium pentoxide electrodes in aqueous and acetonitrile solutions. J Electrochem Soc 127:241–242
306. Schmitt M, Heusing S, Aegerter MA, Pawlicka A, Avellaneda C (1998) Electrochromic properties of Nb_2O_5 sol–gel coatings. Sol Energy Mater Sol Cells 54:9–17
307. Avellaneda CO, Pawlicka A, Aegerter MA (1998) Two methods of obtaining sol–gel Nb_2O_5 thin films for electrochromic devices. J Mater Sci 33:2181–2185. doi:10.1023/A:1004339723987
308. Pawlicka A, Atik M, Aegerter MA (1997) Synthesis of multicolor Nb_2O_5 coatings for electrochromic devices. Thin Solid Films 301:236–241
309. Pawlicka A, Atik M, Aegerter MA (1995) Synthesis of Nb205 thin films for electrochromic devices. J Mater Sci Lett 14:1568–1570
310. Faria RC, Bulhoes LOdS (1994) A novel synthetic route to NbJOS thin films for electrochromic devices. J Electrochem Soc 141:L29–L30
311. Bell JM, Barczynska J, Evans LA, MacDonald KA, Wang J, Green DC, Smith GB (1994) Proceedings of SPIE: the international society for optical engineering, vol 2255, pp 324–331
312. Kitao M, Oshima Y, Urabe K (1997) Preparation and electrochromism of RF-sputtered TiO_2 films. Jpn J Appl Phys 36:4423–4426
313. Yoshimura K, Miki T, Tanemura S (1997) TiO_2 electrochromic thin films by reactive direct current magnetron sputtering. J Vac Sci Technol A 15:2673–2676
314. Campus F, Bonhote P, Gratzel M, Heinen S, Walder L (1999) Electrochromic devices based on surface-modified nanocrystalline TiO_2 thin-film electrodes. Sol Energy Mater Sol Cells 56:281–297
315. Cinnsealach R, Boschloo G, Rao SN, Fitzmaurice D (1999) Colored electrochromic windows based on nanostructured TiO_2 films modified by adsorbed redox chromophores. Sol Energy Mater Sol Cells 57:107–125
316. Wang Z, Hu X (1999) Fabrication and electrochromic properties of spin-coated TiO_2 thin films from peroxo-polytitanic acid. Thin Solid Films 352:62–65
317. Huang SY, Kavan L, Exnar I, Gratzel M (1995) Rocking chair lithium battery based on nanocrystalline TiO_2 (anatase). J Electrochem Soc 142:L142–L144
318. Cronemeyer DC (1959) Infrared absorption of reduced rutile single crystals. Phys Rev 113:1222–1226
319. Hagfeldt A, Vlachopoulos N, Graetzel M (1994) Fast electrochromic switching with nanocrystalline oxide semiconductor films. J Electrochem Soc 141:L82–L84
320. Lindstrom H, Sodergren S, Solbrand A, Rensmo H, Hjelm J, Hagfeldt A, Lindquist S-E (1997) Li+ ion insertion in TiO_2 (anatase). 2. Voltammetry on nanoporous films. J Phys Chem B 101:7717–7722
321. Lindstrom H, Sodergren S, Solbrand A, Rensmo H, Hjelm J, Hagfeldt A, Lindquist S-E (1997) Li+ ion insertion in TiO_2 (anatase). 1. Chronoameromety on CVD films and nanoporous films. J Phys Chem B 101:7710–7716
322. Ghicov A, Tsuchiya H, Hahn R, Macak JM, Munoz AG, Schmuki P (2006) TiO_2 nanotubes: H^+ insertion and strong electrochromic effects. Electrochem Commun 8:528–532
323. Hahn R, Ghicov A, Tsuchiya H, Macak JM, Munoz AG, Schmuki P (2007) Lithium–ion insertion in anodic TiO_2 nanotubes resulting in high electrochromic contrast. Phys Status Solid A 204:1281–1285
324. Ghicov A, Schmuki P (2009) Self-ordering electrochemistry: a review on growth and functionality of TiO_2 nanotubes and other self-aligned MO_x structures. Chem Commun 20:2791–2808
325. Varghese OK, Gong D, Paulose M, Ong KG, Dickey EC, Grimes CA (2003) Extreme changes in the electrical resistance of titania nanotubes with hydrogen exposure. Adv Mater 15:624–627
326. Khan SUM, Al-Shahry M, Ingler WB (2002) Efficient photochemical water splitting by a chemically modified n-TiO_2. Science 297:2243–2245
327. Mor GK, Shankar K, Varghese OK, Grimes CA (2004) Photoelectrochemical properties of titania nanotubes. J Mater Res 19:2989–2996
328. Sukamto JPH, Mcmillan CS, Smyrl W (1993) photoelectrochemical investigations of thin metal-oxide films-TiO_2, Al_2O_3, and HfO_2 on the parent metals. Electrochim Acta 38:15–27
329. Sukamto JPH, Smyrl WH, Mcmillan CS, Kozlowski MR (1992) Photoelectrochemical measurements of thin oxide films: multiple internal reflection effects. J Electrochem Soc 139:1033–1043
330. Hoffman P (2001) Tomorrow's energy: hydrogen, fuel cells, and the prospects for a cleaner planet. Cambridge University, Cambridge
331. Chtristofides C, Mandelis A (1990) Solid-state sensors for trace hydrogen gas detection. J Appl Phys 68:R1–R30
332. Ruths PF, Askok S, Fonash SJ, Ruths JM (1981) A study of Pd/Si MIS Schottky barrier diode hydrogen detector. IEEE Trans Electron Dev 28:1003–1009
333. Schalwig J, Muller G, Karrer U, Eickhoff M, Ambacher O, Stutzmann M, Gorgens L, Dollinger G (2002) Hydrogen response mechanism of Pt–GaN Schottky diodes. Appl Phys Lett 80:1222–1224

334. Roy S, Jacob C, Lang C, Basu S (2003) Studies on Ru/3C-SiC Schottky junctions for high temperature hydrogen sensors. J Electrochem Soc 150:H135–H139
335. Cheng S-Y (2003) A hydrogen sensitive Pd/GaAs Schottky diode sensor. Mater Chem Phys 78:525–528
336. Butler MA (1991) Optic sensor for hydrogen concentrations near the explosive limit. J Electrochem Soc 138:L46–L47
337. Sekimoto S, Nakagawa H, Okazaki S, Fukuda K, Asakura S, Shigemori T, Takahashi S (2000) A fiber-optic evanescent-wave hydrogen gas sensor using palladium-supported tungsten oxide. Sens Actuators B 66:142–145
338. Sutapun B, Tabib-Azar M, Kazemi A (1999) Pd-coated elastooptic fiber optic Bragg grating sensors for multiplexed hydrogen sensing. Sens Actuators B 60:27–34
339. Matsumiya M, Shin W, Izu N, Murayama N (2003) Nanostructured thin film Pt catalyst for thermoelectric hydrogen gas sensor. Sens Actuators B 93:309–315
340. Katti VR, Debnath AK, Gadkari SC, Gupta SK, Sahni VC (2002) Passivated thick film catalytic type H_2 operating at low temperature. Sens Actuators B 84:219–225
341. Luo RX, Chen LH, Chen AF, Liu CC (1991) A novel catalytic sensor for monitoring the concentration of mixed combustible gases. Sci China Ser A 34:1500–1507
342. Maffei N, Kuriakose AK (1999) A hydrogen sensor based on a hydrogen ion conducting solid electrolyte. Sens Actuators B 56:243–246
343. Katahira K, Matsumoto H, Iwahara H, Koide K, Iwamoto T (2001) A solid electrolyte hydrogen sensor with an electrochemically supplied hydrogen standard. Sens Actuators B 73:130–134
344. Lu G, Miura N, Yamazoe N (1996) High temperature hydrogen sensor based on stabilized zirconia and a metal oxide electrode. Sens Actuators B 130:35–36
345. Miura N, Harada T, Shimizu Y, Yamazoe N (1990) Cordless solid-state hydrogen sensor using proton-conductor thick film. Sens Actuators B 1:125–129
346. Lundstrom I, Shivaraman S, Svensson CS, Lundkvist L (1975) A hydrogen sensitive MOS field effect transistor. Appl Phys Lett 26:55–57
347. Miura N, Harada T, Yoshida N, Shimizu Y, Yamazoe N (1995) Sensing characteristics of ISFET-based hydrogen sensor using proton-conductive thick film. Sens Actuators B 25:499–503
348. Fomenko S, Gumenjuk S, Podlepetsky B, Chuvashov V, Safronkin G (1992) The influence of technological factors on the hydrogen sensitivity of mosfer sensors. Sens Actuators B 10:7–10
349. Hyodo T, Nishida N, Shimizu Y, Egashir M (2002) Preparation and gas-sensing properties of thermally stable mesoporous SnO_2. Sens Actuators B 83:209–215
350. Chaudhary VA, Mulla IS, Vijayamohanan K (1999) Selective hydrogen sensing properties of surface functionalized tin oxide. Sens Actuators B 55:154–160
351. Banerjee AN, Chattopadhyay KK (2008) Nanostructured p-type semiconducting transparent oxides: promising materials for nano-active devices and the emerging field of transparent nanoelectronics. Recent Pat Nanotechnol 2:41–68
352. Banerjee AN, Chattopadhyay KK (2009) P-type transparent semiconducting delafossite $CuAlO_{2+x}$ thin film. Nova Science Publisher, New York
353. Zamharir SG, Ranjbar M, Salamati H (2014) Excimer laser treatment of TiO2/WO3 thin films for self-cleaning gasochromic applications: preparation and characterization. Sol Energy Mater Sol Cells 130:27–35
354. Domaradzki J, Mazur M, Wojcieszak D, Kaczmarek D, Jedrzejak T (2015) Investigation of optical response of gasochromic thin film structures through modeling of their transmission spectra under presence of organic vapor. Acta Phys Pol A 127:1702–1705
355. Domaradzki J, Prociow E, Kaczmarek D, Wojcieszak D, Gatner D (2009) Gasochromic effect in nanocrystalline TiO_2 thin films doped with Ta and Pd. Acta Phys Pol A 116:S126–S128